Physik-Department
Lehrstuhl für Experimentalphysik E21

High energy resolution and first time-dependent positron annihilation induced Auger electron spectroscopy

Dissertation

Jakob Mayer

Technische Universität München

Fakultät für Physik der Technischen Universität München
Lehrstuhl für Experimentalphysik E21

High energy resolution and first time-dependent positron annihilation induced Auger electron spectroscopy

Dipl.-Phys. Univ. Jakob Mayer

Vollständiger Abdruck der von der Fakultät für Physik der Technischen Universität München zur Erlangung des akademischen Grades eines

Doktors der Naturwissenschaften (Dr. rer. nat.)

genehmigten Dissertation.

Vorsitzender:		Univ.-Prof. Dr. W. Zwerger
Prüfer der Dissertation:	1.	Univ.-Prof. Dr. K. Schreckenbach
	2.	apl. Prof. Dr. P.A. Feulner

Die Dissertation wurde am 04.03.2010 bei der Technischen Universität München eingereicht und durch die Fakultät für Physik am 30.04.2010 angenommen.

Abstract

The extensive characterization of surfaces and surface processes is of paramount interest in surface chemistry and surface physics. One typical elemental sensitive analysis method in this context is **E**lectron induced **A**uger **E**lectron **S**pectroscopy, EAES. Though it is widely accepted as a surface sensitive method, it averages over several atomic layers. In contrast to EAES, **P**ositron annihilation induced **A**uger **E**lectron **S**pectroscopy, PAES, examines almost exclusively the topmost atomic layer of a sample.

Although PAES has a higher surface selectivity and elemental selectivity compared to EAES, it has not been widely used in surface science yet. This is attributed mainly to the long measurement times needed in the past for a single PAES spectrum. For this reason, it was the aim of this thesis to improve the existing PAES spectrometer at the highly intense positron source NEPOMUC (**NE**utron induced **PO**sitron source **MU**ni**C**h) in several ways:
Firstly, the measurement time for a single PAES spectrum should be reduced from typically 12 h to roughly 1 h or even less. Secondly, the energy resolution, whicht amounted to $\Delta E/E \approx 10\%$, should be increased by at least one order of magnitude in order to make high resolution PAES-measurements of Auger transitions possible and thus deliver more information about the nature of the Auger process.

In order to achieve these objectives, the PAES spectrometer was equipped with a new electron energy analyzer. For its ideal operation all other components of the Auger analysis chamber had to be adapted. Particularly the sample manipulation and the positron beam guidance had to be renewed. Simulations with SIMION® ensured the optimal positron lens parameters.

After the adjustment of the new analyzer and its components, first measurements illustrated the improved performance of the PAES setup:
Firstly, the measurement time for short overview measurements was reduced from 3 h to an unprecedented low value of 420 s. Thus, for the first time measurement times are reached that are comparable with conventional methods. The measurement time for more detailed Auger spectra was shortened from 12 h to 80 min. This is much less than at other PAES spectrometers, where the measurement time amounts up to several days. Secondly, even with the reduced measurement time, the signal to noise ratio was also enhanced by one order of magnitude. Finally, the energy resolution was improved to $\Delta E/E < 1\%$.

The improved spectrometer at the high intensity 20 eV-beam of NEPOMUC enabled several completely novel measurements: The exceptional surface sensitivity and elemental selectivity of PAES was demonstrated in measurements of Pd and Fe, both coated with Cu layers of varying thickness. PAES showed that with 0.96 monolayer of Cu on Fe, more than 55% of the detected Auger electrons stem from Cu. With EAES in contrast, the same layer thickness produced a Cu Auger fraction of less than 6%. In the case of the Cu coated Pd sample 0.96 monolayer of Cu resulted in a Cu Auger fraction of more than 30% with PAES and less than 5% with EAES. The big difference between the two substrates, when measured with PAES, originates from the elemental selectivity due to the different positron affinities of Cu, Fe and Pd.
Secondly, the short recording time enabled for the first time the measurement of dynamic processes with PAES. The observed time-dependent Auger intensities are interpreted as the segregation of Cu in a Pd substrate.
Finally, the unprecedented high energy resolution allowed for the first time the observation of the double peak structure of the Cu $M_{2,3}$VV-transition with PAES.

Thus, within this thesis two objectives were achieved: Firstly, the PAES spectrometer was renewed and improved by at least one order of magnitude with respect to the signal to noise ratio, the measurement time and the energy resolution. Secondly, several measurements have been carried out, demonstrating the high performance of the spectrometer. Amongst them are first dynamic PAES measurements and a high resolution measurement of the Cu $M_{2,3}$VV-transition.

Zusammenfassung

Die umfassende Charakterisierung von Oberflächen und Oberflächenprozessen ist sowohl in der Oberflächenchemie, als auch in der Oberflächenphysik von herausragendem Interesse. Eine typische Untersuchungsmethode in diesem Zusammenhang ist die **E**lektronen induzierte **A**uger **E**lektronen **S**pektroskopie, EAES. Obwohl EAES als oberflächensensitive Methode anerkannt ist, wird bei der EAES über mehrere Atomlagen gemittelt. Im Gegensatz dazu wird mit der sogenannten durch **P**ositronenannihilation induzierte **A**uger **E**lektronen **S**pektroskopie, PAES, tatsächlich fast nur die erste Atomlage untersucht.

Obwohl PAES im Vergleich zu EAES eine höhere Element-Selektivität und Oberflächensensitivität bietet, wird sie dennoch bis heute kaum eingesetzt. Der Hauptgrund dafür sind die sehr langen Messzeiten, die bisher für ein einziges PAES-Spektrum notwendig waren. Daher war es das Ziel dieser Dissertation, das bestehende PAES-Spektrometer an der hochintensiven Positronenquelle NEPOMUC (**NE**utron induced **PO**sitron source **MU**ni**C**h) bezüglich der folgenden Aspekte zu verbessern:
Erstens sollte die Messzeit, welche zuvor bei etwa 12 h lag auf ca. eine Stunde oder sogar noch weniger reduziert werden. Zweitens sollte die Energieauflösung von bislang $\Delta E/E \approx 10\%$ um wenigstens eine Größenordnung verbessert werden, um hochaufgelöste PAES-Messungen zu ermöglichen und somit mehr über den Auger-Prozess als solchen erfahren zu können.

Um diese Ziele zu erreichen, wurde am bestehenden PAES-Spektrometer ein neuer Elektronenenergieanalysator in Betrieb genommen. Dafür musste der Großteil der restlichen Analysekammer angepasst werden. Insbesondere die Probenhalterung und die Positronenstrahlführung wurden neu konzipiert. Die Linsenspannungen wurden mit dem Simulationsprogramm SIMION® optimiert.

Nach der Justage des neuen Analysators und seiner Komponenten wurden erste Messungen durchgeführt, die das Erreichen der gesteckten Ziele verdeutlichen:
Zunächst wurde die Messzeit für ein Übersichtsspektrum von drei Stunden auf bis dahin unerreichte 420 s verkürzt. Damit sind zum ersten Mal mit PAES Zeitskalen erreicht, die mit konventionellen Methoden wie EAES vergleichbar sind. Die Messzeit für ein detaillierteres Auger-Spektrum wurde von 12 h auf nur 80 min reduziert. Im Vergleich zu anderen PAES-Spektrometern ist das sehr kurz, da die Messzeit sonst oft noch im Bereich von einigen Tagen liegt. Des weiteren wurde die Qualität des Spektrums, das Signal zu Untergrund-Verhältnis, um eine Größenordnung verbessert. Außerdem wurde die relative Energieauflösung auf einen Wert von $\Delta E/E < 1\%$ erhöht.

Mit den soeben genannten technischen Verbesserungen konnten einige vollkommen neue Messungen durchgeführt werden: Die Oberflächensensitivität und Element-Selektivität von PAES wurde anhand einer Untersuchung von Pd und Fe, bedampft mit unterschiedlich dicken Cu-Schichten, gezeigt. Bei PAES stellte sich heraus, dass bei einer Bedeckung von Fe mit nur 0.96 Atomlagen Cu bereits mehr als 55% der detektierten Augerelektronen von Cu stammen. Wurde dieselbe Probe mittels EAES gemessen, belief sich der Cu-Anteil hingegen auf weniger als 6%. Bei der Pd-Probe mit 0.96 Atomlagen Cu stammten bei der Untersuchung mit PAES mehr als 30% der Augerelektronen vom Cu, wohingegen bei der EAES nicht einmal 5% der Augerelektronen von Cu kamen. Der große Unterschied in den Intensitäten bei der Messung mit PAES wird durch die sich stark unterscheidenden Positronenaffinitäten der verwendeten Elemente erklärt.
Außerdem ermöglichte die kurze Messzeit zum ersten Mal die Beobachtung dynamischer Prozesse mit PAES. Die gemessenen zeitabhängigen Augerintensitäten werden als Segregation von Cu in Pd interpretiert.
Schließlich erlaubte die für PAES beispiellose Energieauflösung zum ersten Mal die Messung der Doppelpeak-Struktur des Cu $M_{2,3}$VV-Übergangs mit PAES.

Es wurden in dieser Arbeit also zwei Hauptziele erreicht: Erstens wurde das PAES-Spektrometer technisch modifiziert, insbesondere wurde die Energieauflösung, das Signal zu Untergrund-Verhältnis und die Messzeit um wenigstens eine Größenordnung verbessert. Außerdem wurden mehrere Messungen durchgeführt, welche die Leistungsfähigkeit des Spektrometers aufzeigen. Besonders hervorzuheben ist die erste Untersuchung eines dynamischen Prozesses mittels PAES und die hochaufgelöste Messung des Cu $M_{2,3}$VV-Übergangs.

Contents

1 Introduction **1**

2 Positrons at surfaces **3**

2.1 Properties of the positron 3

2.2 Positron sources 4

2.2.1 Radioactive isotopes 4

2.2.2 Pair production 4

2.3 Positrons in matter 6

2.4 Positrons at surfaces 8

3 Theory and principle of EAES and PAES **11**

3.1 The Auger transition 11

3.1.1 Principle of the Auger effect 11

3.1.2 Nomenclature of Auger transitions 13

3.1.3 Energy of Auger electrons 13

3.2 Electron induced Auger electron spectroscopy 14

3.3 Positron annihilation induced Auger electron spectroscopy 16

4 Setup for positron annihilation induced Auger electron spectroscopy **21**

4.1 Setup of PAES-spectrometers 21

4.1.1 LEED setup 21

4.1.2 Cylindrical mirror analyzer 23

4.1.3 Time of flight method 23

4.1.4 Concentric hemispherical analyzer 25

4.2 Setup at NEPOMUC 28

4.2.1 Vacuum chambers and installed instruments 28

4.2.2 Vacuum system 33

4.2.3 Beam guidance 33
4.2.4 Concentric hemispherical analyzers at NEPOMUC 37

5 Measurements and results 43
5.1 Status of PAES at NEPOMUC before this thesis 43
5.2 Sample preparation 44
5.3 Improvements of the PAES spectrometer 45
5.4 Short term PAES-measurement 47
5.5 High resolution PAES of the Cu $M_{2,3}$VV-transition 47
5.6 High purity materials 49
5.6.1 PAES spectra of Fe, Ni, Cu, Zn, Pd and Au 49
5.6.2 Correlation of Auger intensity and binding energy 51
5.7 Sub-monolayers of Cu on Pd and Fe 52
5.7.1 Preconditions for the interpretation of the data 52
5.7.2 Preparation of the layered samples 53
5.7.3 EAES and PAES measurements of Cu/Pd 53
5.7.4 EAES and PAES measurements of Cu/Fe 57
5.7.5 Comparison of the Cu/Pd and the Cu/Fe systems 58
5.8 Segregation of Cu in Pd 60
5.8.1 Time dependent measurement of Cu on Pd 60
5.8.2 Interpretation 61
5.9 Measurement of the positron work function 63

6 Conclusion and outlook 65

7 Appendix 67
7.1 Calculated core annihilation probabilities 67
7.2 Positron affinities 69

Bibliography 71

Acknowledgments 77

List of publications 79

Chapter 1

Introduction

The examination and detailed characterization of surfaces is of outstanding importance in solid state physics. The surface represents the interacting zone between the solid on the one side and another solid, a gas or a liquid on the other. The processes at the surface e.g. diffusion, segregation, catalysis or corrosion are manifold and complex and hence topic of current research.

Typical analysis methods use often photons or electrons as primary particles. The detected particles are normally electrons in an energy range below several keV, due to their intrinsically short information depth. Typical methods are e.g. **X**-ray induced **P**hoto electron **S**pectroscopy (XPS), **L**ow **E**lectron **E**nergy **D**iffraction (LEED) or **E**lectron induced **A**uger **E**lectron **S**pectroscopy (EAES). Corresponding instruments can be purchased commercially and the measurement methods are well established in industry and research.

Additionally, there are more exotic investigation methods, which require a more complex setup, but yield very specific information. Among these is **P**ositron annihilation induced **A**uger **E**lectron **S**pectroscopy (PAES). In the past it suffered from long measurement times and was thus not often used.

PAES was invented at the university of Texas, Arlington by A. Weiss [WMJ$^+$88]. It is an extremely surface sensitive, elemental selective, and non destructive measurement method. In contrast to conventional EAES, the primary hole in the atomic shell is created via matter antimatter annihilation and not via electron impact. Thus, the energy of the positrons can be chosen as low as technically possible, typically not more than 20 eV. Due to this low implantation energy, the secondary electron background ends at that low incident energy, and hence the Auger peaks, which occur at energies > 20 eV, can be observed without disturbing secondary electron background.
Furthermore, the implantation site and the annihilation site of the thermalized positron do not coincide, since the positron diffuses prior to its annihilation. PAES is hence a non destructive investigation method, even at an atomic scale.
The third advantage of PAES compared to conventional EAES consists in the much higher surface sensitivity and the high elemental selectivity. The former is due to the fact that low energy positrons are trapped in a surface state and hence up to 95% of

the Auger signal stems from the topmost atomic layer [WMJ+88, SL88, JW90]. The reason for the elemental selectivity is the so-called positron affinity, which makes elements differently attractive for positrons.
Although the Auger electron yield, i.e. the number of Auger electrons per incident particle, is roughly two orders of magnitude higher in PAES compared to EAES [BS83, Col00, HMS07], the main drawback of PAES so far consisted in the low available positron intensities, leading to measurement times for PAES of up to three weeks [Str02]. This is overcome with the highly intense positron source NEPOMUC (**NE**utron induced **PO**sitron source **MU**ni**C**h) at the research reactor Heinz-Meier Leibnitz [HSSS06].

Within this thesis several major improvements have been achieved, which make PAES very attractive for future studies in surface science. The high positron intensity and the installation of a new electron energy analyzer reduced the measurement time to unprecedented time scales for PAES of the order of minutes. In addition, the energy resolution was enhanced significantly. The modifications of the installed PAES spectrometer that led to those improvements, and the completely novel measurements will be presented in this work.

The thesis is structured as follows: Chapter 2 deals with the production of positrons and their interaction with matter. The main focus is drawn to effects of positrons at surfaces. Chapter 3 covers the Auger effect in general and the comparison between EAES and PAES. In Chapter 4 the setup of the PAES spectrometer at NEPOMUC and its development stages are explained. Chapter 5 presents the performed measurements, starting with a comparative spectrum of polycrystalline Cu that visualizes the improvements. Next, a short term PAES measurement of Cu is presented with the shortest recording time reported so far. Then, a line shape measurement of the Cu $M_{2,3}$VV-transition with unprecedented high energy resolution is shown. This is followed by elemental selective measurements of samples, coated with Cu in the sub-monolayer range. After this, the first dynamic PAES measurement is presented, the segregation of Cu in Pd. The chapter ends with the measurement of the energy distribution of moderated positrons, which aims for the study and development of new positron moderation materials. A short summary and an outlook about future developments of PAES conclude the work.

Chapter 2

Positrons at surfaces

As for every positron measurement a positron source is inevitable this chapter deals with the production of positrons. Additionally the properties of positrons and their interaction with matter will be described. Since positrons do not annihilate instantaneously, when they encounter matter, but after some hundred picoseconds, several processes in the bulk and at the surface of a sample are possible. As this work focuses on the Auger effect, the main attention is drawn on processes related to positrons at the surface.

2.1 Properties of the positron

The positron was postulated by P. Dirac in 1929 [Dir30] and only three years later C. Andersson revealed its existence experimentally [And33]. The physical properties of the positron are apart from the sign of the charge and the sign of the magnetic moment identical to the properties of the electron. The properties of a positron are summarized in Table 2.1.

rest mass m_0	$9.10938215(45) \cdot 10^{-31}\,\mathrm{kg}$
rest energy	$0.510998910(13)\,\mathrm{MeV}$
charge	$1.602176487(40) \cdot 10^{-19}\,\mathrm{C}$
magnetic moment	$1.00115965218111(74) \cdot \mu_\mathrm{B}$
spin	1/2
lifetime in vacuum	$\tau > 2 \cdot 10^{21}\,\mathrm{a}$

Table 2.1: Physical properties of the positron [MTN08, SL88].

If a positron encounters an electron in the absence of a third particle they annihilate at least into two gamma quanta. Typical is the annihilation into two gamma quanta of each 511 keV, measured in the positron-electron rest frame. The probability of the annihilation into three gamma quanta with continuous energy distribution is reduced

by a factor of 370 [OP49]. The electron density $n(r)$ at the annihilation site influences strongly the lifetime of the positron and the energy distribution of the emitted gamma quanta [Wes73].

In gases, semiconductors or at the surface of metals the formation of positronium (Ps) is possible. Ps is a bound state of a positron and an electron and has a binding energy of 6.8 eV. Depending on the spin orientation of electron and positron, Ps has a lifetime of 125 ps in the case of para-Ps and 142 ns in the case of ortho-Ps. The spin orientation results in the annihilation of p-Ps into an even number of photons, whereas o-Ps annihilates into an odd number of photons [Col00].

2.2 Positron sources

The positron source can either be a radioactive isotope, i.e. a β^+-emitter, or a large scale facility where positrons are produced via pair production.

2.2.1 Radioactive isotopes

For lab-based positron experiments radioactive isotopes ${}^A_Z X$ with neutron deficiency are used. Thus, they decay as follows:

$$ {}^A_Z X \rightarrow {}^A_{Z-1} X + \mathrm{e}^+ + \nu_e \quad . \tag{2.1} $$

Since the released energy is shared between the positron and the electron neutrino ν_e, the β^+-spectrum of the emitted positrons extends over a large energy range with a well defined end point energy, see Figure 2.1. The process of moderation, whose result is also shown in Figure 2.1 will be discussed shortly in Section 2.4. ^{22}Na is often used for lab based positron beams due to its long half-life of 2.6 a and the 1275 keV gamma quantum, which is emitted promptly with the positron. Due to self absorption the activity of a radioactive positron source with reasonable size is limited to about 3.7 GBq [SL88]. Thus, another approach is needed to produce positron sources with higher intensities. The latter are desirable, since the measurement times with radioactive isotopes are long and for some experiments, e.g. PAES extend up to several days [Str02].

2.2.2 Pair production

Using the principle of pair production, positron sources with high intensities become possible. Therefore, highly intense gamma sources available at LINACs (**LI**near **AC**celerators) or research reactors are needed and intensities of up to $9 \cdot 10^8 \, \frac{\mathrm{e}^+}{\mathrm{s}}$ are achieved [HLM$^+$08]. Pair production corresponds to the „inverse annihilation“ process:

$$ \gamma \rightarrow \mathrm{e}^+ + \mathrm{e}^- \quad , \tag{2.2} $$

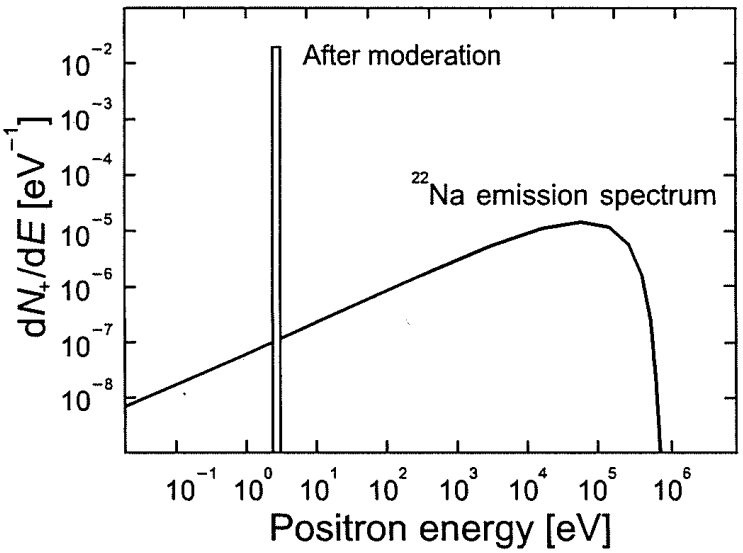

Figure 2.1: Energy spectrum of positrons emitted from a ^{22}Na-source. The end point energy of ^{22}Na amounts to 545.7 keV [Fir05]. The effective process of remoderation is also shown [KRL99]. Its explanation is given in Section 2.4.

where the energy of the γ-quantum must exceed 1022 keV. Due to momentum conservation pair production is only possible in the vicinity of another particle. Since the cross section for this process increases approximately with Z^2 [Col00], high Z conversion materials such as tungsten or platinum are used.

In the case of a LINAC based positron beam the high energy γ-radiation originates from Bremsstrahlung, when the relativistic electrons are stopped at a cooled target [KRBJ$^+$08, SOM$^+$97].
At reactor based beams either the high γ-flux near the fuel element is used directly for pair production [vVSdR$^+$01] or thermal neutrons are converted via a (n, γ)-reaction into high energy γ-radiation [KS90]. The latter possibility is realized at the NEPOMUC beam at the research reactor Heinz Meier-Leibnitz FRM II in Munich. NEPOMUC uses the high cross section of ^{113}Cd ($\sigma_{n,therm} = 20600$ barn) to capture thermal neutrons. Afterwards, the de-excitation of the excited ^{114}Cd via the emission of γ-quanta is used to produce e^+-e^- pairs in a platinum structure. Platinum is used not only due to its high Z, but also because it acts as a positron moderator, see Chapter 2.4. With adequate positive voltages applied to the lenses the positrons are released into the solenoidal guiding field, see Figure 2.2. A more detailed description of NEPOMUC is found in literature [HKR$^+$02b, HKR$^+$02a, HLM$^+$08].

Out of the reactor tank, there is a remoderator installed, which enhances the brightness of the positron beam and thus reduces the beam diameter. The positrons are then guided to a beam switch, where one of presently five experiments is fed.

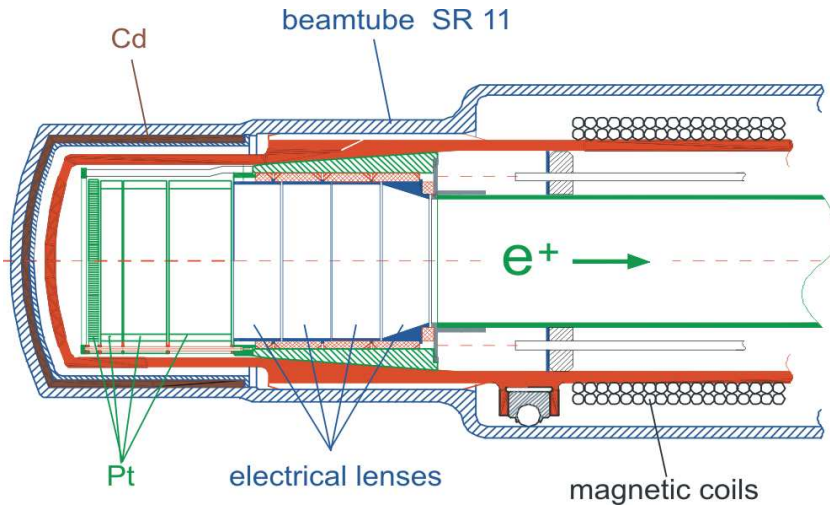

Figure 2.2: Beam tube tip of the in pile positron source NEPOMUC at the research reactor FRM II. ^{113}Cd captures thermal neutrons with a high cross section and emits high energy γ-radiation, which is then converted in electron-positron pairs. The electric lenses and the magnetic coils form the beam and guide the positrons to the experiments.

2.3 Positrons in matter

When a positron beam encounters matter several processes are possible, see Figure 2.3. First, if the positrons are not backscattered (in)elastically, they penetrate the sample, where the maximal range depends on their energy. The Makhovian implantation profile describes the depth distribution of positrons and results in a mean implantation depth of $\approx 0.1\mu$m for a 3 keV positron [Mak61]. The energy loss mechanism at high energies (keVrange) is dominated by ionization, in the middle energy range (several 100 eV) by electron-hole excitations and plasmon excitations, and at low energies (from roughly 25 eV down to thermal energies) positrons loose their energy only via phonon scattering and conduction electron scattering [RLG$^+$93]. After the thermalization of the positrons ($t < 10 \cdot 10^{-12}$ s), they can diffuse through the solid up to several hundred nm and eventually they get trapped in a lattice defect. Due to the low intensity of positron beams, there is always only one positron at a time in the sample. Hence the Pauli-principle does not limit the possible energies of a positron, but every positron can slow down to thermal energies and no positron-positron exchange interaction needs to be regarded. Thus, a positron in a solid will occupy the energetically lowest state.

Since open volume defects, such as mono vacancies or lattice mismatches, are attractive potentials, positrons get trapped there with high probability. Thus, positrons can be used as an active micro probe for defect studies and concentrations of only 10^{-6}defects/atom are detectable. If the surface is within the diffusion length, the positrons can diffuse back to the surface. The effects that occur there are described in Section 2.4.

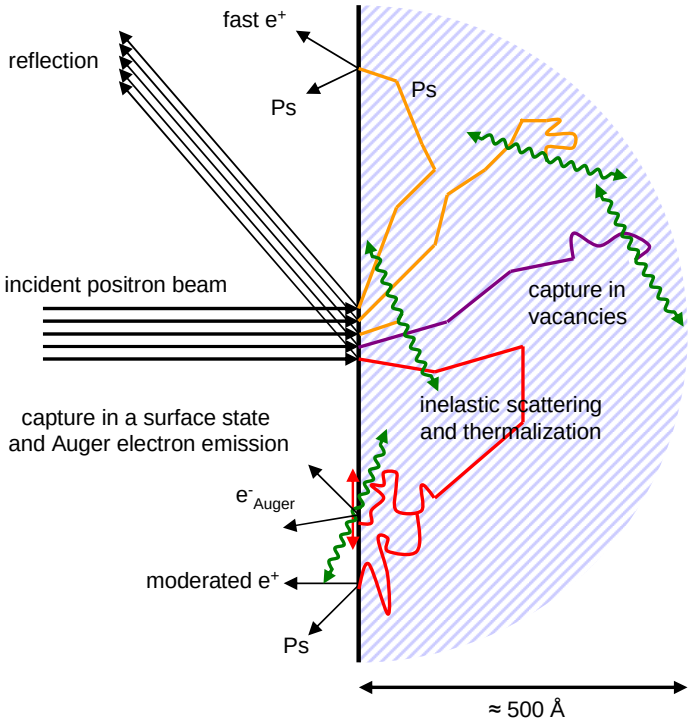

Figure 2.3: Fate of positrons in matter. Most important in this work is the effect, shown at the bottom of this figure, where positrons are caught in a surface state before their annihilation. With a probability of several percent such an annihilation is followed by the emission of an Auger electron.

Certainly, the positrons can annihilate at any time during the processes just explained. The positron lifetime is typically of the order of several hundred picoseconds. The electron density and the momentum distribution at the annihilation site influence strongly the shape of the annihilation line and the lifetime of the positrons. In most positron experiments applied in solid state physics these two parameters are measured and analyzed.
Lifetime experiments exploit the type and concentration of vacancies in a sample (e.g. [PR99]), CDBS (**C**oincident **D**oppler **B**roadening **S**pectroscopy) probes the chemical environment of the annihilation site (e.g. [HPSS08]). AMOC (**A**ge **MO**mentum **C**orrelation) combines the latter two methods and with ACAR (**A**ngular **C**orrelation of **A**nnihilation **R**adiation) it is possible to determine Fermi surfaces (e.g [LDD+07]) without the necessity to apply a magnetic field and to measure at low temperatures as required e.g. for the de Haas-van Alphén effect. An additional advantage of all described positron techniques is that they are non destructive and that the samples are not activated after the measurement.

2.4 Positrons at surfaces

Since positrons that are trapped in a surface state are the fundamental prerequisite for the surface sensitivity of PAES, the reasons why they are trapped at all at the surface will be elucidated in the following.

Low energy positrons implanted in a solid are thermalized within ps and then diffuse through the solid. The diffusion time has a typical value of $1 \cdot 10^{-10}$ s, the positron lifetime amounts to roughly $(2 - 4 \cdot 10^{-10}$ s). If the surface is within the diffusion length, the positrons get trapped there. In such a surface state positrons live typically $4 - 6 \cdot 10^{-10}$ s [SL88]. Figure 2.4 shows the calculated potential and the wave function for a positron at a Si(110) surface. It can be seen, that the potential has a minimum right at the surface and consequently the positron ground state wave function has its maximum there. This is due to the fact that the positively charged nuclei repulse the positron, while the electron distribution at the surface attracts the positron.

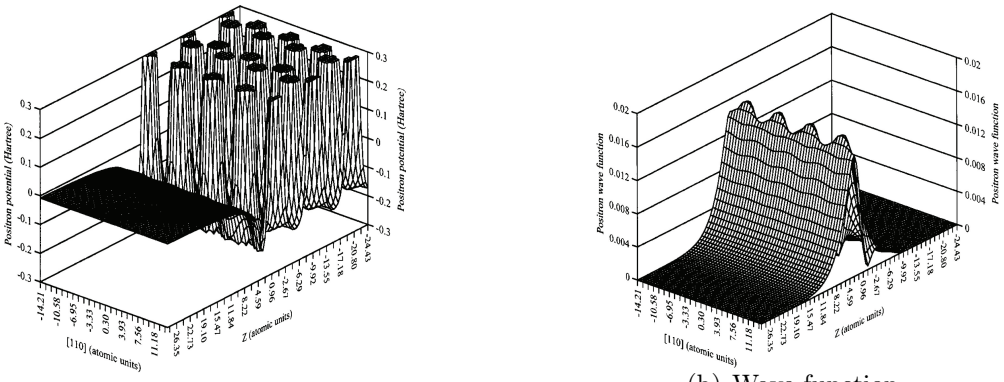

(a) Potential (b) Wave function

Figure 2.4: Calculated potential and ground state wave function for a positron at a clean Si(110) surface [FFW04].

In order to understand the form of the potential qualitatively, the single contributions to the potential for a positron in a solid $V_+(r)$ are explained in the following [BPN87]:

$$V_+(r) = -V_{Coul}(r) + V_{corr}(n(r)) \quad . \tag{2.3}$$

Here, $V_{Coul}(r)$ contains the Coulomb potential of the nuclei and also the Hartree potential of the electron density $n(r)$. $V_{corr}(n(r))$ stands for the correlation potential that describes the effects due to the short range pileup of electrons near the positron. The potential for an electron is given by

$$V_{eff}(r) = V_{Coul}(r) + V_{xc}(n(r)) \quad , \tag{2.4}$$

where $V_{Coul}(r)$ is the same potential as above. Due to the opposite charge of the electron, the sign of $V_{Coul}(r)$ is changed. $V_{xc}(n(r))$ signifies the exchange correlation potential at the point r, which depends solely on the electron density. Figure 2.5 shows the

calculated potentials at an aluminum surface for electrons (left) and positrons (right). Here, three other quantities occur: the work function Φ, the chemical potential μ and the surface dipole barrier Δ. The index „+“ and „-“ distinguishes between positrons and electrons.

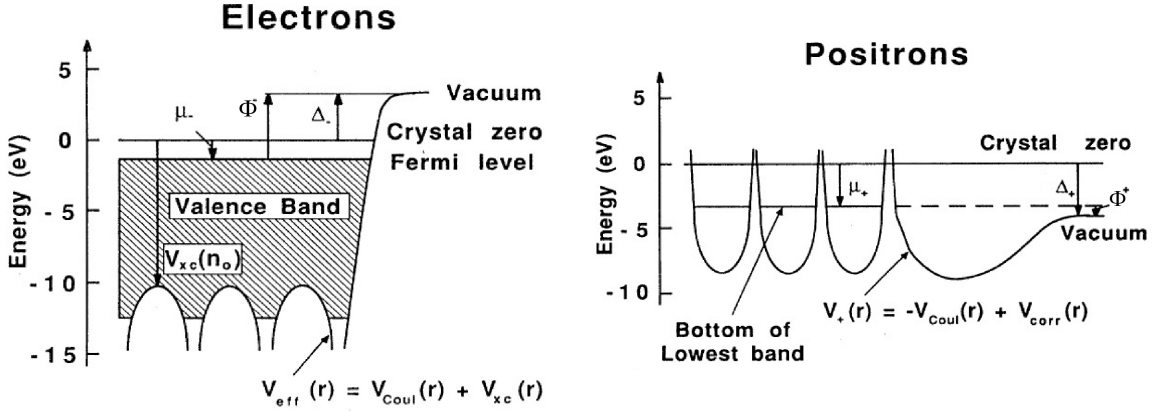

Figure 2.5: Comparison of the potentials for electrons (left) and positrons (right) at the surface of aluminum. Φ^- and Φ^+ denote the electron and the positron work function, respectively. μ_- and μ_+ stand for the electron and positron chemical potential, and $\Delta_- = -\Delta_+$ are the electron and positron dipole potentials. $V_{Coul}(r)$ denotes the Coulomb potential of nuclei and the electron charge density, $n(r)$. $V_{xc}(n(r))$ is the exchange correlation potential, which depends on $n(r)$. $V_{corr}(n(r))$ is the potential that describes the lowering due to the electron pile up near a positron (after [PLN89]).

The surface dipole barrier Δ is the energy difference between the crystal zero level and the vacuum level. It is equal for electrons and positrons in its absolute value, but contrary in its sign. The chemical potential for electrons, μ_-, is defined as the distance between the Fermi level and the crystal zero, whereas the chemical potential for positrons, μ_+, is defined as the difference between the bottom of the lowest band and the crystal zero. Finally, the work function Φ stands for the energy, which is needed to remove an electron/positron from the bulk of the material into the vacuum. It can be calculated as

$$\Phi = \Delta - \mu \quad . \tag{2.5}$$

Φ^- is positive, since the dipole barrier for electrons is usually positive and the chemical potential is negative. Thus, energy is required for the removal of an electron from the bulk of a sample. Φ^+ in comparison, can also be negative. This means that thermalized positrons can be emitted with a discrete energy. If the right hand side of Figure 2.5 is considered, one might expect that all positrons reaching the surface might be emitted with discrete energy, since the vacuum level is below μ_+. This is not the case, because phonon scattering reduces in some cases the energy of the positron. Thus, it gets trapped in a surface state.

As the shape of the positron potential is now explained, the processes that can occur when a positron reaches the surface will be explained in the following. Three different processes are distinguished:

- If the sample material has a negative positron work function, $\Phi^+ < 0$, the thermalized positrons can be emitted perpendicularly to the surface with a sharp energy. This effect is used for the so-called positron moderation. With this moderation process it is possible to generate highly brilliant positron beams, see e.g. [Col00, SL88, Pio09].

- The second possibility for a positron arriving at the surface is the capture of the positron in a delocalized surface state. If the positron does not annihilate with a valence electron, it annihilates with a certain probability, the so-called *core annihilation probability* p_{core}, with a core electron. p_{core} is a crucial factor for the Auger signal intensity and is thus discussed in detail in Section 3.3. Subsequent to the annihilation the atomic shell is in an excited state and the emission of characteristic X-rays or the emission of Auger electrons is possible. Which process is dominating and the Auger process itself is described in Chapter 3.

- The third possible fate is the formation of positronium, Ps. In most cases, it is built when the positron arrives at the surface, where it picks up an electron and leaves the solid as Ps. The other possibility, even tough far less probable is the formation of Ps by a positron which is already captured in a surface state. Because the binding energy of 6.8 eV is gained, the escape of Ps from the surface well gets possible [Col00].

Chapter 3

Theory and principle of EAES and PAES

This chapter deals with the Auger process in general first. This is common to EAES and PAES, which only differ in the creation of the primary hole. Then, the specialities of EAES and PAES will be compared, in particular the surface sensitivity and elemental selectivity, the signal to noise ratio and the extent of damage due to the primary particles.

3.1 The Auger transition

The Auger effect, for the first time discovered by Lise Meitner in 1922 [Mei22] and three years later by Pierre Auger [Aug25] independently one from another, is a radiationless atomic transition. Today, Auger electron spectroscopy is a standard method for the elemental surface analysis in industry as well as in research. Complete Auger spectrometers can be purchased from several manufacturers.

3.1.1 Principle of the Auger effect

The Auger transition ABC consists basically of three steps, see Figure 3.1. First, an electron from the level A of an atom is removed via electron capture, internal conversion, a high energy electron, a photon, an ion or a positron. The resulting hole is then filled from another electron of a higher level B. The released energy is emitted either via a photon, resulting in the emission of X-rays with characteristic energy or via the radiationless emission of an electron with sharp energy, the Auger electron from level C. The Auger electron has a sharp energy corresponding to the electron levels of the element, where it is produced. Even the binding state of an atom is seen in a chemical shift (on the order of several eV) of the Auger electron. In contrast to X-ray photoelectron spectroscopy (XPS), the energy of the Auger electron does not depend on the energy of the initializing particle.

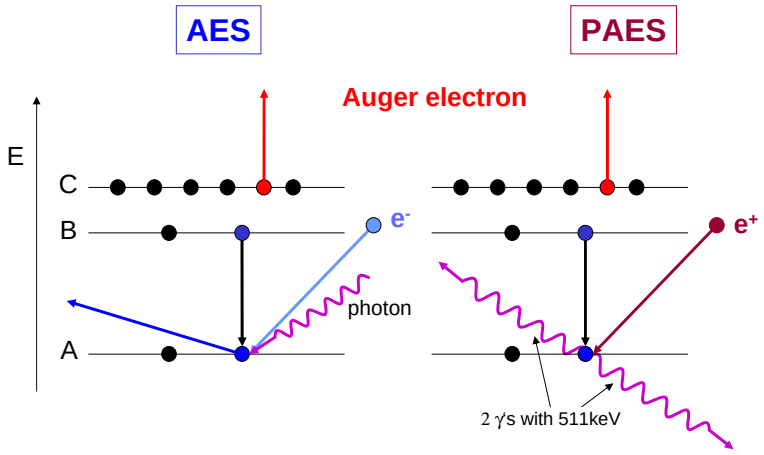

Figure 3.1: Principle of AES and PAES. On the left-hand side, the primary hole is created via impact of an high energy electron (EAES) or a photon (XAES), respectively. On the right-hand side, the primary hole is produced via matter antimatter annihilation of an electron and a positron. The subsequent Auger effect is almost identical in all three cases and leaves the atom doubly ionized.

Whether the exited atom emits a photon or an Auger electron, depends on the shell in which the atom was ionized. The lighter the element and the outer the shell is, the more likely is the emission of an Auger electron, see Figure 3.2. For a rule of thumb the binding energy of the primary electron can be considered: if it is less than 2 keV, the emission of Auger electrons is preferred [BS83].

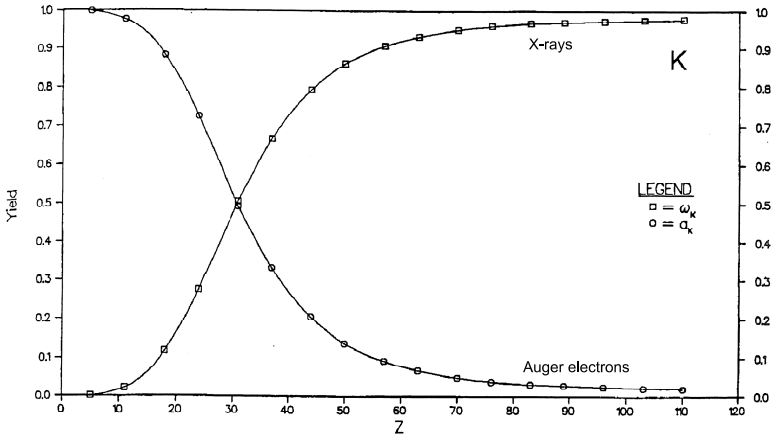

Figure 3.2: Yield for non Coster-Kronig Auger transitions (open circles) and for the emission of characteristic X-rays (open squares) for an atom, ionized in the K-level as a function of the atomic numer Z, from [Kra79].

3.1.2 Nomenclature of Auger transitions

Every Auger transition is described by an unambiguous nomenclature, e.g. KL_1L_2. This follows the participating electron energy levels, whereas the levels are named in the way of the X-ray spectroscopy: The main quantum number ($n = 1, 2, 3$ etc.) is represented by capital letters K, L, M etc. . The subscript stands for the combination of the orbital angular momentum ($l = 0, 1, 2\ldots$) and the respective electron spin, hence $j = l + s$. The total angular momentum j takes values of $1/2, 3/2, 5/2$, etc. and is denoted by an integer subscript, starting with 1. If two energy levels are close to each other, both levels can be excited and the transition is denominated by both levels, e.g. $M_{2,3}$. In the case, that the electron stems from the valence band it is common to name this level simply V. When two electrons from a level with the identical principal quantum number are involved, the process is called Coster-Kronig transition (e.g. L_1L_2M). If even all electrons originate from the same level, the transition is named Super-Coster-Kronig transition (e.g. $M_{2,3}M_{4,5}M_{4,5}$) [CK35].

When the Auger effect was observed first, it was thought to be an effect with two independent steps: first, a X-ray quantum is produced, which then initiates an internal photo effect. Though this is energetically possible, the selection rules for dipole transitions ($\Delta l = \pm 1$) are not obeyed, e.g. for an actually observed KL_1L_1-transition. Hence, the Auger effect must be a radiationless three electron process [BS83].

3.1.3 Energy of Auger electrons

The discrete energy of an Auger electron of the transition ABC can be calculated in a first estimation according to the following formula [CJ70]:

$$E_{ABC} \approx E_A(Z) - \frac{1}{2}[E_B(Z) + E_B(Z+1)] - \frac{1}{2}[E_C(Z) + E_C(Z+1)] - \Phi^- \quad . \tag{3.1}$$

Here, $E_i(Z)$ denotes the electron binding energy of the respective level ($i = A, B, C$) with the atomic number Z. Since the atom is singly ionized after the creation of the primary hole, the binding energies must be corrected, which is expressed in the second and third term of Equation 3.1. As the Auger electron is emitted from the bulk of a sample, also the electron work function Φ^- must be taken into account.

For a more accurate calculation of the Auger electron energies, the correlation $\mathscr{F}(BC : x)$ between the holes in the shells B and C in the final state x as well as the relaxation energies R_x^{in} and R_x^{ex} must also be taken into account [BS83]:

$$E_{ABC} = E_A - E_B - E_C - \mathscr{F}(BC : x) + R_x^{\text{in}} + R_x^{\text{ex}} - \Phi^- \quad . \tag{3.2}$$

When the relaxation, i.e. the inward collapse of outer electronic orbitals, takes place, there is an increased Coulomb and exchange interaction between electrons in outer and inner orbitals. R_x^{in} accounts for the intra-atomic relaxation energy, i.e. the relaxation energy appropriate for an isolated atom. If the excited atom is in a solid or a molecule, interactions with other atoms or the valence band occur and thus also the extra-atomic

relaxation energy R^{ex} must be taken into account. Those correction terms can be considerable in their magnitude and must not be neglected.

The Auger electron energies for the different materials can be found in several standard books about Auger electron spectroscopy, e.g. in [BG03, PRWM72].

The width of the Auger peaks (in gases) is given by the lifetimes of the vacancies involved. As the lifetime is on the order of 10^{-16} s, the widths are calculated by the uncertainty principle to values of 0.5 eV. Holes in weakly bound levels have larger lifetimes than holes in strongly bound levels unless Coster-Kronig transitions are allowed. Coster-Kronig transitions show widths on the order of 2 eV. Those considerations hold for Auger electrons emitted from free atoms.
If the Auger electrons are emitted from a solid, various environmental factors must be regarded. Not taking into account the instrumental broadening, the major broadening factors are:

- valence band effects
- chemical shifts
- energy loss processes (e.g. plasmon losses).

An excellent description of the Auger effect is found in [Cha76].

3.2 Electron induced Auger electron spectroscopy

The most common way to initiate the Auger process is the ionization via electron impact (**E**lectron induced **A**uger **E**lectron **S**pectroscopy, EAES) or a photon (**X**-ray induced **A**uger **E**lectron **S**pectroscopy, XAES). Here, EAES will described more explicitly, since it was used during this thesis. A detailed explanation of XAES is found e.g. in the book of D. Briggs [BG03].

EAES uses electrons with an energy of $2-10$ keV for the initiation of the Auger process. The energy must be chosen that high, because the efficiency to produce a hole is highest if the kinetic energy of the electron amounts to the fivefold binding energy, and the Auger process occurs for electrons with a binding energy of up to 2 keV [BG03, BS83]. Due to the high energy of the primary electron beam, the electrons penetrate the sample up to 2 µm. Hence, secondary electrons of a large energy range are emitted from the sample, which makes it sometimes hard to observe the Auger peaks at all, since the secondary electron background contains roughly 10^6 as many electrons than the Auger peak. At this point it should be mentioned that in this thesis the term „secondary electrons“ refers to all electrons, which contribute to the background of an electron spectrum, including „true“ secondary electrons as well as inelastically scattered primary electrons. This is important, since in some textbooks „secondary electrons“ refer only to background electrons in the energy range below 100 eV, the so-called true secondaries, see e.g. [BS83, Col00].

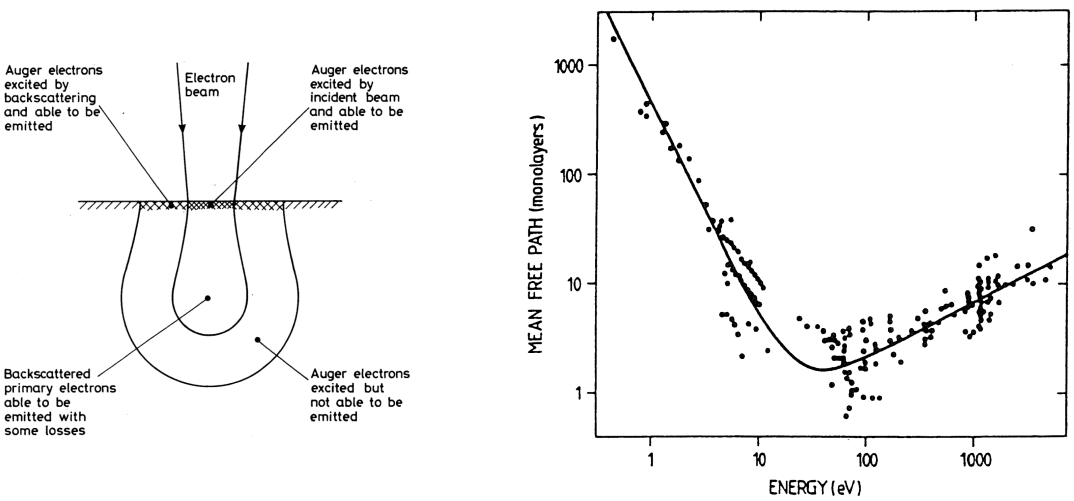

Figure 3.3: Left: the volume is shown, where secondary electrons and Auger electrons are produced. Right: IMFP of electrons for different elements. Not the penetration depth of the primary electron beam determines the information depth, but the IMFP of the excited Auger electrons. Typically, up to 10 atomic layers are probed with EAES [BS83].

The left side of Figure 3.3 shows the large volume, where Auger electrons and secondary electrons are produced upon the impact of an electron beam. But only the Auger electrons from the first 5-10 atomic layers contribute to the Auger peak in an electron energy spectrum. All other Auger electrons loose their energy information due to inelastic scattering in the sample and increase the electron background at lower energies. Hence, it is obvious that not the penetration depth of the primary beam determines the information depth of EAES, but the **I**nelastic **M**ean **F**ree **P**ath (IMFP) of the Auger electron. The dependency of the IMFP on the energy is plotted in the graph on the right hand side of Figure 3.3. The IMFP is almost independent of the elements (black data points).

Due to the high energy of the primary electron beam, slightly bound adsorbates with only a few eV binding energy can be removed. Thus, the sample is altered during the measurement, which has to be taken into account at EAES.

A typical EAES spectrum of a clean Cu (111) sample is shown in Figure 3.4. It can be seen that the Auger peaks are superimposed on a high secondary electron background. Several Auger transitions of outer electrons (Cu MVV) and stronger bound electrons (Cu LMM) are resolved.

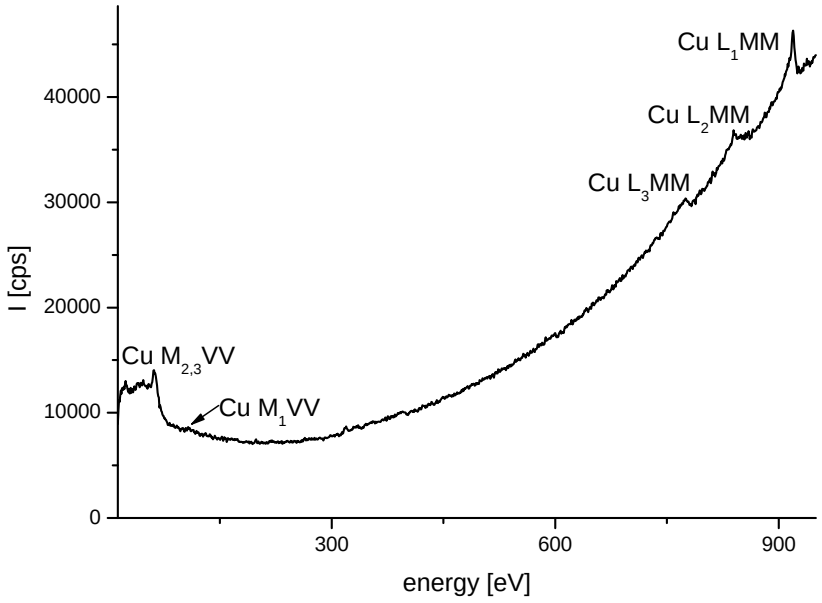

Figure 3.4: EAES spectrum of a clean Cu (111) single crystal, obtained with a primary electron beam energy of 2 keV.

3.3 Positron annihilation induced Auger electron spectroscopy

PAES, in contrast has several advantages, but other limitations. The major challenge is the low positron intensity compared to electron guns and the more complex setup for a positron beam. Whereas for EAES, it is convenient to buy an electron gun with its electronics, for PAES one has to set up a whole positron beam, including a positron source (β^+-emitter or a large scale facility), a moderation device and a beam guidance system (see Chapter 2). Even at NEPOMUC, the positron beam with the highest intensity of monoenergetic positrons, only $9 \cdot 10^8 \frac{e^+}{s}$ with an energy of 1 keV are available. After the remoderation stage and the guidance of the positron beam to the chamber, $9 \cdot 10^6 \frac{e^+}{s}$ with 20 eV energy reach the sample. This corresponds roughly to a positron current of 1 pA, whereas electron guns provide currents in the µA-range. Hence, the positron intensity is a limiting factor, since it prolongs the measurement time to several hours.

The major difference of PAES compared to EAES is the creation of the primary hole, which initiates the Auger process. At PAES, this hole is produced via matter antimatter annihilation, i.e. the annihilation of a core electron with a positron. The subsequent Auger process does not differ from EAES, still the advantageous consequences of the hole creation method are manifold.

First, since the electron is not removed via collision, but annihilation, the incident energy of the positrons can be chosen as low as technically possible. At NEPOMUC, a positron implantation energy of 20 eV is used. A consequence of the low positron

energy is that the secondary electron background, that makes quantitative analysis in EAES often difficult, ends at 20 eV. As the Auger electrons have mainly higher energies, the related peaks appear in a region without significant background, which enhances the signal to noise ratio (SNR) significantly. Whereas with EAES the typical SNR lies in the range of 1:2 or even worse, PAES reaches a SNR of 11:1 [HMS09], see Figures 3.4 and 3.5. Anyhow, there is still background observable at the low energy side of Auger peaks in a PAES spectrum, which leads to slightly asymmetric Auger peaks, see Figure 3.5. The reason for this asymmetry is that Auger electrons are emitted from the topmost atomic layer isotropically and hence inelastically backscattered Auger electrons contribute intrinsically to the line shape.

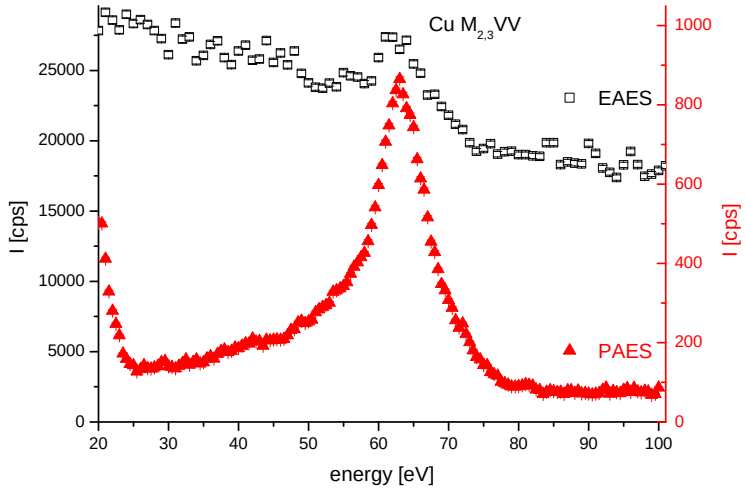

Figure 3.5: Comparison of EAES (open squares) and PAES (full triangles) at a polycrystalline copper foil. The energy of the incident positrons amounted to 20 eV and that of the impinging electrons to 2 keV. The secondary electron background has vanished completely with PAES in the range of the Cu Auger peak.

The second advantage of PAES is the extreme surface sensitivity and elemental selectivity. Since low energy positrons diffuse back to the surface (see Section 2.4), between 80% and 95% of the emitted Auger electrons stem from the topmost atomic layer of the specimen [WMJ+88, SL88, JW90]. This provides PAES with an extremly high surface sensitivity. High surface sensitivity can be also achieved with resonant XAES with the drawback of the high secondary electron background or with **A**uger **P**hotoelectron **C**oincidence **S**pectroscopy (APECS).
APECS detects the photoelectron, which is emitted with XAES, and the Auger electron in coincidence and thus reduces the secondary electron background considerably. Therefore two hemispherical electron energy analyzers are needed and due to the low coincidence count rates APECS is usually performed at synchrotron sources. Under certain conditions it is then possible to investigate only the topmost atomic layer [BJHK96]. However, the photons can remove weakly bound adsorbates.

The surface sensitivity of PAES originates from the backdiffusion of the positrons to the surface, see Section 2.4. The surface selectivity stems from the so-called positron affinity, A_+. It is calculated via the negative sum of the electron work function and the positron work function:

$$A_+ = -(\Phi^- + \Phi^+) \quad . \tag{3.3}$$

In general, A_+ is negative, which means that the positron is attracted. At an interface of two different materials or at a surface, where two different materials are present, positrons will be attracted to the element having the higher absolute positron affinity $|A_+|$. Hence, in all positron measurements the element with the higher absolute positron affinity $|A_+|$ is overestimated compared to its actual concentration. A table of the calculated positron affinities for various elements is given in Appendix 7.2.

Thirdly, PAES is also a non-destructive analysis method, since the position, where the positron impinges differs from the place where the Auger electron is emitted. Hence, adsorbates with low binding energies are not influenced or removed by the thermalized positrons. Furthermore, the electron shell of the ionized atom is barely excited by the low energy primary beam. This enables the observation of the undisturbed Auger transition from the topmost atomic layer of a sample. Due to the different ionization process, the line shape and the kinetic energies at PAES and EAES might differ.

Intensity of the Auger signal

The intensity of the Auger signal with PAES is determined by the core annihilation probability p_{core}, which was already introduced in Section 2.4. p_{core} is proportional to the overlap of the positron and electron density [JW90]:

$$p_{core} \propto \pi r_0^2 c \int d^3\vec{r} \cdot |\Psi_+(\vec{r})|^2 \cdot \left(\sum_i \left| \Psi_{nl}^i(\vec{r}) \right|^2 \right) \quad . \tag{3.4}$$

Here, r_0 denotes the classical electron radius ($r_0 = 2.818 \cdot 10^{-15}\,\mathrm{m}$), c is the speed of light in vacuum, Ψ_+ is the positron wave function and Ψ_{nl}^i stands for the core-electron wave functions, represented by free atom wave functions. The sum runs over the electron states in the atomic level, defined by the quantum numbers $n = 1, 2, 3 \ldots$ and $l = s, p, d \ldots$.

Evaluating the calculated core annihilation probabilities, a rough approximation for p_{core} was found [Col00]:

$$p_{core} \approx \frac{600 \cdot N(E_b)}{(E_b)^{1,6}} \quad , \tag{3.5}$$

where p_{core} is given in percent, E_b is the binding energy of the electron in eV and $N(E_b)$ is the number of electrons with E_b. Obviously, the core annihilation probability decreases with increasing binding energy due to the repulsive core potential. This formula calculates the core annihilation probabilities in the bulk of a sample, which amount up to 11%. At the surface, the value is roughly half the bulk value due to the

lower electron density. A table of calculated core annihilation probabilities is given in Appendix 7.1.

The Auger yield, i.e. the amount of Auger electrons per incident particle, amounts to 10^{-5} for EAES and 10^{-3} for PAES [BS83, Col00, HMS07]. The difference is mainly attributed to the fact that at EAES Auger electrons in a large volume are excited, but only Auger electrons from surface layers contribute to Auger peak in the electron spectrum. At PAES, in contrast, most of the excited Auger electrons are produced in the topmost atomic layer and hence their majority is emitted and detected without being scattered, fully contributing to the Auger signal.

Hence, PAES provides unique possibilities for fundamental studies, such as the observation of the line shape of Auger transitions [YZJ$^+$97, YZJW95, OSMY97, MSH09]. But also more applied research is possible, e.g. the study of thin layers in the sub-monolayer range or the observation of catalysis processes [MKJ$^+$90, KLM$^+$92, KLY$^+$92, MSH07].

Chapter 4

Setup for positron annihilation induced Auger electron spectroscopy

In this chapter, first the general setup of a PAES spectrometer is presented. Since the different PAES spectrometers differ mostly in their electron energy detection, this aspect will be elucidated. Then, the setup at NEPOMUC is described in detail. There, the main focus is drawn to the positron beam guidance and the performance of the used electron energy analyzers.

4.1 Setup of PAES-spectrometers

The general setup of a PAES apparatus is illustrated in Figure 4.1. Within a vacuum system a monoenergetic positron beam, a sample preparation unit and an electron energy analyzer have to be provided. The positron transport is mainly realized with a solenoid guiding field or Helmholtz coils. Also the sample preparation chamber is mostly the same at the different setups, containing a sputter gun, a sample heating unit and possibilities to coat the surface of the specimen (e.g. e^--beam evaporator and gas inlets).
The electron energy can be detected in various ways. As the energy detection presents a major part of PAES, some possibilities will be presented in further detail in the following.

4.1.1 LEED setup

The setup, which was used for the first PAES measurement [WMJ+88], consisted of a modified LEED (**L**ow **E**lektron **E**nergy **D**iffraction) setup. A LEED setup comprises an electron/positron beam guidance system and the detector system, see Figure 4.2. The detector is built of three or four hemispherical, concentric grids, a hemispherical and concentric phosphor screen and a position sensitive detector. With appropriate voltages applied to the grids, the energy of the emitted electrons can be determined.

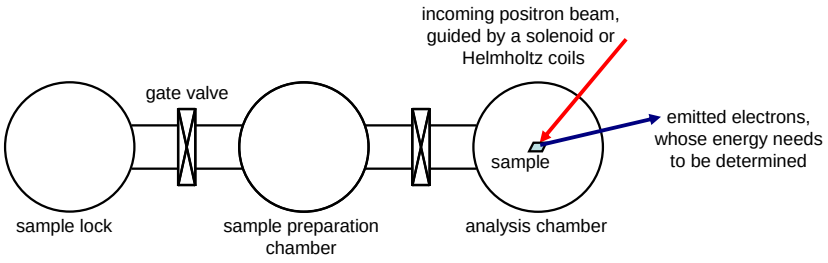

Figure 4.1: Sketch of the general setup of a PAES spectrometer, consisting of a sample lock, a sample preparation chamber and the analysis chamber.

The whole system must be shielded with µ-metal in order to shield disturbing magnetic fields. This setup has the advantage of a large solid angle, but on the other hand the signal to noise ratio and the energy resolution are poor. A further advantage of such a setup is the possibility to determine also the structure of the surface, which is the principal aim in LEED. None of the following other spectrometer types features such an opportunity.
The feasibility of PAES has been shown with this setup and in the following more and more elaborated setups were developed.

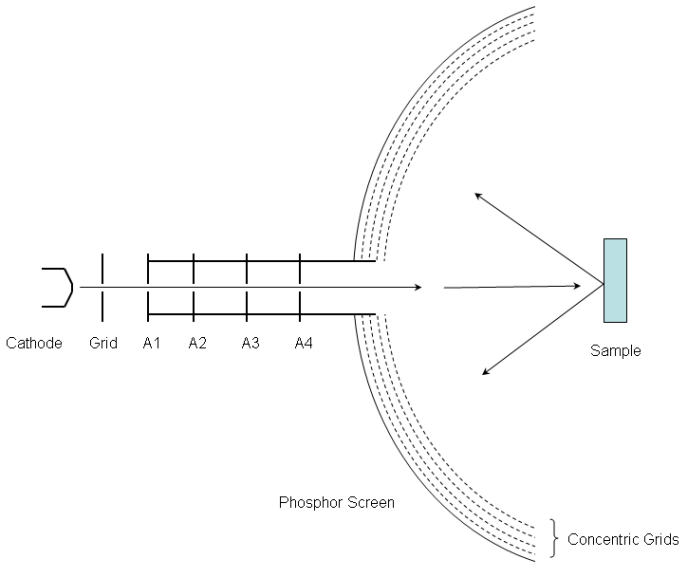

Figure 4.2: Sketch of a simplified conventional LEED setup. In the case of PAES, a positron beam instead of the shown cathode must be provided [Li06].

4.1.2 Cylindrical mirror analyzer

The **C**ylindrical **M**irror **A**nalyzer (CMA) uses two concentric cylinders, where the inner cylinder is set on ground potential while the outer cylinder is set on negative voltage and is scanned for the detection of electrons with different energies, see Figure 4.3. The CMA detects electrons that emerge from the surface of the sample within an angular range of $42.3° \pm 6°$. The detection is typically realized with a channeltron or a **M**icro **C**hannel **P**late (MCP). The electron gun or rather the positron source must be mounted within the CMA. The restricted space sets limits to the spatial requirements of the positron lenses. Also in the case of a CMA, the chamber is shielded with µ-metal. The energy resolution of a CMA can be approximated with the formula [Se67]:

$$\frac{\Delta E}{E} = 0.18 \cdot \frac{W_r}{R_i} + 1.375 \cdot (\Delta\alpha)^3 \quad , \tag{4.1}$$

where R_i is the radius of the inner cylinder, W_r the width of the exit slit and $\Delta\alpha$ is the half acceptance angle, i.e. $\Delta\alpha = 6°$. Exemplary values of $W_r = 5\,\text{mm}$ and $R_i = 25\,\text{mm}$ yield a resolution of $\frac{\Delta E}{E} \approx 4\%$.
The transmission, defined as the accepted solid angle divided by 2π, is calculated as follows:

$$T = 2 \cdot \sin(\alpha) \cdot \Delta\alpha \quad . \tag{4.2}$$

With $\alpha = 42.3°$ and $\Delta\alpha = 6°$ a transmission of $T = 0.141$ is achieved.

For a better energy resolution, a double CMA (two CMAs consecutively) can be used. Such a CMA is used at the university of Texas, Arlington. There, first highly resolved PAES-spectra were obtained [YZJ+97].

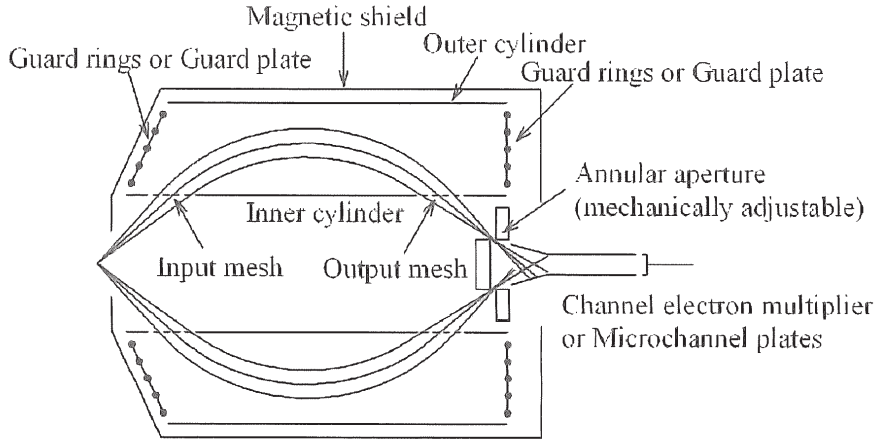

Figure 4.3: Setup of a typical CMA with an annular aperture to vary the energy resolution.

4.1.3 Time of flight method

The determination of the energy of electrons using their **T**ime **O**f **F**light (TOF) from the specimen to the detector is an alternative energy detection method in PAES [LMK+89,

LH07, SOM+96]. This is mainly attributed to the high efficiency of the principle. A TOF-spectrometer consists of a flight tube (approximately 1 m long) and a trochoidal filter, which separates the incoming positron beam from the emitted electron beam, see Figure 4.4. A trochoidal filter is an $\vec{E} \times \vec{B}$ filter, where the magnetic field is parallel and the electric field perpendicular to the beam direction. In comparison to a the classical Wien filter where $\vec{E}$ and $\vec{B}$ are perpendicular to one another as well as perpendicular to the beam.

Within the flight tube the incoming positrons and the emerging electrons are guided by a longitudinal magnetic field produced by Helmholtz coils. Right behind the sample the positron beam is focused by a strong permanent magnet onto the sample. The emitted electrons are gathered within a solid angle of almost 2π and fly back through flight tube. The emitted electrons are usually detected with a MCP. The annihilation quanta that are also produced at the sample serve as the start signal for the TOF-measurement, and the detected electrons at the MCP deliver the stop signal.

According to the time of flight Δt and the known flight distance L, the kinetic energy of the electrons can be easily calculated with $E = \frac{mL^2}{2\Delta t^2}$.

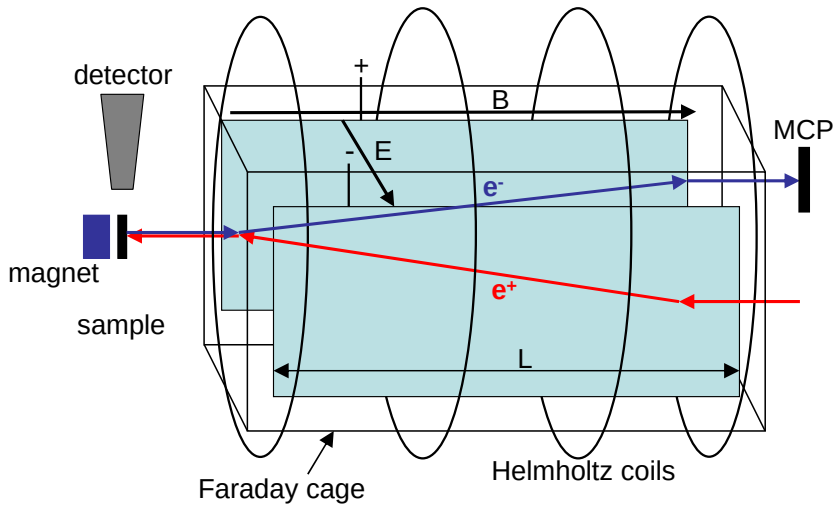

Figure 4.4: Realization of the TOF-PAES setup at NEPOMUC [Leg06]. The incoming and outgoing beam are separated by a trochoidal filter. The energy range is selected via the Faraday cage.

The energy resolution of a TOF-PAES apparatus depends on both the length of the flight tube and the energy range which is to be detected. The larger the energy range the worse the energy resolution gets. This restriction is in principal overcome with the new idea of installing a Faraday cage as it was done for the first time in Munich, see Figure 4.4. With the application of a defined potential, the emitted electrons are decelerated, which enlarges the flight time. With this the energy range, which is to be measured, can be varied and also high energy resolution at higher kinetic energies

becomes possible.
The ultimate resolution theoretically achievable with this setup amounts to $\frac{\Delta E}{E} = 2\%$. Without the Faraday cage, the typical energy resolution achievable is in the region of $\frac{\Delta E}{E} = 10\%$. More details can be found in [Leg06, LH07].

4.1.4 Concentric hemispherical analyzer

The **C**oncentric **H**emispherical **A**nalyzer (CHA) is an electrostatical electron energy analyzer. Thus, also in this case a magnetic shielding of the analysis chamber with µ-metal is inevitable. In Figure 4.5 a sketch of a CHA is shown.

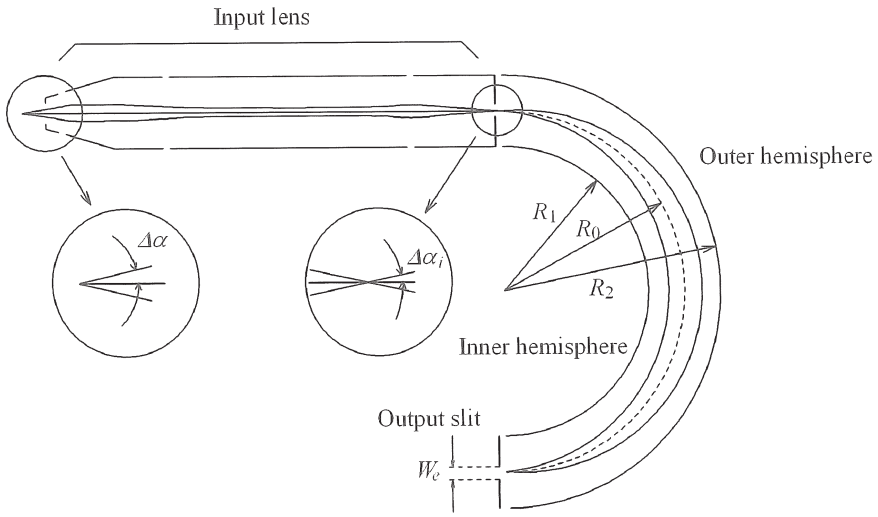

Figure 4.5: Sketch of a CHA [BG03]. In modern analyzers, there is analog to the output slit an entrance slit and an iris aperture in the input lens system in order to improve the energy resolution.

A CHA consists of an input lens system, two concentric hemispheres and an electron detector. It is utilized to measure the energy of charged particles, e.g. electrons or positrons. The hemispheres can be set on potentials and hence particles, entering the space between the hemispheres are deflected differently according to their kinetic energy and pass the hemispheres on orbital trajectories [Pur38].

In front of the hemispheres, there is a lens system which serves for several purposes. First, it images the sample plane onto the entrance plane of the CHA. Thus, the sample can be placed further away from the entrance of the hemispheres. Secondly, it defines the accepted area of the sample and the solid angle, and thirdly it accelerates/decelerates the particles to the pass energy of the hemispheres.

4.1.4.1 Energy resolution

The electric field between the two hemispheres with radii R_1 and R_2 is proportional to $1/r^2$ and focuses particles with the pass energy E_p onto the exit plane of the analyzer [BG03]. The energy resolution of a CHA can be calculated by the following equation [BS83, RT90]:

$$\frac{\Delta E}{E_p} = \frac{W_e}{2 \cdot R_0} + \frac{(\Delta\alpha_i)^2}{4} \quad , \tag{4.3}$$

where E_p is the pass energy, W_e the width of the exit slit and $R_0 = (R_1 + R_2)/2$ the mean radius between the two hemispheres. Particles with E_p, which are entering the hemispheres exactly in the middle of the two hemispheres, leave the hemispheres also in the exit plane exactly in the middle. $\Delta\alpha_i$ equals half the solid angle at the entrance plane, see Figure 4.5. The Lagrange-Helmholtz relation correlates $\Delta\alpha_i$ with the acceptance half-angle of the input lens, $\Delta\alpha$, as follows [RT90]:

$$\Delta\alpha_i = \frac{1}{M}\sqrt{R}\Delta\alpha \quad , \tag{4.4}$$

where R is the retarding ratio $R = E/E_p$ and M the magnification of the input lens system. Equation 4.3 for the energy resolution can hence be written as

$$\frac{\Delta E}{E} = \frac{1}{R} \cdot \left[\frac{W_e}{2 \cdot R_0} + \frac{R}{4} \cdot \left(\frac{\Delta\alpha}{M} \right)^2 \right] \quad . \tag{4.5}$$

The transmission of a CHA can be calculated with the formula:

$$T = 1 - \cos\Delta\alpha \quad . \tag{4.6}$$

With a typical value $\Delta\alpha = 12°$ the transmission amounts to $T = 0.02$. Thus, the transmission of a CHA is roughly a factor of 7 lower than the transmission of a CMA.

4.1.4.2 Modes of operation

A CHA analyzer can be operated in two different modes: the **F**ixed **A**nalyzer **T**ransmission (FAT) mode and the **F**ixed **R**etarding **R**atio (FRR) mode.

FAT mode In the FAT mode, the pass energy E_p is kept constant for all kinetic energies and the particles (in the case of AES electrons) are decelerated/accelerated in the lens system. The absolute energy resolution depends only slightly on the kinetic energy and the measured intensity is $N(E)$.

FRR mode The second analyzer mode is the **F**ixed **R**etarding **R**atio (FRR) mode, where the electrons are decelerated by a constant fraction of the initial kinetic energy $R = E/E_p$. Thus the pass energy is varied with their kinetic energy. Equation 4.5

reveals that in the FRR mode the absolute energy resolution is energy dependent, but the relative energy resolution is constant. Since the intensity in the FRR mode is proportional to the energy, the measured intensity is $E \cdot N(E)$. In Auger spectroscopy, traditionally the FRR mode is used [BG03].

Figure 4.6 shows the relative and the absolute energy resolution of a CHA. The graphs are calculated using Equation 4.5 with the following typical values: $W_e = 7\,\text{mm}$, $R_0 = 150\,\text{mm}$, $M = 1$ and $\Delta\alpha = 12°$.

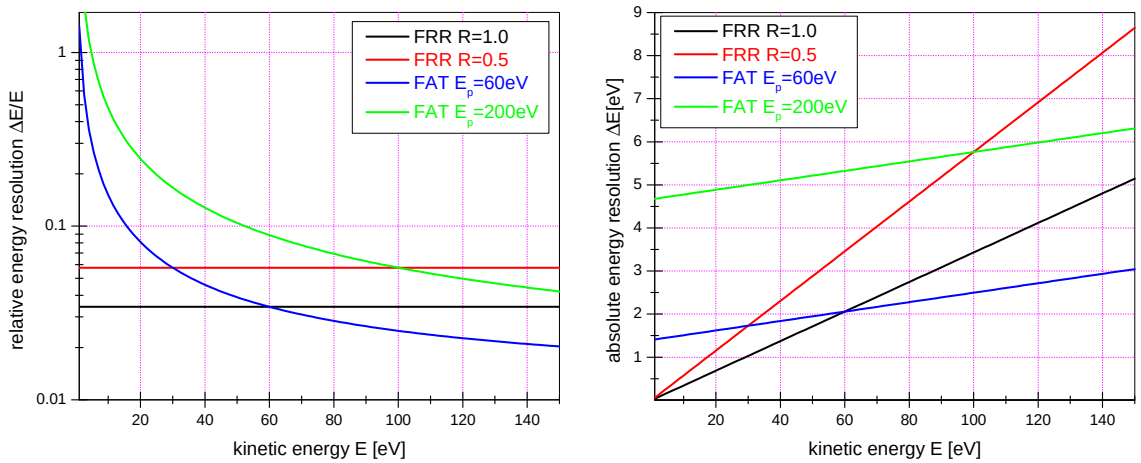

Figure 4.6: Left: relative energy resolution of a CHA as a function of the kinetic energy. Right: absolute energy resolution of a CHA as a function of the kinetic energy. In both cases the resolution is calculated for two different retarding ratios, $R = 1$ and $R = 0.5$, and two different pass energies, $E_p = 60\,\text{eV}$ and $E_p = 200\,\text{eV}$.

4.1.4.3 Electron detection

The electrons in the exit plane of the analyzer can be detected in one of the following ways. Either by a single channeltron as it is used only in old analyzers or by a stack of channeltrons in order to detect several kinetic energies simultaneously. Channeltrons have the advantage of very low dark count rates. The energy resolution of the analyzer is limited by the geometric dimensions of the channeltron stack, i.e. their number and size. It is also not possible to measure the angular spread of the electrons in the non dispersive direction, since no spatial information can be gained with channeltrons.

Another possibility nowadays is the electron detection with a MCP in combination with a CCD camera. A MCP has a smaller dynamic range compared to channeltrons and a higher dark count rate, but it has the advantage that it provides information in the dispersive as well as in the non dispersive direction. Thus, angularly resolved measurements become possible. The higher dark count rate enters only statistically and thus results in a linear background which can be subtracted. Moreover, the dark count rate can be minimized by cooling the CCD camera: the noise of the CCD camera is reduced typically by a factor of 2 if the temperature of the CCD is decreased by 8 K [The96].

If 2D local information and low noise is required the so-called delay line detector is a third alternative for electron detection. It consists of a (double) MCP assembly, which is not read out with a CCD camera, but with a set of wires (x and y direction) directly behind the MCP. Using the times informations from the x- and the y-wire it is possible to determine the exact place, where the electron emerged from the MCP. The delay line detector is faster and has a lower dark count rate than the CCD-readout, yet it is also more expensive.

For a more detailed description of concentric hemispherical analyzers the book *Surface analysis by Auger and X-ray photoelectron spectroscopy*, edited by D. Briggs and J. Grant [BG03] or *Low energy electron spectrometry* by Kenneth D. Sevier [Sev72] and the references therein are recommended.

4.2 Setup at NEPOMUC

In the following the details of each component of the PAES setup at NEPOMUC will be presented. The sample lock and the sample preparation chamber have been changed only slightly during this thesis. Except for the electron gun, all components in the analysis chamber have been renewed or modified compared to the former setup as it is described in [May06].

4.2.1 Vacuum chambers and installed instruments

The PAES-setup, realized at NEPOMUC is shown in Figure 4.7. It consists in principle of three chambers, each separated by a gate valve one from another:

- First, there is a sample lock to change the samples without breaking the vacuum of the other two chambers.
- It is connected to the sample preparation chamber, where the samples can be cleaned with Ar^+-ions and coated by means of either a metal foil boat (resistive heating) or by an electron beam evaporator. The thickness of the coating is controlled by a piezo thickness monitor. This setup enables a thin film deposition of two different materials with thicknesses from the fraction of an atomic layer up to several 100 nm.
- In the µ-metal shielded analysis chamber there are an electron gun for conventional EAES, a mass spectrometer for residual gas analysis and a MCP-CCD beam monitor for the positioning of the positron beam and the electron beam, respectively. Furthermore, a NaI(Tl)-detector for the observation of the 511 keV annihilation radiation, the positron lens system and the concentric hemispherical electron energy analyzer are installed there. As the positrons have an energy of only 20 eV , it is essential that there is no magnetic material used in the analysis chamber. Every slightly magnetic screw would distort the incoming positron

beam as well as low energy electrons. In the following the instruments installed in the analysis chamber are described.

4.2.1.1 Electron gun

The electron gun is tunable in its emission energy from 10 eV up to 5 keV. Thus, electrons are usable as testing particles, e.g. for the test of the MCP-CCD setup at low energies, and for conventional EAES, which requires electron energies in the keV range. For EAES the energy of the electrons was usually set to 2 keV and the emission current amounted to 4.4 µA.

4.2.1.2 Mass spectrometer

The mass spectrometer is used for leak testing and for residual gas analysis. It revealed that the most significant contribution were from H_2, H_2O and N_2. The contribution of H_2O was reduced considerably after the baking of the chamber for 48 h at 150°C.

4.2.1.3 NaI(Tl)-detector

The NaI(Tl)-detector is used to optimize the e^+-beam intensity at the sample site via maximizing the count rate of the detector. In order to exclude that the NaI(Tl) detector observes any other annihilation radiation than that from the specimen the NaI(Tl)-crystal is shielded by a lead and by a tungsten cylinder, see Figure 4.8. Such a misleading radiation might emerge from positrons, that annihilate at one of the lenses for the beam transport.
However, the detection of the count rate on its own was not sufficient to optimize the beam, since the detector integrates over a large area. Thus, there was no difference in the count rate, when the positron beam hit the sample right in the middle or off center. For a better beam focus and a maximal count rate a MCP was installed, see below.

During the PAES-measurements the count rate of the NaI-detector was recorded in order to see whether there was any change in the primary positron flux. If there was a malfunction of a high voltage supply for the lenses or a failure of the power supplies for the coils, the count rate monitoring was very useful to determine the exact time of the failure for a proper data evaluation.

4.2.1.4 Sample holder

The sample holder is simple in its shape and has dimensions of $25\times25\times9\,mm^3$, see Figure 4.9. It fits samples with the proportions of $25\times18\,mm^2$, which are hold in place by aluminum clamps. There are two clearances for the two forks of the manipulator in the analysis chamber and the transfer manipulator, respectively. The fork in the

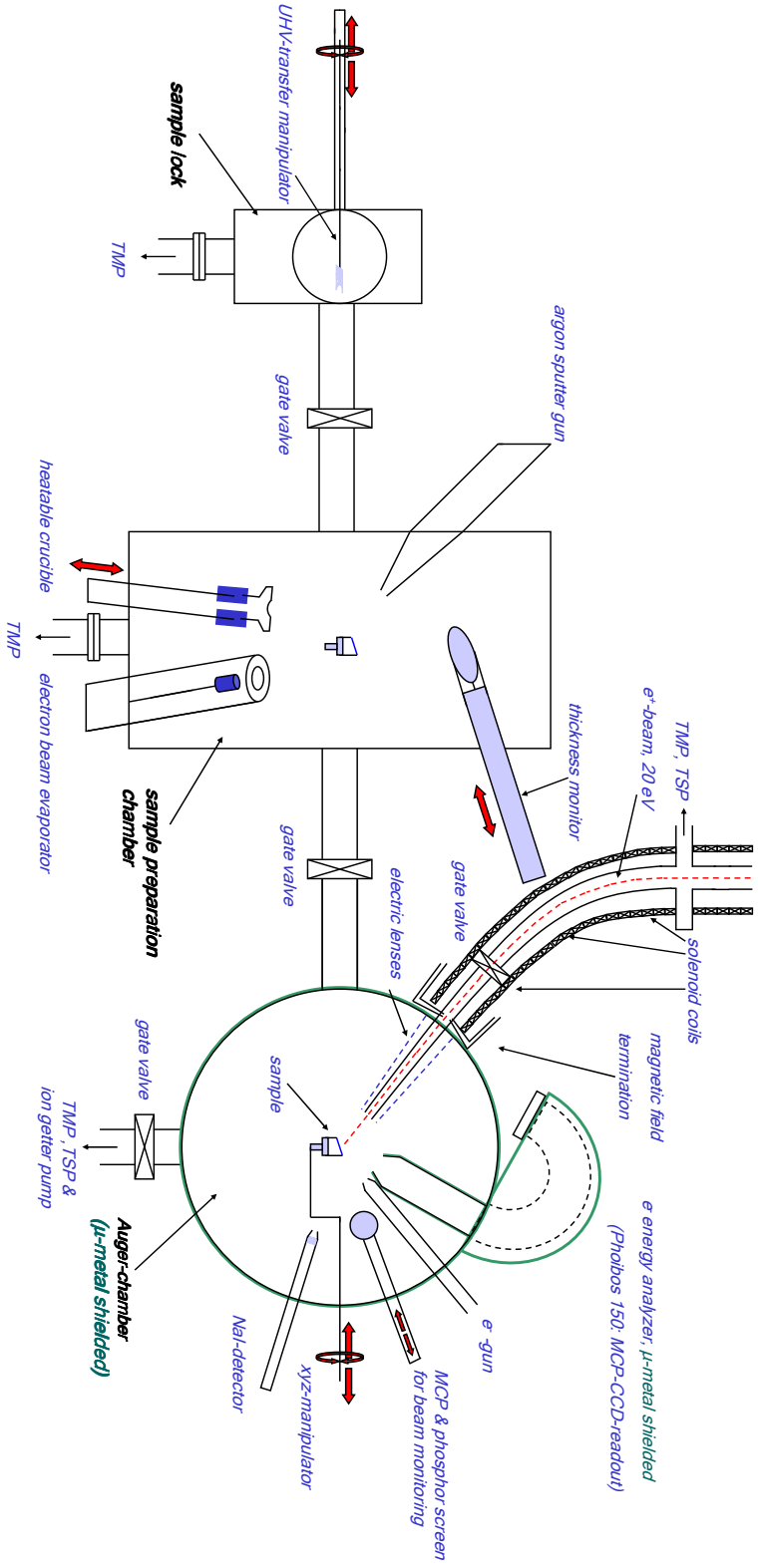

Figure 4.7: Sketch of the PAES setup at NEPOMUC. For details see text.

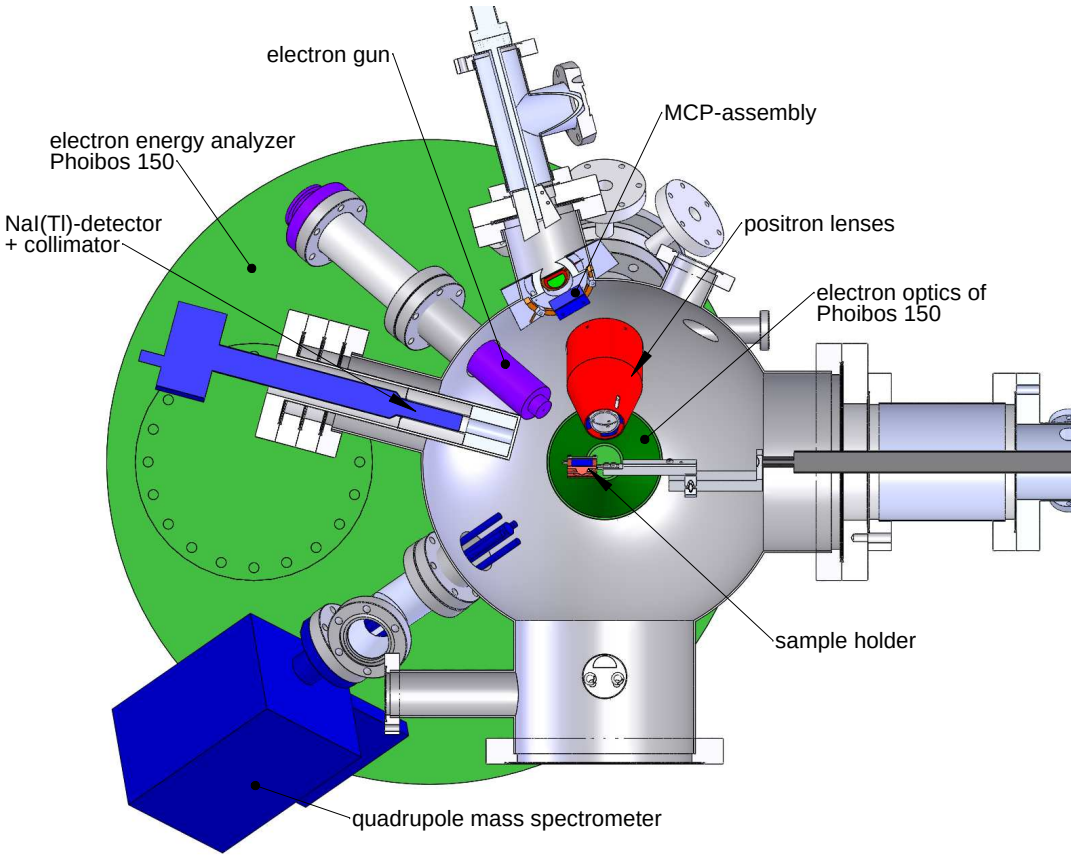

Figure 4.8: View into the Auger chamber.

analysis chamber is mounted on a xyz-manipulator (including rotation about the z-axis) for optimal sample positioning. In order to apply a well defined potential, the fork in the analysis chamber is electrically isolated and voltages of several 100 V can be applied. All PAES-measurements were performed at ground potential, but for the measurement of the positron work function a potential was applied.

4.2.1.5 MCP-CCD beam monitor

Lately, a movable MCP with a phosphor screen and a CCD for the readout was installed, see Figure 4.9 in order to determine the positron beam diameter at the sample site directly.
The output voltage (+1700 V) and especially the screen voltage (+3400 V) of the MCP-stack are set on high potentials. Thus, it was inevitable to shield the capton insulated wires, which are connected to the electrical inputs of the MCP, with nickel plated copper braid. The additional screening shown in Figure 4.9 was necessary to shield the connectors of the HV inputs.
In order to determine the energy distribution of the beam, there is also an electrically isolated grid in front of the MCP input. The idea was, to record the count rate of the NaI(Tl) detector, while the repulsive potential of the grid was being varied. However,

it was difficult to obtain an absolute value of the beam energy distribution, since the NaI(Tl) detector showed always the same count rate, independently from the bias of the grid. This was due to the fact that the positrons always annihilated within the solid angle seen by the NaI(Tl) detector. Thus, it cannot be distinguished whether the positrons annihilate at the MCP input or somewhere nearby. To get at least a qualitative understanding of the beam energy distribution, three pictures with three different grid potentials are shown in Figure 4.10. It is planned to install new electronics in order to read out the produced electrons directly via a capacitor. This will enable the quantitative analysis of the focused beam.

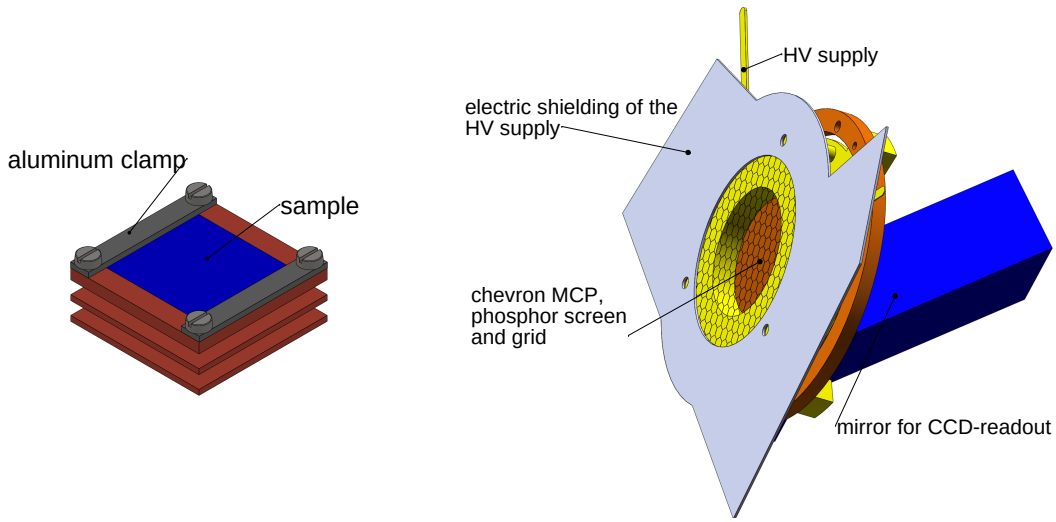

Figure 4.9: Left: sketch of the sample holder. Right: detailed view of the MCP-assembly in the Auger chamber. The shielding, made of copper, was necessary to avoid a distortion of the beam due to the HV supplies of the MCP.

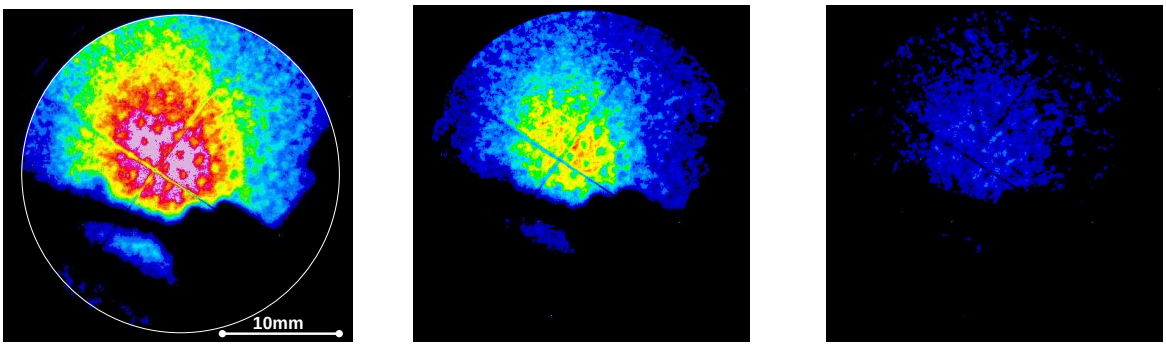

(a) $U_{\mathrm{Grid}} = 0\,\mathrm{V}$ (b) $U_{\mathrm{Grid}} = 10\,\mathrm{V}$ (c) $U_{\mathrm{Grid}} = 15\,\mathrm{V}$

Figure 4.10: MCP images with different grid potentials for a qualitative analysis of the beam energy distribution and for the determination of the beam diameter at the sample site.

4.2.2 Vacuum system

Regarding the fact that PAES is a surface sensitive analysis method, the vacuum system of the spectrometer is rather important. Assuming a sticking coefficient of 1 and a pressure of 10^{-6} mbar a sample is covered with one monolayer (ML) of contaminants within only one second. Hence, it is clear that for measurement times of several hours the pressure in the analysis chamber should at least be as low as 10^{-9} mbar to obtain reliable results. Initially it was a challenge to achieve a pressure below $3 \cdot 10^{-8}$ mbar [HMS07, May06], but due to several improvements it is now possible to record PAES-spectra at a pressure of $3 \cdot 10^{-9}$ mbar. This is reached with a turbo molecular pump (TMP) and a titanium sublimation pump, one of each mounted in the last part of the beam line as well as in the analysis chamber.
If the analysis chamber had to be opened, it was subsequently baked for 48 h at 150°C in order to reduce the H_2O fraction in the residual gas. With closed gate valves, a pressure of $< 1.5 \cdot 10^{-10}$ mbar is reachable in the analysis chamber, but the beam line with a base pressure of $8 \cdot 10^{-8}$ mbar limits the ultimate pressure to $3 \cdot 10^{-9}$ mbar. The use of the also available ion getter pump (IGP) is not desirable, since it produces a high electron background which affects the measurements. An improvement of the vacuum by one order of magnitude compared to the previous PAES-setup at NEPOMUC [May06] was achieved.

4.2.3 Beam guidance

4.2.3.1 General setup of the lens system

The positron beam, arriving from the remoderator, is guided adiabatically in a solenoidal transport field of 8 mT. The positron beam is released non adiabatically from the magnetic field and focused electrostatically onto the sample. Initially, the non-adiabatic release was realized with a „spider“-assembly [SAKH99]. The spider is made from µ-metal in order to terminate all magnetic fields at the chamber entrance. It showed however that despite its high geometric transmission, too many positrons annihilated at the spider veins, see Figure 4.11. This was due to the fact, that the spider was actually constructed for a lab beam with a diameter of less than 2 mm. The NEPOMUC beam at the spider, where the magnetic guiding field ends, has a diameter of 5 mm. Due to the partial annihilation of the positron beam at the spider, electrons were produced via Compton scattering and the photoelectric effect [MSH07]. The necessity to prevent those electrons to reach the sample led to unwanted limitations in the settings of the lens potentials and hence the beam was not focused properly.

In order to avoid these restrictions a new magnetic field termination was built, also made from µ-metal, but simpler in its shape compared to the spider. The new magnetic field termination has a similar silhouette as the spider, but instead of the tiny veins there is simply a hole of 16 mm diameter, see Figure 4.11. Simulations with Comsol multiphysics did not show major changes in the decay of the magnetic field at the entrance of the chamber compared to the spider geometry. Thus, the non-adiabatic beam extraction

is still ensured. The change of the geometry did not only reduce the annihilation at the magnetic field termination, but also acts as an aperture that enables differential pumping between the analysis chamber and the beam line.

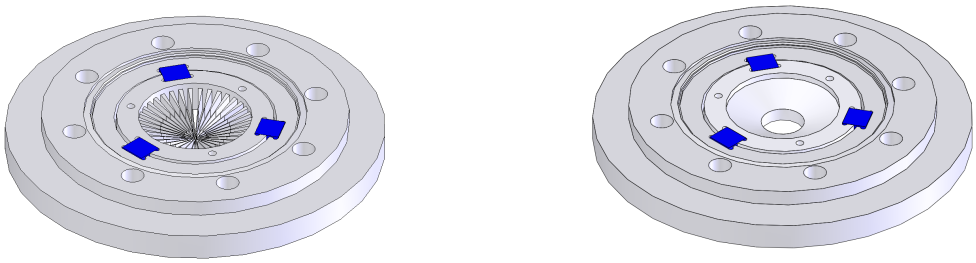

Figure 4.11: CAD drawing of the old (left) and new (right) magnetic field termination.

The magnetic field termination is part of the positron lens system, which is shown in Figure 4.12. The lens system consists of 8 lenses, where the penultimate lens is divided into 4 segments. These 4 segments enable the fine positioning of the beam on the sample. In order to shield the electric field, a Faraday cage is installed around the lenses.

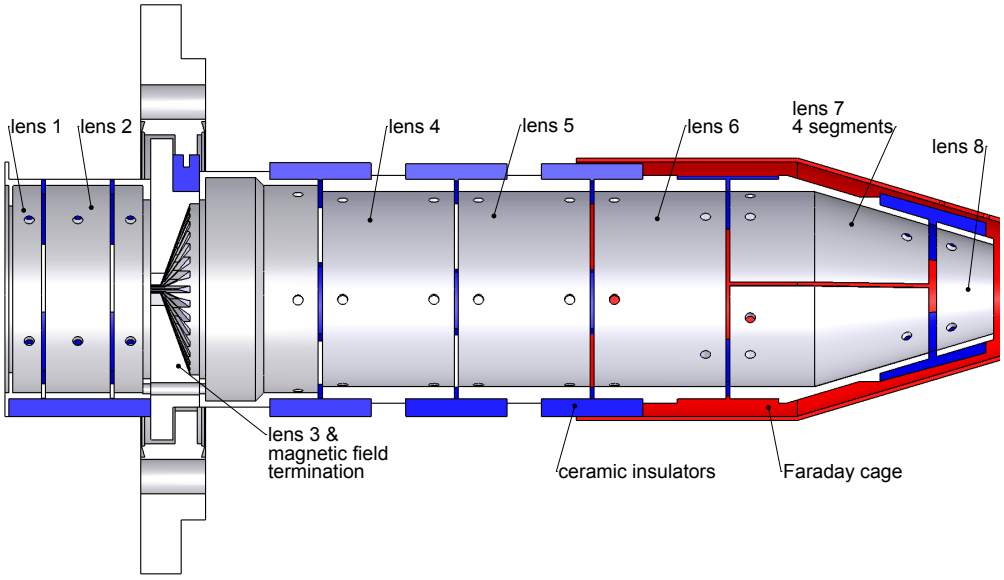

Figure 4.12: CAD drawing of the positron lens system.

4.2.3.2 Optimization of the beam focus

Beam properties and constraints In simulations with Simion the lens potentials were optimized, assuming a positron beam diameter of 5 mm in the magnetic transport field of 8 mT and a beam energy of 20 eV with FWTM= 5 eV [Pio09]. This is equivalent

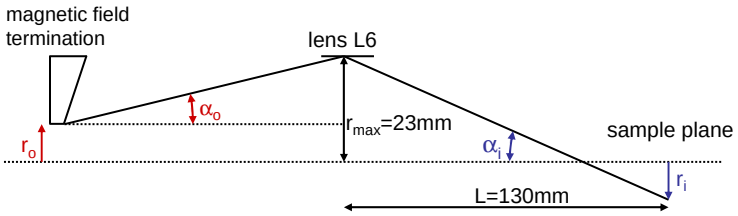

Figure 4.13: Simple sketch for the estimation of the minimal theoretically possible beam focus.

to a mean „longitudinal“ beam energy of $E_{\parallel} = 17.5\,\text{eV}$ and a „transversal“ beam energy of $E_{\perp} = 2.5\,\text{eV}$. Without magnetic field this corresponds to a divergence of $\pm 20°$. The deterioration of the beam quality results from field inhomogeneities and the many bendings on the way of the positrons from the remoderator to the experiment.

Since PAES needs positrons with an energy as low as possible, the sample must be set on ground potential and thus the focusing of the beam is not trivial. The last lens (L8) was always set on ground potential to minimize the stray fields in the sample region. All four segmented lenses (L7.1-L7.4) were in the simulation and in the experiment set on the same, low potential, since the positron beam did not have any axial displacement.

Theoretical limit The best beam focus, theoretically achievable with these restrictions can be calculated using Gaussian optics for rotationally symmetric lenses. For the sake of simplicity, only the magnetic field termination, lens L6 and the sample are considered for the calculation of the beam focus. Disregarding spherical and geometrical aberrations the beam diameter at the sample site can be approximated as follows [Pio09]:

$$r_i = \sqrt{\frac{\Delta E_{\perp}}{E_{\parallel}}} \cdot \frac{r_0}{\alpha_i} \quad . \tag{4.7}$$

r_i denotes the radius of the imaged beam, r_0 is the radius of the beam at the magnetic field termination and α_i gives the incident angle of the beam at the sample site, see Figure 4.13.

The beam spreads maximal over the whole inner diameter of the lens system, which results in an $\alpha_i = r_{max}/L \approx 0.18$. With the given values for $E_{\parallel} = 17.5\,\text{eV}$, $\Delta E_{\perp} = 2.5\,\text{eV}$ and $r_0 = 2.5\,\text{mm}$ a total beam radius of not less than $r_i = 6\,\text{mm}$ is achievable. It must be stressed that this estimation uses some kind of a worst case scenario, because only a minor part of the positrons have such a high transversal energy.

Simulations The same assumptions, concerning the total beam energy and the beam divergence, were used for the simulations carried out with Simion. Additionally to the positrons with a divergence of $\pm 20°$, intermediate starting angles of $\pm 10°$ and $\pm 5°$ were also simulated. Typical voltages, applied for the electrostatic beam guidance and the positron trajectories are shown in Figure 4.14. The simulation regards also electrons,

which might be produced at one of the positron lenses or the magnetic field termination. In the simulations those electrons start without energy right in front of the respective lens.

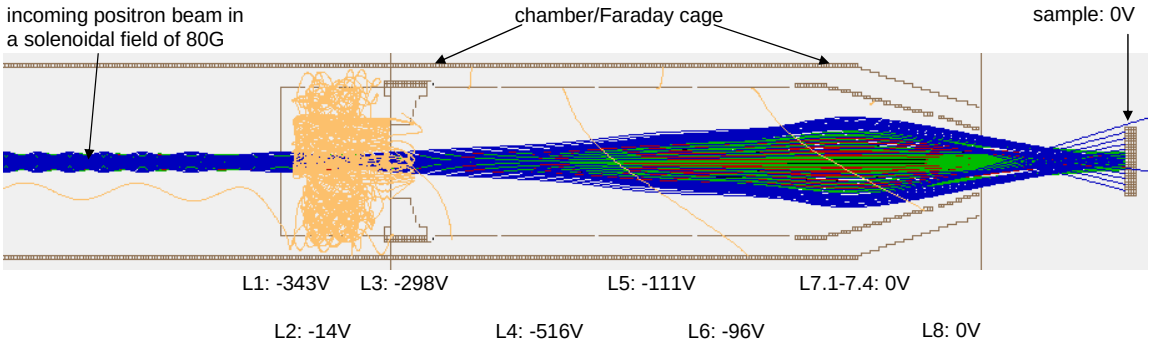

Figure 4.14: Simion simulation of the beam focusing onto the sample. The colors of the beam represent positrons with different beam starting angles: no divergence (black), ±5° (red), ±10° (green) and ±20° (blue). Furthermore, electrons (orange) are shown to ensure that no electrons, produced at the magnetic field termination or at one of the lenses, reach the sample with the applied voltages.

With the settings shown in the simulation, a beam diameter of less than 6 mm is achievable for the major part of the positrons. If also positrons with the highest transversal energy are taken into account, the beam focus increases to roughly 18 mm. The applied voltages also prevent electrons to reach the sample.
For every new beam time, the positron beam arrived in a slightly different way and the voltages had to be adjusted. Though the changes were only small.

Measured beam diameter The comparison of the simulation with the actually measured beam shows a good agreement. A picture of the positron beam is given in Figure 4.10. There, the total beam diameter amounts to ≈ 14 mm, the center beam with the major part of the beam has a diameter of ≈ 6 mm.

4.2.3.3 Artificial peaks

Not only electrons, which were produced at the magnetic field termination were a challenge. Since the beam spreads rather widely within the positron lenses it could occur, that a fraction of the positrons annihilated at one of the lenses and produced electrons, which were guided onto the sample. This resulted in a sharp peak in the electron energy spectrum, see Figure 4.15, which was avoided with appropriate lens potentials.

When this artificial peak occurred first, it was not clear which effect was responsible for it. At the beginning it was accidentally at an energy, where an Auger peak was expected. This was confirmed, when the peak position did not change in dependency

of the applied analyzer lens mode. The application of voltage at the sample did not shift the peak. Thus, it was clear that the electrons were already produced before they reached the sample. Finally, the variation of the positron lens potentials revealed the true nature of this peak. It was attributed to low energy electrons, emitted from a lens, which then reached the sample. The elastically backscattered e^- appear as a distinct peak in the e^--spectrum.

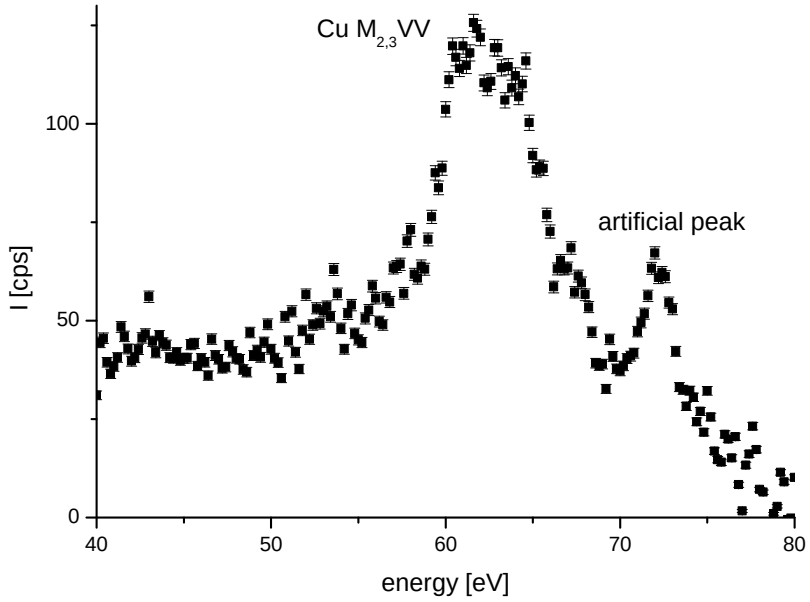

Figure 4.15: Electron energy spectrum, obtained with positrons. The peak at 71 eV is an artifact due to positrons annihilating at lens 6 which was set to 72 V. The produced electrons reach the sample and some of the elastically scattered electrons are detected in the analyzer.

It can be summarized that the focusing of the positrons is not always straightforward and needs a certain experience in order to produce a well focused beam at the sample site with high positron intensity and no electrons.

4.2.4 Concentric hemispherical analyzers at NEPOMUC

Together with the positron lens system, the electron energy analyzer is the most important part of the PAES spectrometer for fast and highly resolved PAES measurements. At NEPOMUC, a CHA is used, whose general concept was already explained in Subsection 4.1.4. Two different analyzers (CLAM2 and PHOIBOS 150) were in operation during this PhD-thesis, and their special features will be described in the following.

4.2.4.1 CLAM2

The CLAM2 was manufactured in the 1990's and was at that time state of the art with respect to hardware (electron detection, lens system etc.) as well as with respect to data

acquisition. There were only two lens modes available (mapping 1:1 and magnifying 3:1) and the retarding ratios and pass energies were selectable only in discrete steps and within a small range.

The CLAM2 analyzer uses sectional hemispheres with a mean radius of 100 mm and with a section angle of 150°. The electrons are detected with a single channeltron. There are no entrance slits and four exit slits (0.5, 1, 2, 4 mm). The electron lenses accept electrons, that emerge from the sample within ±3°. This results in a solid angle of

$$\frac{\Omega}{4\pi} = \int_0^{2\pi} \mathrm{d}\varphi \int_0^{3^\circ} \sin\gamma \,\mathrm{d}\gamma \approx 0.07\% \quad . \tag{4.8}$$

Due to the small solid angle and the electron detection with only one channeltron, the FAT mode with 200 eV pass energy was usually used for PAES. Only in this mode the transmission was high enough for measurements within reasonable time [May06]. Those settings resulted in a typical energy resolution with PAES as high as 6 eV.

Due to these restrictions, i.e. low energy resolution and the small solid angle, and the resulting long measurement time of 12 h it was decided to purchase a new electron energy analyzer, the PHOIBOS 150. A reduction of the measurement time by at least one order of magnitude was expected.

4.2.4.2 PHOIBOS 150

In autumn 2007 the new electron energy analyzer, PHOIBOS 150, has been installed. It is different to the CLAM2 in several aspects.

First, it offers a new state of the art electron lens design which enlarges the acceptance area of the analyzer strongly. Depending on the applied lens mode (3 magnifying modes, 4 angular resolving modes and 3 transmission optimized modes) it offers an acceptance angle of up to ±13°, resulting in a solid angle of 1.3%. This leads to a higher transmission compared to the CLAM2 and thus reduced measurement times.

Secondly, the electrons are detected with a MCP (diameter 40 mm) and hence several energies can be acquired simultaneously. The number of the latter depends on the discretization of the CCD-readout. It can be adjusted between 10 and 100 channels, resulting in virtual slit widths of $0.4 - 4$ mm. The more channels, the larger the data amount and also the dead time. It turned out that dividing the MCP into 25 virtual channels for the simultaneous acquisition of 25 energies is a good compromise between dead time and energy resolution. The noise of the CCD camera is minimized by cooling the camera to a temperature of −13°C.

Thirdly, the whole analyzer is truly bipolar. Thus it is also possible to analyze positrons in their energy. This is useful e.g. for the measurement of positron work functions, see Section 5.9.

Fourthly, the PHOIBOS 150 offers more slit combinations (8 entrance and 2 exit slits) compared to the CLAM2 and the mean radius of the electrons passing the hemispheres increased from 100 mm to 150 mm. Together with the higher transmission of the lenses,

measurements with higher energy resolution are hence enabled. Whereas it was impossible with the CLAM2 to record spectra in the FRR mode due to its poor transmission, this mode can be applied now. For the first time, this provides the opportunity for direct comparison between EAES and PAES, since in EAES the FRR mode is the typical measurement mode.

The true 180° section with its ideally self focusing properties [ZB02] reduces the spread of the image of the sample spot and enhances the energy resolution furthermore. The energy resolution is calculated with the following formula [SPE], which is only slightly modified compared to Equation 4.3, because of the use of entrance and exit slits:

$$\frac{\Delta E}{E_p} = \frac{S}{2 \cdot R_0} + \frac{\Delta\alpha^2}{4} \quad . \tag{4.9}$$

S is given by $S = (S_1 + S_2)/2$, where S_1 and S_2 are the entrance and the exit slit widths, respectively. R_0 denotes the mean radius of the analyzer, i.e. $R_0 = 150\,\mathrm{mm}$ and $\Delta\alpha$ gives the divergence of the electron beam when it enters the analyzer.
Since $\Delta\alpha$ changes with the kinetic energy and the applied lens mode, it must be calculated for each setting separately. Yet, the second term on the right hand side of Equation 4.9 is maximally as big as the first term on the right hand side of Equation 4.9 [Mäh09, BS83]. This estimation was tested in a measurement of the energy resolution of the analyzer for pass energies, which are relevant for the PAES measurements. For this purpose, the electron beam was tuned to energies, where Auger peaks are observed. Then, the FWHM of the elastic peak was measured with different retarding ratios, i.e. energy resolutions. The FWHM, ΔE is plotted in Figure 4.16 as a function of the pass energy E_p.

Besides the measured values, also theoretical values are given in Figure 4.16. These were calculated according to:

$$\Delta E = E_p \cdot \frac{S_1 + S_2}{2 \cdot R_0} \quad . \tag{4.10}$$

Here, the second summand in Equation 4.9 was assumed to be as large as the first summand. This results in the worst theoretically possible energy resolution.

The measured resolution in Figure 4.16 is in most cases better than the theoretical values. For that reason, a linear fit of the form

$$\Delta E(E_p) = a + m \cdot E_p \tag{4.11}$$

is applied to the measured data points, which is plotted as a green solid line in Figure 4.16. The results are:

$$a = 0.065 \pm 0.035 \qquad \text{and} \qquad m = 0.024 \pm 0.001 \quad . \tag{4.12}$$

With the entrance slit width of $S_1 = 7\,\mathrm{mm}$ and the exit slit width of $S_2 = 1.4\,\mathrm{mm}$ the divergence $\Delta\alpha$ is calculated to $\Delta\alpha \approx 11.6°$. Thus, the experimentally determined energy resolution, which is used in the following is calculated with the formula

$$\frac{\Delta E}{E} = \frac{1}{R} \cdot 0.024 \quad , \tag{4.13}$$

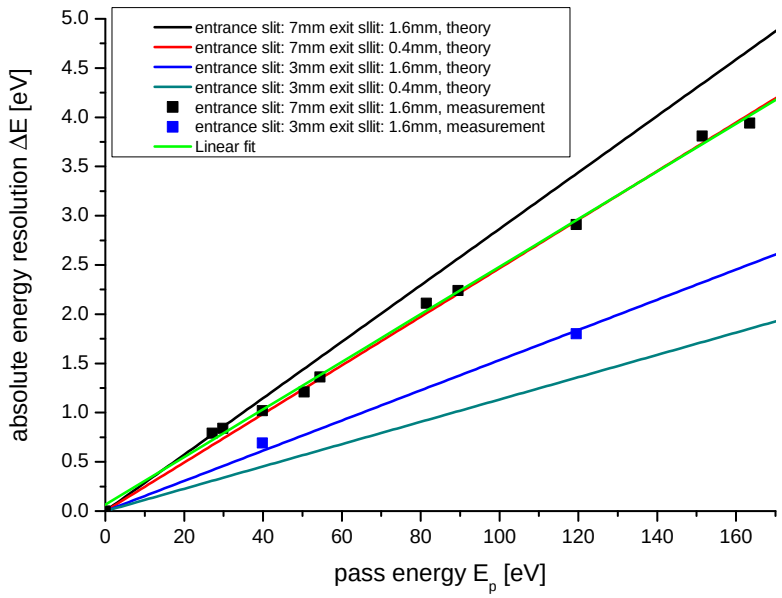

Figure 4.16: Theoretical (continuous lines) and measured (discrete data points) energy resolution at relevant pass energies. The green line is a linear fit of the black data points.

in the case of $S_1 = 7\,\text{mm}$ and $S_2 = 1.4\,\text{mm}$. $R = E/E_p$ denotes the retarding ratio. This value is roughly 17% below the conservative limit, which is used for other slit settings:

$$\frac{\Delta E}{E} < \frac{S}{R \cdot R_0} \quad . \tag{4.14}$$

4.2.4.3 Comparison of CLAM2 and PHOIBOS 150

Summing up, the new electron energy analyzer was expected to reduce the measurement time by at least one order of magnitude and to provide a better energy resolution at the same time, see Chapter 5. Table 4.1 summarizes the most important features of the utilized analyzers are compared. It is stressed that the values for $\Delta E/E$ in Table 4.1 are typical for PAES. Both analyzers can be operated at higher energy resolutions. Those numbers are given in the column ultimate ΔE. Only with the given values it was possible to obtain a PAES spectrum within reasonable time.

	typical $\frac{\Delta E}{E}$	ultimate ΔE	electron detection	solid angle
CLAM2	$\approx 10\%$	100 meV	1 channeltron	0.07%
PHOIBOS 150	$< 5\%$	2.9 meV	MCP/CCD assembly	1.3%

Table 4.1: Comparison of the old electron energy analyzer (CLAM2) and the currently installed analyzer (PHOIBOS 150).

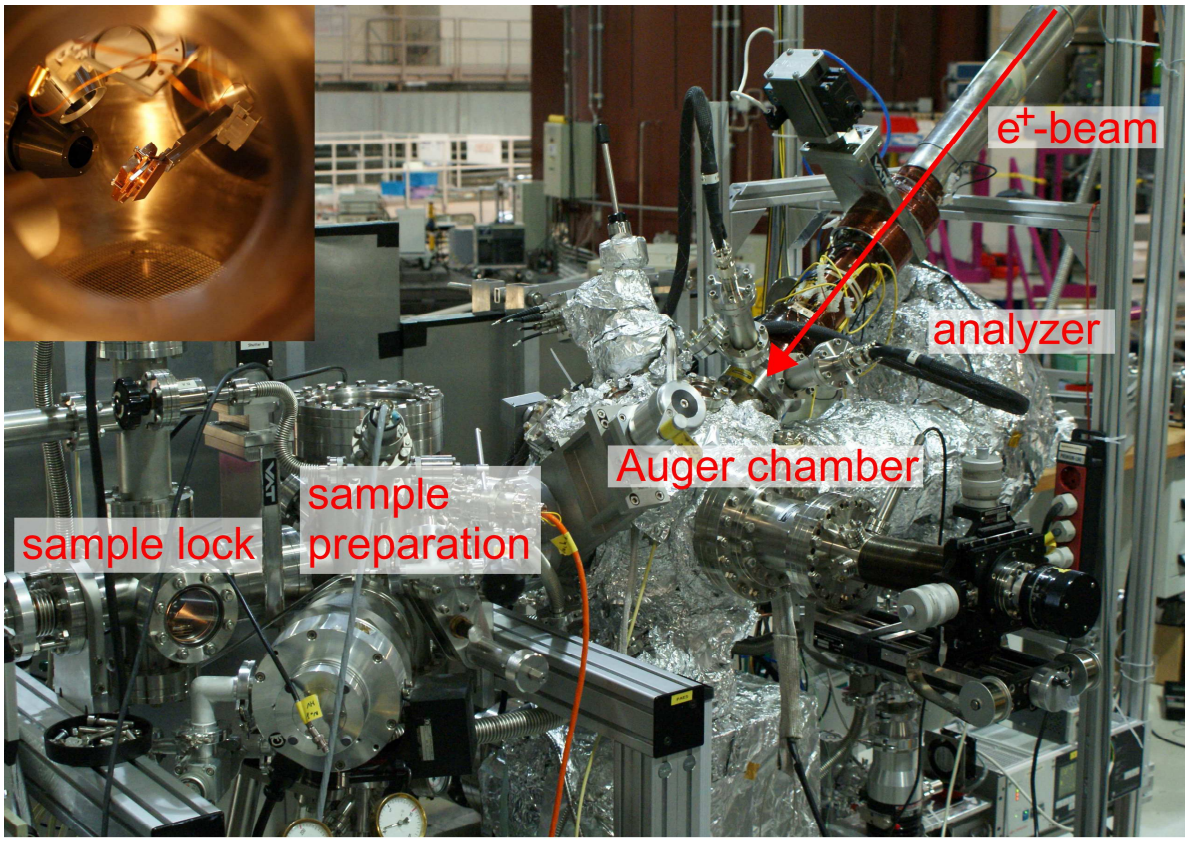

Figure 4.17: Picture of the PAES setup at NEPOMUC.

Chapter 5

Measurements and results

This chapter starts with a short review of the measurements which have been performed at the PEAS spectrometer before this thesis. Then, the sample preparation is described, followed by a presentation of the measurements carried out during this thesis. The associated results will be discussed in detail.

In the first part, the general improvement, concerning measurement time and spectrum quality, is revealed. Secondly, a PAES spectrum of Cu with the shortest measurement time reported so far will be presented. Then, a PAES-measurement of copper with unprecedented high energy resolution follows. After that, PAES spectra of high purity elements are presented. In order to demonstrate the surface sensitivity and elemental selectivity, samples covered in the sub-monolayer range are shown. At two of those coated samples the segregation of the topping layer could be observed.
Finally, a first measurement of the energy distribution of moderated positrons will be shown. With this type of measurement, it is in principle possible to determine the negative positron work functions of a material.

5.1 Status of PAES at NEPOMUC before this thesis

The current PAES spectrometer at NEPOMUC has already been modified twice. The first version was built up during the PhD-thesis of B. Straßer [Str02]. This spectrometer was operated with a ^{22}Na-source at a positron beam energy of 40 eV. It was demonstrated at the example of a polycrystalline Cu foil that the spectrometer was working stable. Yet, it took 20 days to obtain a single PAES spectrum, see Figure 5.1. The Auger electron intensity, detected at the electron energy analyzer was as low as $6 \cdot 10^{-2} e_A^+/s$. Thus, this setup could hardly be used for regular measurements, competitive with EAES due to the long measurement time.

In the next stage the spectrometer was connected to the NEPOMUC beamline, where also a sample lock and a sample preparation chamber were added to the main chamber. With the first of operation of NEPOMUC in 2004, it was already possible to perform PAES-measurements, see Figure 5.2 [HSSS06]. The measurement time was reduced

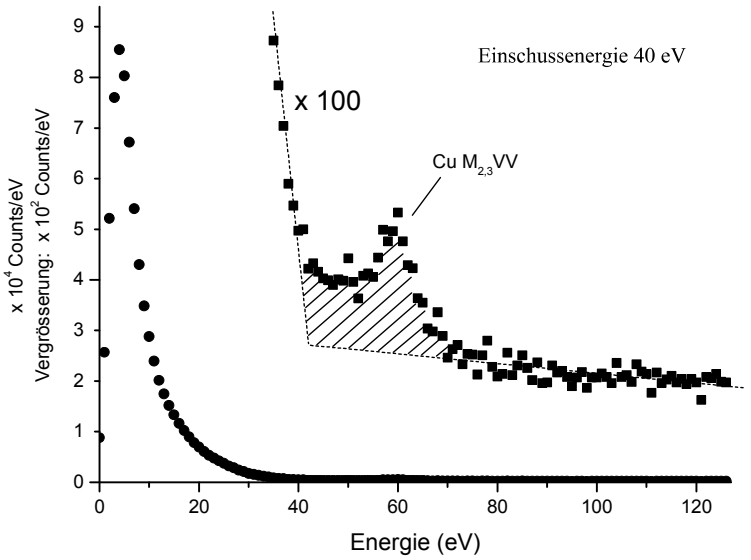

Figure 5.1: First PAES spectrum at the FRM-II, measured with ^{22}Na-based positron beam. The measurement time amounted to 20 days [Str02].

considerably due to the higher positron intensity and amounted to 12 h per spectrum. With this configuration, the spectrometer was used successfully in the diploma thesis of J. Mayer [May06]. Measurements of polycrystalline Cu and Si(100) coated with Cu were published, which demonstrated the high surface selectivity of PAES. Furthermore, the initially high secondary electron background was reduced by a factor of 3 and a Cu sample was measured within only 3 h and a SNR of 3:2 [MSH07, HMS07]. The pressure in the analysis chamber during the PAES measurements was $4.5 \cdot 10^{-8}$ mbar.

In the present thesis, it was aimed for improving the vacuum and reducing the measurement time further, at least by one order of magnitude. Both was achieved and even time dependent PAES-measurements and hence the observation of dynamic processes at the surface have become possible.

5.2 Sample preparation

In order to prepare a clean sample surface, the following procedure was carried out: First, the samples were cleaned ex situ using acetone and deionized water. Secondly, the specimen were annealed ex situ under vacuum conditions ($p < 10^{-6}$ mbar) at $T = 0.75\,T_m$, where T_m denotes the melting temperature of the respective material. This is far above the recrystallization temperature and hence the majority of defects and defect clusters is removed. Since the grain size is thus enhanced, the capture of positrons in grain boundaries is negligible.

After the transfer in the vacuum chambers, the specimen surface was cleaned with the Ar^+-sputter gun, using an Ar^+-energy of 1 keV and the cleanliness Ar 6.0. The sputter-

ing angle was set to $50 \pm 2°$ relative to the surface normal which showed experimentally to be the optimal angle. The ion beam current amounted to $I = 35\,\mu A$. In order to clean the entire sample with a surface area of typically $18 \times 20\,mm^2$ an Ar^+-beam diameter of 20 mm was chosen. The incident angle increased the effective beam diameter at the sample site to $d = \frac{r^2 \cdot \pi}{\sin 50°} \approx 410\,mm^2$.

The chosen parameters are sufficient for the cleaning of the sample surface, as the following estimation for the time to remove one ML shows:

$$\frac{\text{number of atoms/ML}mm^2}{\text{number of ions/s}\,mm^2} \approx \frac{10^{13}/mm^2}{\frac{35 \cdot 10^{-6} A}{1.6 \cdot 10^{-19} As \cdot 410\,mm^2}} \approx 19\,s \quad . \tag{5.1}$$

This estimation assumes a sputtering yield of 1, i.e. 1 ion removes 1 surface atom, see [RB07].

The sputtering time depended on the initial surface conditions and had a range from 10 min for almost clean samples that were stored in the vacuum chamber, and up to 2 h for samples that were used for the first time and had been stored at ambient pressure before. In the case of the coated samples (cf. Section 5.7) the sputtering time was set to 20 min in order to ensure a clean surface.

5.3 Improvements of the PAES spectrometer

In this section, the development of the PAES spectrometer is illustrated, using an exemplary PAES spectrum of polycrystalline copper, which was recorded at each development stage of the spectrometer.

The first PAES spectrum measured at NEPOMUC is plotted in black squares in Figure 5.2. The measurement time amounted to 12 h, the SNR to 3:2 and the positrons had a kinetic energy of 40 eV. The secondary electron background over the whole energy range was higher than expected.

It turned out that this background was due to electrons that were produced at the magnetic field termination (spider) as a consequence of the large beam diameter. These electrons were accelerated to an energy equivalent to the spider potential of $-1000\,V$ and a part of them reached the sample. Hence, the spectrum shows a mixture of PAES and EAES. Further background arose from (n, γ)-reactions in the experimental hall of the FRM II. With a better beam guidance and a lead shielding, the spectrum plotted in red squares in Figure 5.2 was obtained. The background is reduced considerably, which results in a SNR of 3:1, whereas the measurement time amounted still to 12 h. The energy of the positrons amounted to 47 eV. A detailed description of those measurements is given in [May06, HSSS06]. This was the status at the beginning of this thesis.

In a first step, the implementation of the remoderation stage provided the major improvement. With the help of the remoderator, the beam brightness was enhanced by a factor of 300. This means that on the one hand the beam intensity was reduced, but on

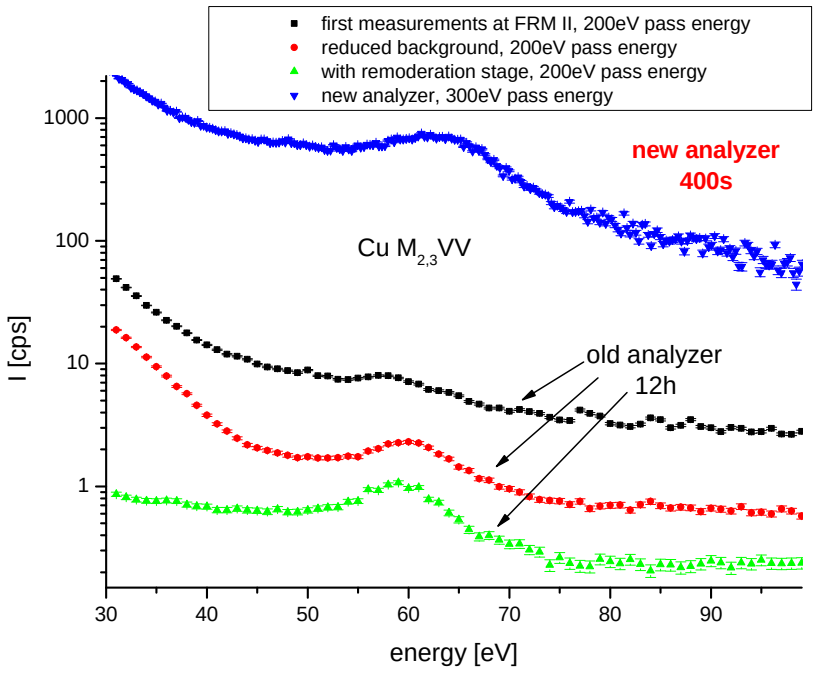

Figure 5.2: PAES spectra of polycrystalline Cu at the four development stages at NEPOMUC. For a better comparison, all measurements were recorded in the FAT mode. The spectrum quality increases with each step. Note the logarithmic intensity scale.

the other hand the resultant beam was smaller in its diameter and sharper in its energy distribution. Consequently, the positron beam was focused better onto the sample and hence relatively more electrons were emitted within the acceptance area of the analyzer (CLAM2). Thus, the absolute count rate of the analyzer was reduced, but the quality of the spectrum was improved to a SNR of 7:2 (green triangles in Figure 5.2) [MHS08]. All following measurements were performed with the remoderator.

In a second step the new electron energy analyzer PHOIBOS 150 was installed (see Section 4.2.4.2). The new setup allows now to measure a PAES overview spectrum within only 400 s with a further improved SNR of 17:2. The resulting spectrum is shown in blue triangles in Figure 5.2—note the logarithmic scale. This means that the new analyzer reduced not only the measurement time by two orders of magnitude, but also enhanced the SNR more than a factor of 2.

All measurements in Figure 5.2 were performed in the FAT mode, since there was no other possibility with the CLAM2. The new analyzer enables for the first time direct comparison of EAES and PAES with respect to the analyzer mode. Now, the FRR mode is also the standard analyzer mode for PAES and all following spectra are recorded in the FRR mode. If not stated otherwise, the used lens mode was the **W**ide **A**ngle **M**ode (WAM), because it provides with $\pm 13°$ the largest acceptance angle. Except for the high resolution measurement, where an entrance slit of 3 mm was used, the slit was set to 7 mm . The MCP was divided into 25 virtual channels for all measurements.

5.4 Short term PAES-measurement

The new analyzer with its high transmission offers entirely new possibilities. Figure 5.3 shows a PAES spectrum, recorded within only 420 s in the FRR mode and an energy resolution of $\frac{\Delta E}{E} < 5\%$. The SNR in this measurement amounts to 11:1. This is the shortest measurement time for a PAES spectrum with reasonable statistics reported so far, for comparable positron beam energy and energy resolution [SOM+96].

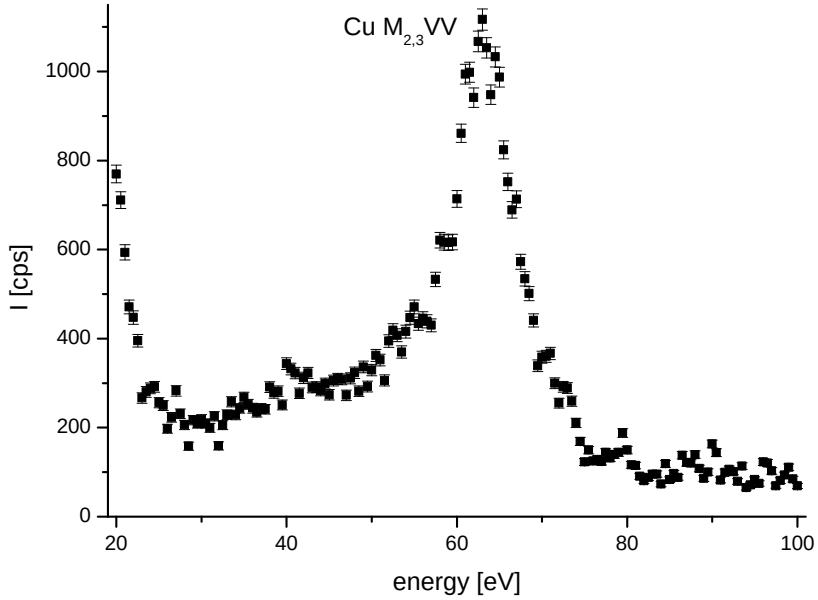

Figure 5.3: PAES spectrum of a polycrystalline copper foil, recorded within only 420 s.

Since the measurement time for an overview spectrum was reduced to that extent, it became possible to control the cleanliness of a sample after the sputtering process with PAES. Until then, this was usually done with conventional EAES due to the shorter measurement time. But since PAES is more surface sensitive and not more time consuming than EAES, from that time on the cleanliness was verified only with PAES. Furthermore, the short recording time enables the measurement of dynamic processes with PAES for the first time, see Section 5.8.

5.5 High resolution PAES of the Cu $M_{2,3}$VV-transition

Motivation for the measurement Due to the different ionization process of PAES compared to EAES, the line shape of Auger transitions should be well observable without background as long as the energy of the Auger electrons is higher than the energy of the impinging positrons. This is true for the Cu $M_{2,3}$VV-transition, which occurs at approximately 62 eV, when 20 eV positrons are used. At EAES, the impinging electrons

have high energies, generating a high secondary electron background and producing Auger electrons from several atomic layers. These scattered Auger electrons hence might affect the peak position and the line shape of the Auger transition as already explained in Chapter 3.

Several experiments with different specimens have been conducted by other groups in order to investigate, whether there is a difference in the kinetic energies or in the line shape between PAES and EAES [YZJ+97, YZJW95, OSMY97, MSH09]. In these publications the energy resolution amounted to $\frac{\Delta E}{E} = 2\%$ or worse and the double peak structure of Cu could not be resolved clearly.

Due to the different binding energies of the $3p_{1/2}$ level and the $3p_{3/2}$ level a relative difference of 2.2 eV in the peak positions is expected for evaporated copper [FKWF77, GDPO+09]. Hence, with an energy resolution of the present setup of $\frac{\Delta E}{E} < 1\%$ both peaks should be clearly resolvable.

Comparison of the PAES and EAES spectra In Figure 5.4 the electron energy spectra of the PAES and EAES measurement of Cu(111) are shown. Both spectra were recorded in the FRR mode with a relative energy resolution of $\frac{\Delta E}{E} < 1\%$. This is the best energy resolution for PAES, reported so far (cf. [YZJW95, YZJ+97]). The step width was set to 0.25 eV and the entire PAES spectrum was recorded within only 5.5 h.

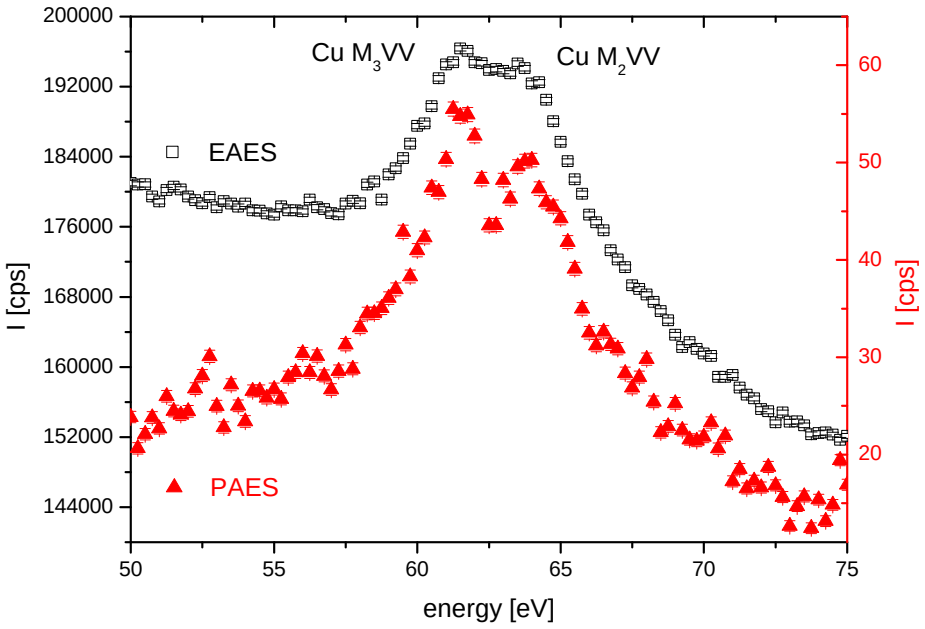

Figure 5.4: High resolution spectroscopy of the Cu $M_{2,3}VV$-transition with EAES (open squares) and PAES (full triangles). The energy resolution was set to $\frac{\Delta E}{E} < 1\%$. The double peak structure was clearly resolved with PAES. Note the different intensity scales for EAES (left) and PAES (right).

With EAES, the high secondary electron background leads to a SNR of 1:6. Furthermore, the two peaks, corresponding to the Cu M_3VV and the Cu M_2VV Auger transi-

tion can be seen and the energy difference reads 2.3(1) eV. But due to the large volume in the specimen, where Auger electrons are excited by the incoming electrons, the inelastically scattered electrons smear out the minimum between both peaks. Moreover, the secondary electron background makes it difficult to determine the line shape.

PAES in contrast, reveals the double peak structure clearly. The predominant emission of the Auger electrons from the topmost atomic layer leads to a better resolution of the double peak compared to EAES. The relative energy difference of the peaks amounts to 2.3(1) eV, similar to EAES. Due to the low positron implantation energy the signal drops to low count rates on both sides of the peak. Consequently a SNR of 5:2 is observed. Nevertheless, the peak structure still seems to be broad. This is not attributed to the energy resolution of the analyzer, but it is an intrinsic broadening. This leads to an effective broadening of the two primary peaks, see [BJHK96].

5.6 High purity materials

The difference in the surface sensitivity and elemental selectivity of PAES compared to EAES, can be seen most clearly with the examination of layered samples. The first step for the investigation of such systems is to record spectra of the clean reference samples. Several different materials with varying Auger peak energies and positron affinities were investigated: polycrystalline samples of Fe, Ni, Cu, Zn, Pd and Au. Due to annealing the grain sizes are sufficiently large. Thus, the positrons are not trapped at grain boundaries.

5.6.1 PAES spectra of Fe, Ni, Cu, Zn, Pd and Au

The PAES spectra for all these elements are shown in Figure 5.5. All Auger peaks in Figure 5.5 can be distinguished clearly. The SNR varies from 1:1 in the case of Zn to 10:1 in the case of Pd. The step width for all measurements was 0.5 eV, except for Au and Ni, where the step width was set to 0.25 eV. The energy resolution for Fe, Cu, Zn and Pd was better than 5%, for Ni and Au even better than 2.5%. The measurement time for each spectrum amounted to 80 min. This measurement time was chosen in order to ensure enough statistics for all measurements, also for the elements where lower count rates are expected. In all cases, the most significant Auger peak stems from electrons of the outermost main shell. Deeper electron levels might have also been excited, but only in the case of Pd a peak was observed. The Pd M_5NN-transition can be seen only very badly and is not taken into account for further evaluations.
The background, which is still observable at energies higher than the Auger peak is attributed to Compton and photo electrons produced by the annihilation radiation in the sample and scattered electrons from energetically higher Auger peaks.

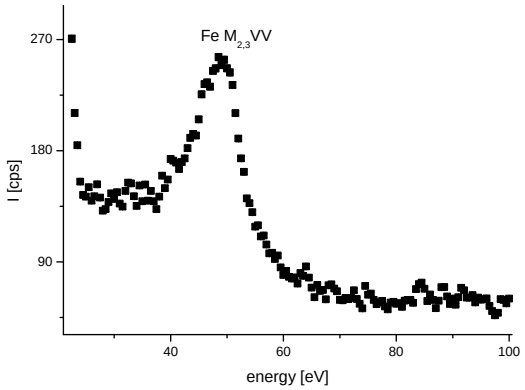

(a) Polycrystalline Fe, FRR 0.5.

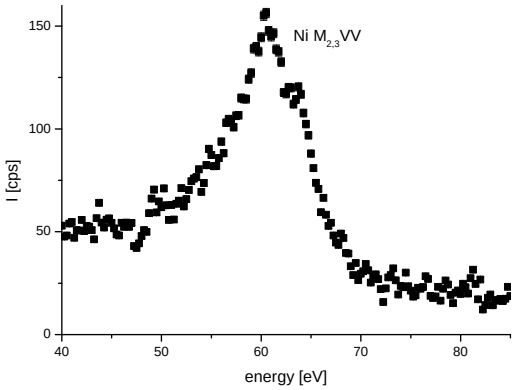

(b) Polycrystalline Ni, FRR 1.0.

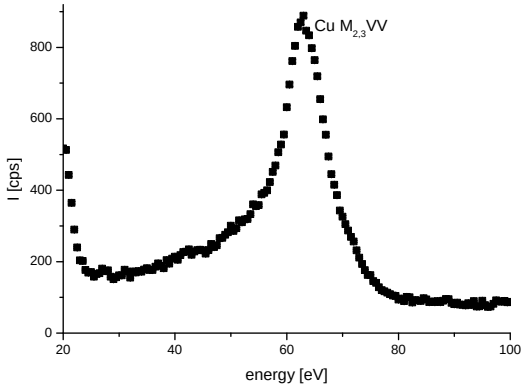

(c) Polycrystalline Cu, FRR 0.5.

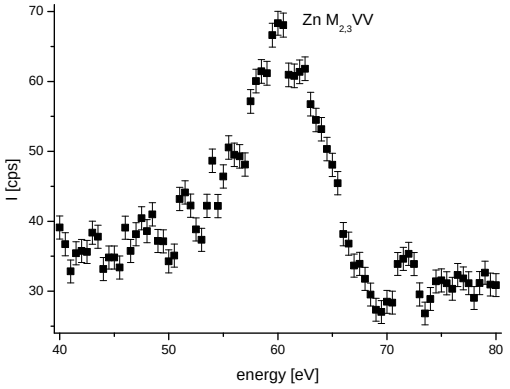

(d) Polycrystalline Zn, FRR 0.5.

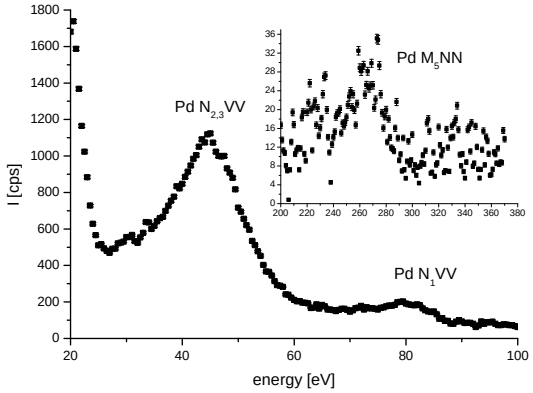

(e) Polycrystalline Pd, FRR 0.5. Inset with LAD lens mode, FRR 1.0

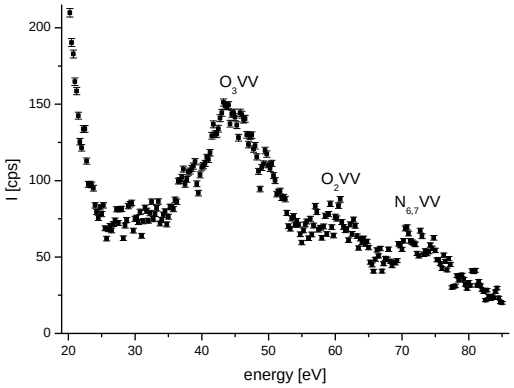

(f) Polycrystalline Au, FRR 1.0.

Figure 5.5: PAES spectra for 6 different polycrystalline elements. All spectra were taken with the WAM lens mode, except for the high energy part of Pd, because the WAM mode is not applicable at such high energies. The retarding ratios are given in the captions of the respective spectra. The measurement time amounted for all spectra to 80 min.

5.6.2 Correlation of Auger intensity and binding energy

As already stated the intensities in Figure 5.5 and thus the SNRs vary within a wide range. This is due to the different electron binding energy of the primary electron of the respective Auger transition. As already mentioned in Chapter 3, the core annihilation probability and hence the Auger electron intensity is proportional like $p_{core} \propto E_b^{-1.6}$, where E_b is the binding energy of the primarily annihilated electron.

In Figure 5.6 the Auger intensities are plotted in a double logarithmic scale as a function of the binding energy of the primarily annihilated electron. The intensities of Ni and Au are corrected due to their different retarding ratios (FRR = 1.0) in comparison to the other elements (FRR = 0.5). Without these corrections the intensities of Ni and Au would be underestimated due to the lower transmission with FRR = 1.0 compared to FRR = 0.5. The intensities of the Auger electrons are calculated using the spectra from Figure 5.5, assuming a linear background and taking only the area under the peaks into account. This is a rather conservative calculation, because e.g. the scattered Auger electrons are neglected, leading to error bars shown in Figure 5.6. Yet, for a qualitative statement this evaluation is sufficiently accurate.

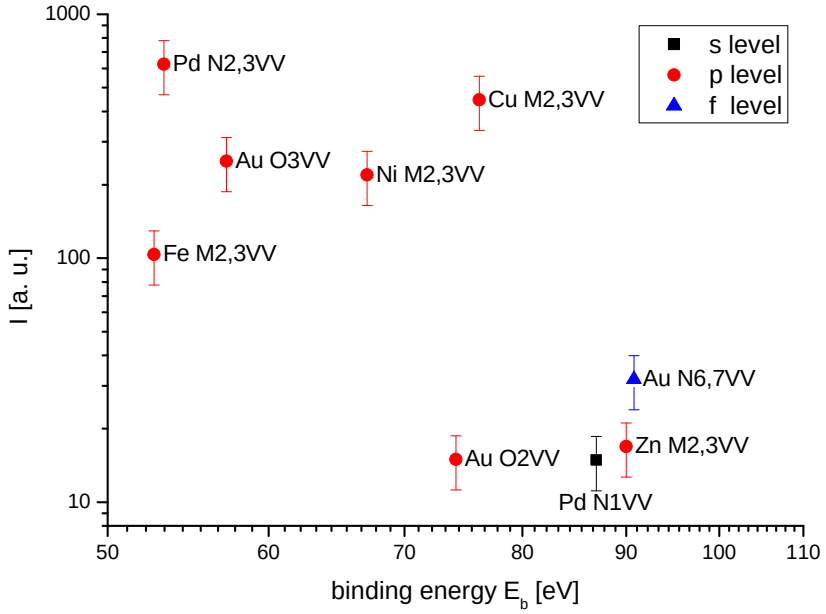

Figure 5.6: The Auger intensities obtained from the spectra shown in Figure 5.5 as a function of the binding energy of the primarily annihilated electron for Fe, Ni, Cu, Zn, Pd and Au [HMS09].

Regarding the following considerations the intensities plotted in Figure 5.6 can be interpreted as a direct measure of the core annihilation probability:
Since the binding energies of all considered electron levels is below 100 eV, virtual 100% of the deexitation of the electron shell takes place via the emission of Auger electrons. The relaxation via the emission of characteristic X-rays is negligible. Secondly, the

positron flux was constant during the measurement and thus the Auger intensity corresponds directly with the core annihilation probability.

The data in Figure 5.6 shows an obvious trend to higher Auger intensities for lower binding energies E_b. This is attributed to the repulsive Coulomb potential of the nucleus, which reduces the core annihilation probability p_{core}. Hence the trend of the semi-empirical formula

$$p_{core} \approx \frac{600 \cdot N(E_b)}{(E_b)^{1,6}} \quad , \tag{5.2}$$

which has already been introduced in Section 3.3, was confirmed by the measurement.

5.7 Sub-monolayers of Cu on Pd and Fe

5.7.1 Preconditions for the interpretation of the data

In order to study the surface sensitivity and elemental selectivity of PAES, a series of Cu-coated Pd and Fe samples were investigated. The processes that influence the measurement of systems with layered structures will be described shortly in the following. It is assumed that the positron energy is chosen low enough that the positrons diffuse back to the surface and predominantly do not annihilate in the bulk of the sample. This is certainly true for the chosen positron beam with an energy of 20 eV.

First, since layered structures are probed there will be a lattice mismatch between the different materials, and hence the presence of open volume defects is expected. Furthermore, the cleaning of the sample with Ar^+-ions will produce defects in the surface. Thus, positrons that pass such trapping sites will be captured with a high probability, see Chapter 2.3.

The second important fact that has to be taken into account is the varying positron affinity A_+ of the different elements. At open volume defects and at surfaces the positron annihilates predominantly with electrons from the element with the higher absolute positron affinity $|A_+|$. This easily leads to a misjudgment of the actual elemental composition and thus must be taken into account.

In order to study experimentally the influence of A_+, the layered systems are chosen such that all used elements have a sufficiently diverse positron affinity, see Table 5.1. Therefore, with PAES a varying increase of the Auger electron fraction of Cu is expected, since in the case of Pd, Pd should be overestimated with PAES. In the case of the Cu/Fe-system, Cu should be overestimated with PAES due to its higher positron affinity.
With EAES in contrast no significant difference between the two different systems is expected, since EAES averages over several layers. Both the surface sensitivity and the surface selectivity are reduced compared to PAES.

A_+(Pd)	A_+(Cu)	A_+(Fe)
$-6.40\,\text{eV}$	$-4.57\,\text{eV}$	$-3.20\,\text{eV}$

Table 5.1: Positron affinities of the investigated materials Fe, Pd, and Cu [FFW98, FFP83].

Measurements with Cu layers from $0.05 - 16.83\,\text{ML}$ on two different substrates, Pd and Fe, have been carried out. Pd samples coated with Cu will be denominated Cu/Pd and Fe samples with Cu are named Cu/Fe. All PAES measurements will be compared to conventional EAES.

5.7.2 Preparation of the layered samples

The procedure for the preparation of the layered samples was as follows: First, the clean, Ar^+-sputtered sample was measured. Then, the sample was again sputtered (see Section 5.2) and the cleanliness was verified with short time PAES-measurements. The temperature of the substrate during the evaporation was 300 K and the evaporation rate varied from 0.01 nm/s for thin films to 0.06 nm/s for the thicker Cu layers. The uncertainty in the layer thicknesses is governed by the time needed to move the shutter of the electron beam evaporator. This time amounted typically to 1 s, resulting in a thickness uncertainty between 0.01 nm and 0.06 nm.

The piezo thickness monitor displays the deposited amount of Cu in Ångstrom. The layer thicknesses, which are given in this thesis are given in ML[1]. Cu has a fcc structure with a lattice constant of $a = 3.61\,\text{Å}$ [Kit02]. The structure of the deposited Cu layers is unknown. There are three possible crystal directions for the definition of a ML: [100], [110] and [111]. In a fcc structure these three directions result in distances of $\frac{1}{\sqrt{4}}a$, $\frac{1}{\sqrt{3}}a$ and $\frac{1}{\sqrt{2}}a$, respectively. In this thesis the middle value, $\frac{1}{\sqrt{3}}a$ was chosen.

5.7.3 EAES and PAES measurements of Cu/Pd

In the first experiment, a polycrystalline, annealed and cleaned Pd foil served as substrate. Copper was evaporated from the electron beam effusion cell to coat the foil. Samples with 8 different layer thicknesses of $0.48 - 5.77\,\text{ML}$ were prepared. For EAES, an additional sample with 16.83 ML Cu was prepared. First, each sample was measured with EAES and then the same sample was measured with PAES. The measurement time with EAES amounted to 10 min and with PAES to 80 min per spectrum. The resulting electron spectra are plotted in Figure 5.7 (EAES) and Figure 5.8 (PAES). For better visibility the single spectra are plotted with offset.

Since with EAES the Pd $N_{2,3}$VV peak vanished completely in the secondary electron background, the monitored Auger transition was the Pd $M_{4,5}$VV-peak. The resulting

[1]Strictly spoken ML is an areal density with the dimension $[1/\,\text{mm}^2]$. One ML of Pt (111) corresponds to $1.504 \cdot 10^{13}\,\text{atoms/mm}^2$ [MK04].

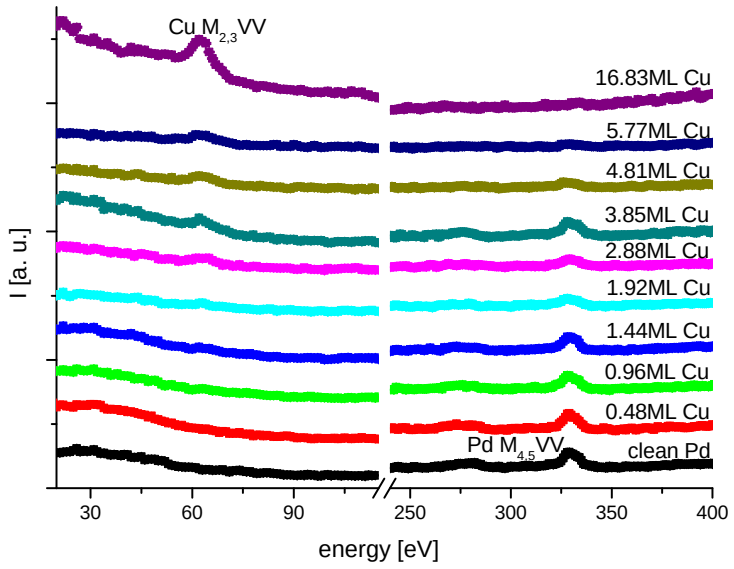

Figure 5.7: EAES spectra of clean Pd and of Pd with Cu layers of 9 different thicknesses (with different offset).

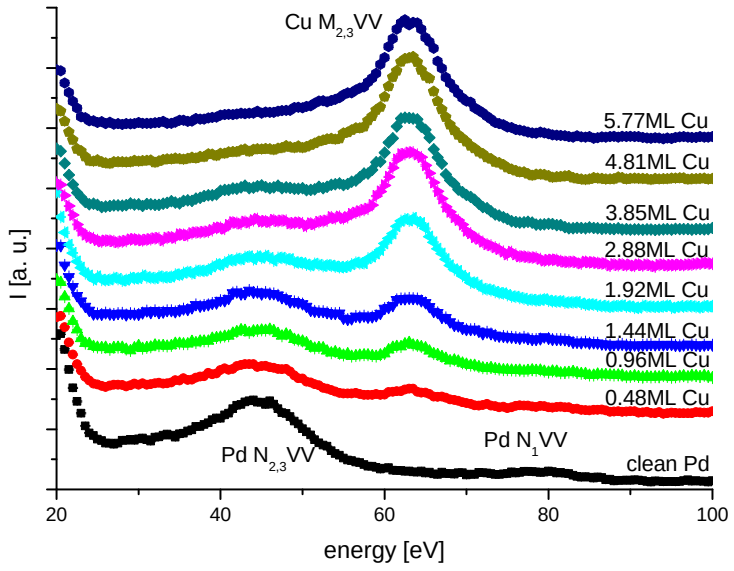

Figure 5.8: PAES spectra of clean Pd, and Pd with Cu layers of 8 different thicknesses (with different offset).

different IMFP due to the different kinetic energies of both Pd peaks influences the measurement not significantly. With EAES, there is no significant change visible in the spectra of Figure 5.7 until 1.92 ML of Cu cover the Pd substrate. With PAES, in contrast, it is seen clearly that the received substrate signal of Pd (Pd $N_{2,3}$VV) decreases considerably already with only 0.48 ML of Cu for the benefit of the Cu $M_{2,3}$VV-signal, see Figure 5.8.

Fitting procedure In order to evaluate the relative contributions of the Auger electrons from the different elements in a quantitative way, the following fitting routine was carried out for both PAES and EAES: first, spectra of the pure elements (Cu, Fe and Pd) were recorded, which serve as references. In the case of Cu, it was the Pd and Fe sample, respectively, coated with such an amount of Cu that no Pd and Fe peak, respectively, was visible any more. For PAES, this thickness was 5.77 ML Cu on Pd and 4.81 ML Cu on Fe, whereas with EAES 16.83 ML had to be deposited until the Pd peak vanished completely.

Then, the results for the coated spectra were fitted with linear combinations of the pure spectra, i.e. with only two free fitting parameters a and b:

$$I_{Cu/x}(E) = a \cdot I_{Cu}(E) + b \cdot I_x(E) \quad , \tag{5.3}$$

$$F_{Cu}(d) = \frac{a}{a+b} \quad \text{and} \quad F_x(d) = \frac{b}{a+b} \quad . \tag{5.4}$$

Here, $I_{Cu/x}(E)$ is the measured spectrum, which is to be fitted, while x stands for the two substrates Fe and Pd, respectively. The Cu layer thickness is named d. $I_{Cu}(E)$ and $I_x(E)$ are the reference spectra of the clean elements. $F_x(d)$ and $F_{Cu}(d)$ are the fractions of all detected Auger electrons, which stem from Pd, Fe and Cu, respectively. Since $F_{Cu}(d)$ and $F_x(d)$ are relative parameters any dependency on a possible change in the intensity of the primary beam is eliminated. In contrast to other data evaluations (e.g. [FFNW06]), where only the Auger peak energy range is used for the fit, here the whole spectrum for the linear combination for both EAES and PAES is used, since the shape of the spectrum is altered with varying layer thickness over the entire energy range. For instance, the reflectivity of the sample increases with increasing atomic number Z and thus leads to a different shape in the low energy region. The results of this fitting procedure, i.e. the Auger fractions for all different Cu thicknesses on Pd are plotted in Figure 5.9 and Figure 5.10.

The detailed analysis of the EAES data in Figure 5.9 shows that also with EAES at low Cu coverages a Cu signal is already visible. Exemplarily dotted lines mark the coverage with 0.96 ML of Cu in Figure 5.9, where less than 5% of all Auger electrons stem from Cu. Even with 5.78 ML Cu on Pd more than 60% of the Auger electrons stem still from the Pd substrate. As much as 16.83 ML of Cu had to be deposited to obtain the pure Cu signal.

In the case of PAES at the same coverage (0.96 ML of Cu), more than 30% of all Auger electrons originate from Cu, see Figure 5.10. For the pure Cu signal 5.78 ML of Cu

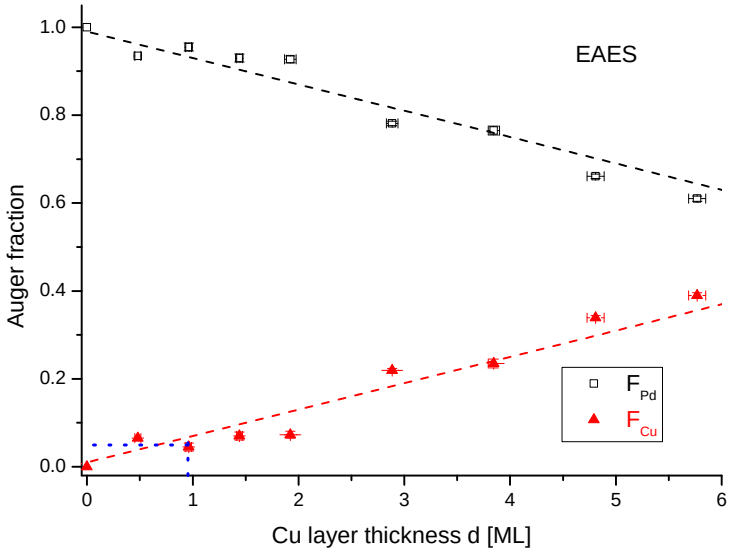

Figure 5.9: Fraction of the Auger signal from Pd and Cu, respectively, as a function of the Cu layer thickness, measured with EAES. The dashed lines here and in the following three graphs are eye guides and no fits.

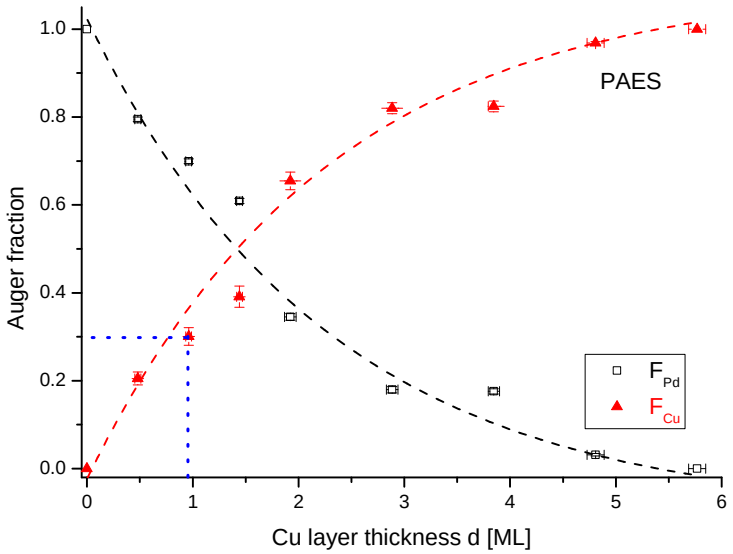

Figure 5.10: Fraction of the Auger signal from Pd and Cu, respectively, as a function of the Cu layer thickness, measured with PAES.

are sufficient. Bearing the positron affinities of both materials in mind ($|A_+(Pd)| > |A_+(Cu)|$) this means that with 5.78 ML Cu, the Pd surface must be covered completely with at least one Cu layer, since no positrons annihilate with Pd any more.
The measurement of the Cu/Pd system showed already the much higher surface selectivity of PAES compared to EAES.

5.7.4 EAES and PAES measurements of Cu/Fe

Next, Cu/Fe samples with even thinner layers, beginning at 0.05 ML of Cu up to 4.81 ML of Cu were prepared and measured with both EAES and PAES. For the Cu reference for EAES, also in this case the Pd sample with 16.83 ML was used.

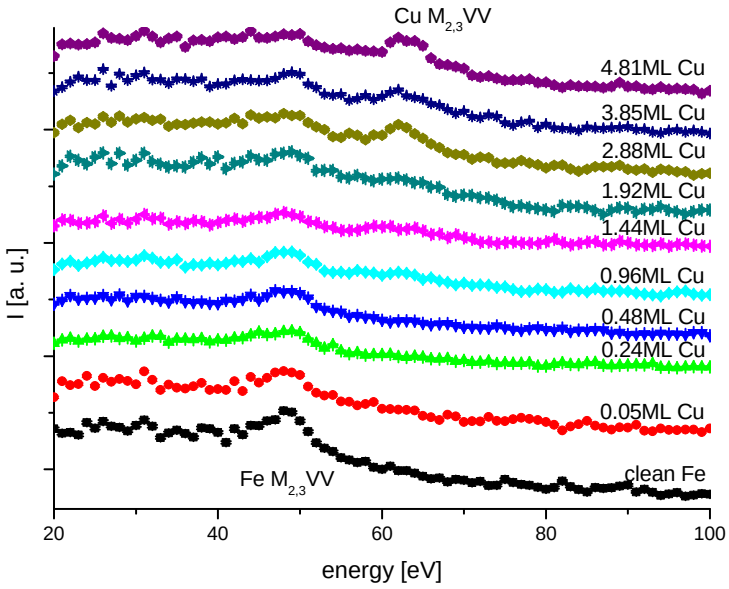

Figure 5.11: EAES spectra of clean Fe and of Fe with Cu layers of 10 different thicknesses (with different offset).

Figure 5.11 and Figure 5.12 show the single spectra for EAES and PAES, respectively. The results of the evaluation procedure for the relative Auger intensities obtained with EAES and PAES are plotted in Figure 5.13 and Figure 5.14, respectively. In both figures, dotted lines at 0.96 ML Cu coverage are plotted as in the case of Cu/Pd. In the case of EAES, less than 6% of the Auger electrons stem from Cu. At low coverages (0.05 ML of Cu and 0.24 ML of Cu) no Cu signal is detectable at all. Even with a Cu coverage of 4.81 ML more than 73% of the detected Auger electrons originate still from the Fe substrate.

With PAES, in contrast, more than 55% of all detected Auger electrons originate from Cu with 0.96 ML of Cu, cf. Figure 5.14. Even a low coverage of only 0.05 ML Cu leads

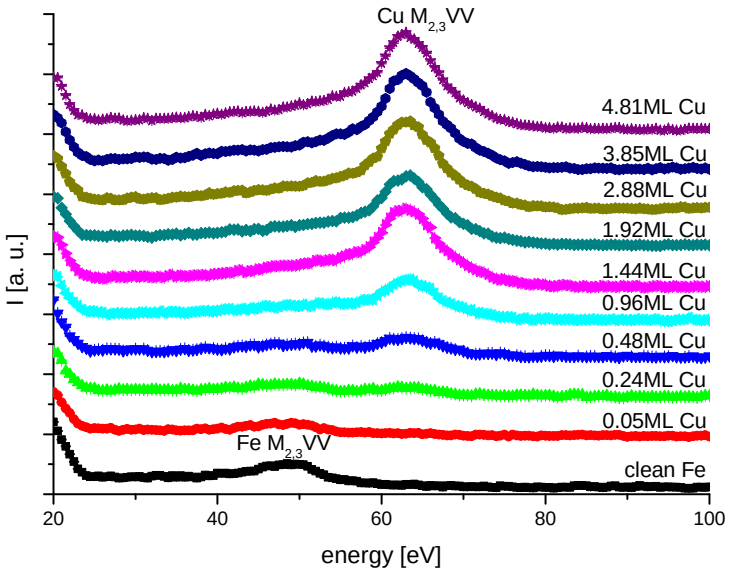

Figure 5.12: PAES spectra of clean Fe, and Fe with Cu layers of 10 different thicknesses (with different offset).

to a significant amount of Auger electrons from Cu of 5%. From 2.88 ML to 4.81 ML of Cu, the Cu signal varies only slightly from 95% to 100%.

5.7.5 Comparison of the Cu/Pd and the Cu/Fe systems

The comparison of EAES and PAES for both systems (Cu/Pd and Cu/Fe) shows that PAES is far more surface sensitive and elemental selective. The fraction of the Auger signal from the covering Cu layer increases much faster with PAES than with EAES. This is even true for the Cu/Pd-system, where the positron affinity actually favors the annihilation with Pd and not with Cu.

The analysis of the EAES spectra shows that there is no significant difference in the slope of the Auger intensities in the Cu/Pd and Cu/Fe systems. Also, the Cu intensity with 0.96 ML of Cu is comparable within the error, see Figures 5.9 and 5.13. With 4.81 ML of Cu in both cases roughly 70% of the detected Auger electrons stem still from the substrate and with both substrates 16.83 ML of Cu were necessary to obtain the pure Cu signal.

With PAES, a difference between the two substrates is clearly visible. The slope of the Cu intensity in Cu/Fe-system (Figure 5.14) is much steeper than in the Cu/Pd-system (Figure 5.10). In the case of Cu/Fe, 1.44 ML of Cu lead to a fraction of 75% Cu Auger electrons. But in the case of the Cu/Pd-system, 5.78 ML of Cu are needed for the pure Cu signal. This observation is explained by the higher absolute positron affinity of Cu compared to Fe and the higher positron absolute affinity of Pd compared to Cu. Due

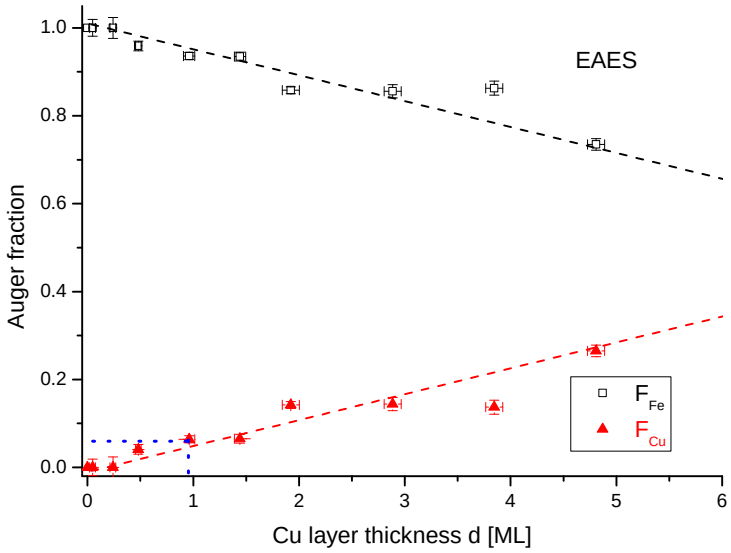

Figure 5.13: Fraction of the Auger signal from Fe and Cu, respectively, as a function of the Cu layer thickness, measured with EAES.

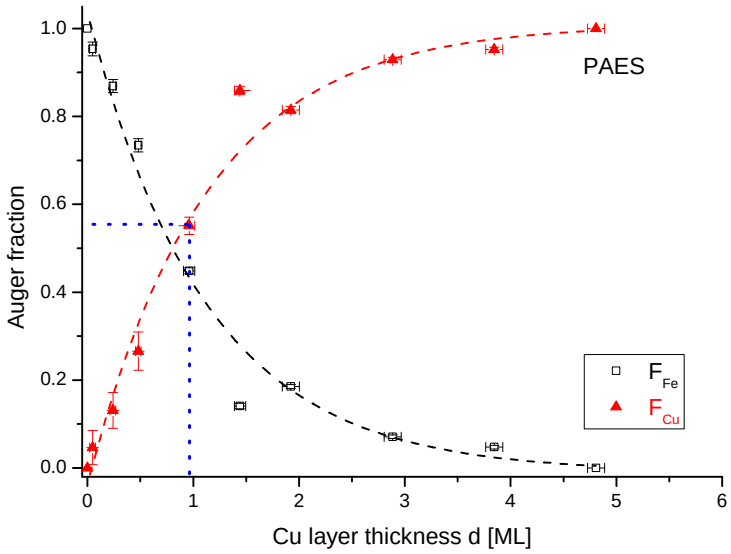

Figure 5.14: Fraction of the Auger signal from Fe and Cu, respectively, as a function of the Cu layer thickness, measured with PAES.

to the high surface sensitivity of PAES (e.g. [JW90]) it is also to be expected that with a coverage of one ML of Cu, almost all Auger electrons arise from Cu. This holds for the Cu/Fe system, but not for the Cu/Pd-system and is explained as follows.

The Cu layers do not grow homogeneously, but it is expected that they grow first, at low coverages, in a fingerlike structure. When the layers are already thicker, Cu islands are built [BGN+03]. The delocalized positron wave function, which is close to the surface, is then trapped in the deepest potential available. This is the surface potential. There, the positron annihilates with the element with the higher absolute positron affinity.

In the case of Cu/Fe the same argumentation holds with the only difference that now the positron rather annihilates with Cu due to its higher absolute positron affinity. For this reason, only 0.05 ML Cu on the Fe surface produce already more than 5% of all Auger electrons. Due to the higher positron affinity of Cu in the case of the Cu/Fe-system, 4.81 ML of Cu are enough to obtain the pure Cu signal, whereas with the Cu/Pd system 5.78 ML are necessary.

Thus, PAES has in both measured systems (Cu/Pd and Cu/Fe) the higher surface sensitivity compared to EAES. Due to the elemental selectivity of PAES, the surface sensitivity is even enhanced if appropriate materials are used with respect to their relative positron affinity.

5.8 Segregation of Cu in Pd

5.8.1 Time dependent measurement of Cu on Pd

Due to the short measurement time for a single PAES spectrum of only 420 s (see Section 5.4), it becomes for the first time possible to observe dynamic processes with PAES. Dynamic processes at the surface are e.g. catalysis processes, surface diffusion, the diffusion of coverage atoms into the bulk of a sample or the segregation of different elements.

Such a segregation is expected for thin Cu layers on Pd. Actually, it is anticipated that the Cu atoms migrate in the second atomic layer, where a stable configuration is assumed, following theoretical calculations [Løvvik05]. In order to test this calculated results experimentally, two PAES measurements as a function of time with 2.88 ML and 5.77 ML of Cu on Pd have been performed. Both samples were measured for 8.5 h and the measurement time for each data point in Figure 5.15 amounted to 15 min.

The fitting procedure for the determination of the Auger electron fraction is the same as explained in Section 5.7. The result of this evaluation is shown in Figure 5.15. There, the Auger fraction from Cu and Pd, respectively, is plotted as a function of time. This is done for both layer thicknesses.

In the case of 2.88 ML Cu on Pd, the Auger fraction from Cu stays constant for almost 2 h at 87% before it drops within 2 h to a constant value of 70%. The behaviour with 5.77 ML of Cu on Pd is likewise. There, at the beginning no Pd is observable at all.

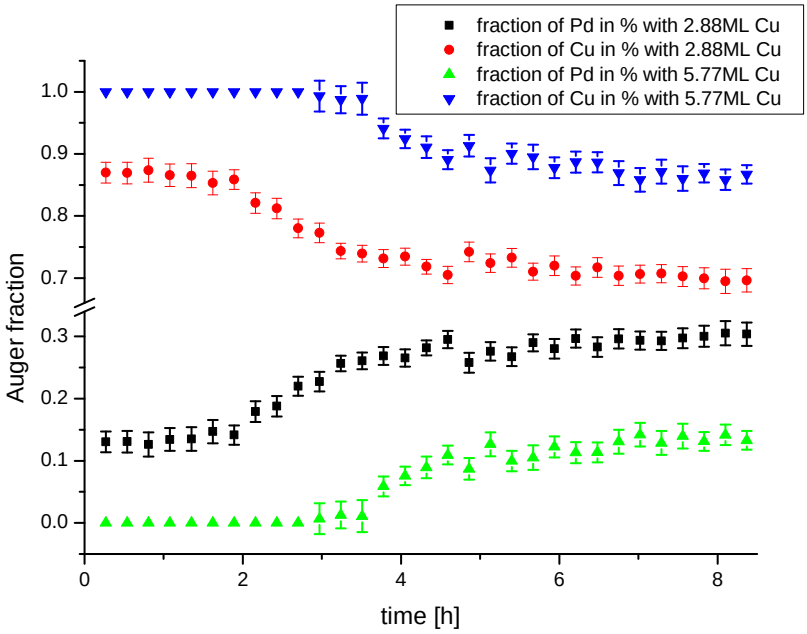

Figure 5.15: Fraction of the Auger signal from Pd and Cu, respectively, as a function of time for two different Cu layer thicknesses, measured with PAES.

Then, after little more than 3 h Auger electrons emitted from Pd become visible. After additional 2 h, the Cu signal stabilizes at 87% of all detected Auger electrons.

5.8.2 Interpretation

At the beginning, it should be noted that the coverage of Pd is expected to be not homogeneous, but Cu islands are anticipated [BGN+03]. If it were homogeneous with a little more than one ML of Cu, only Cu would be detectable with PAES. In the following, several possible explanations for the observed time dependency of the Cu and Pd intensities are discussed. First, the case of 2.88 ML Cu on Pd is treated.

The possibility that the Cu layer gets just contaminated by the residual gas molecules present in the analysis chamber, as it was observed in previous measurements [MHS08], is excluded. In this case, the Cu intensity would only drop, without the simultaneous increase of the Pd fraction. Furthermore, there would not be such a step like behaviour for both intensities.

The second explanation for the variation of the Auger intensities would be surface diffusion. Since the deposited Cu will not grow homogeneously, but in an island structure, it might be possible that the Cu atoms are rearranged in order to form a homogeneous layer. But this hypothesis is also dismissed, since the time scale for surface diffusion is of the order of seconds [MK04].

The third possibility is bulk diffusion of Cu in Pd, which would be observed after $\approx 2\,\mathrm{h}$. Typical bulk diffusion constants at room temperature for Cu diffusion would lead to

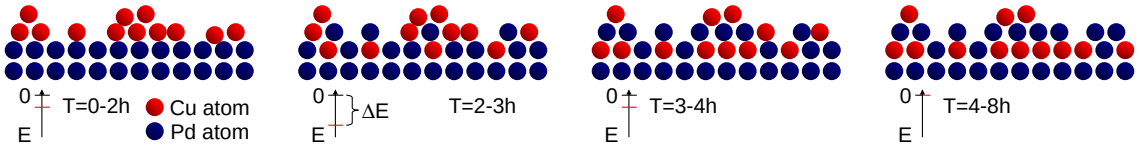

Figure 5.16: Qualitative description of the segregation and its driving energy ΔE.

visible changes within hours [Meh07]. The concentration of a covering element at the time t and the place x is given by $C(x, d)$ the solution of the thin film diffusion equation:

$$C(x,t) = \frac{M}{\sqrt{\pi D t}} \cdot e^{-\frac{x^2}{4Dt}} \quad . \tag{5.5}$$

D is the diffusion constant and $\sqrt{2Dt}$ is known as the characteristic diffusion length. M is the number of cover atoms per unit area, initially $(t = 0)$ placed at $x = 0$.
Thus, if the observed process was a pure bulk diffusion, an exponential decrease of the Cu fraction would be expected. Since a step like behaviour is observed, the possibility of bulk diffusion is also dismissed.

The most probable explanation is given in the following: The shape of the decrease of the Cu intensity seems not to be driven by a constant force, but by a time dependent force. This leads to the initial constant Cu Auger fraction, which decreases and then becomes constant again, resulting in the segregation of Cu in the second atomic layer. Such a behaviour is supported by theoretical calculations, where the segregation energy amounted to roughly $E \approx -6\,\mathrm{kJ/mol} \approx -63\,\mathrm{meV}$ [Løvvik05].
Qualitatively, the occurring processes are explained as follows, visualized also in Figure 5.16, where the potential energy E and the configuration of the atoms are shown schematically: Initially the energy that a single Cu atom gains (ΔE), when it reaches the second atomic layer is relatively small. Thus, only a few Cu atoms reach the second layer. When there are already some Cu atoms, ΔE increases leading to an enhanced migration of the Cu atoms into the second layer. If there are then more Cu atoms in the second layer, the free space available gets less, which causes ΔE to decrease. Hence the slope of the Cu Auger fraction curve gets flatter before the fraction remains at a constant value of 70%. The analogue explanation holds in the case of 5.77 ML of Cu. Also in this case, a part of the Cu diffuses into the Pd substrate. Since the Pd substrate was initially completely covered with Cu, also the final coverage after the migration of a part of Cu into the second layer is higher, leading to a final Cu fraction of 87%.

In order to control the gained results, the measurement with a **S**canning **T**unneling **M**icroscope (STM) would be ideal, to study the surface topology. Ideally, the sample is transferred to the STM without exposure of the sample to ambient pressure. Since at the PAES spectrometer no STM is available, it was tried to measure the sample at an external STM[2]. Unfortunately, the measurement was not successful, which is mainly attributed to the exposure to air.

[2]The STM at the chair E20 of the Physics department was used.

For that reason, it is planned to install a STM in an additional chamber, which will be attached to the existing PAES-spectrometer. With that, it will be possible to gain an entire picture of the sample surface. With PAES, the chemical composition of the sample surface is determined and with the STM the topology is revealed. Additionally further theoretical calculations are anticipated for a full explanation of the results.

5.9 Measurement of the positron work function

Finally, a completely different measurement was carried out, using the capability of the PHOIBOS 150 to analyze also positively charged particles. In this case the energy distribution of moderated positrons was analyzed, enabling to measure the positron work function of any material.

In order to show the feasibility of this idea, a ^{22}Na source with 950 kBq, was mounted directly below a 0.5 µm thick single crystalline W(001) foil. The positrons, emerging the source with up to 544 keV, are moderated in the tungsten foil and emitted with an energy corresponding to the work function of tungsten, $\Phi^+ = -3.0\,\mathrm{eV}$ [Col00]. In order to obtain the energy distribution of the positrons, the moderator is set to a positive potential of more than 10 V. This is done with the goal to shift the spectrum to higher energies, since the electron energy analyzer cannot detect particles with an energy less than 5 eV. A first spectrum of the moderated positrons is shown in Figure 5.17.
The sample was set on +18.4 V and the analyzer was operated in the FAT mode with a pass energy of 70 eV. With the slit width of 7 mm this leads to an energy resolution of $\Delta E \approx 1.75\,\mathrm{eV}$.

A clear peak at 16 eV can be seen. Since the electron energy analyzer is not calibrated for positrons, the measured energy of the positrons can be divided into three contributions in order to extract the kinetic energy of the positrons:

$$E_{measured} = E_{mod} + eV_{sample} + E_{corr} \quad . \tag{5.6}$$

E_{mod} is the energy of the moderated positrons, V_{sample} denotes the sample potential and E_{corr} is the correction energy of the analyzer for the detection of positrons.
Assuming a positron work function of $\Phi^+ = -3.0\,\mathrm{eV}$ for polycrystalline tungsten [Col00], the correction energy of the analyzer is calculated to

$$E_{corr} = E_0 - E_{mod} - eV_{sample} = 17.4\,\mathrm{eV} - 3.0\,\mathrm{eV} - 18.4\,\mathrm{eV} = -4.0\,\mathrm{eV} \quad . \tag{5.7}$$

In the upper scale in Figure 5.17, the energy is corrected by the sample potential and the calculated correction energy.

In order to calculate the moderation efficiency of the used W(001)-foil, the primary intensity and the intensity of the moderated positrons must be known. The primary positron intensity, emitted by ^{22}Na with a branching ratio of 90% amounts to

$$I = 950\,\mathrm{kBq} \cdot 0.9 = 855 \cdot 10^3\,\frac{\mathrm{e}^+}{\mathrm{s}} \quad . \tag{5.8}$$

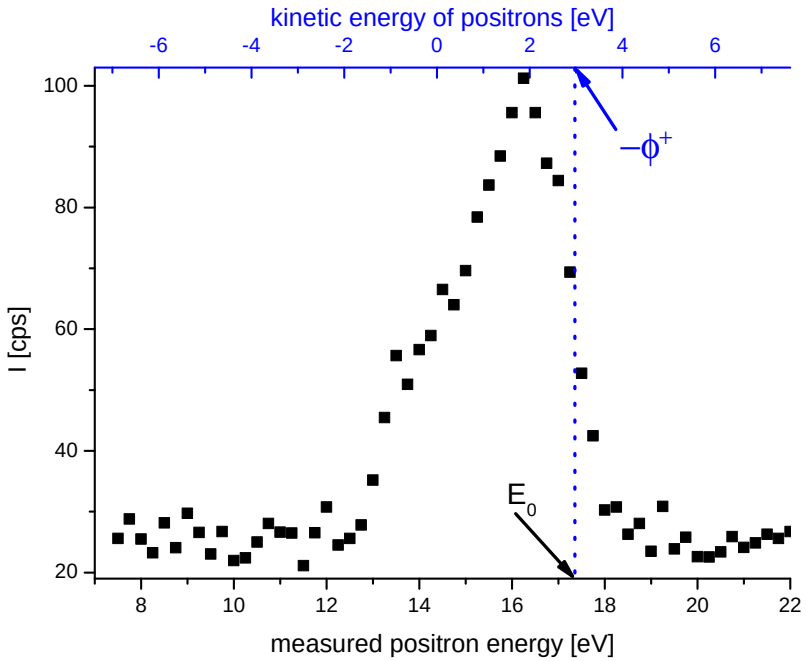

Figure 5.17: Measurement of energy distribution of positrons, which are moderated by tungsten. The positron intensity shows a clear peak at 16 eV due to the moderated positrons. The energy scale at the top is already corrected by the sample potential of 18.4 eV. In this scale, the maximal kinetic energy corresponds to $-\Phi^+$.

The integral over the obtained peak gives the overall intensity of moderated positrons. Additionally, the background of roughly 25 $\frac{e^+}{s}$ is subtracted. This results in

$$\int_{12\,\mathrm{eV}}^{18\,\mathrm{eV}} I(E)\,dE \approx 900\,\frac{e^+}{s} \quad . \tag{5.9}$$

Thus, the moderation efficiency of the measured W(001)-foil amounts to the realistic value of $\epsilon = \frac{900}{855 \cdot 10^3} \approx 1\,‰$.

This experiment demonstrated the capability of the spectrometer to study the relative moderation efficiency, the positron work function and the positron energy distribution in general. However, for future studies several things have to be improved: Firstly, a stable mounting of the moderator materials should be constructed, because with the simple setup as it was used now, the thin foils are not perfectly planar and hence the positrons are not emitted perpendicularly.
Secondly, it is desired to apply a coolable sample holder in order to measure at low temperatures, since the work function in general depends strongly on the temperature and frozen noble gases are highly efficient moderator materials.

Chapter 6

Conclusion and outlook

Within this thesis, the PAES setup at NEPOMUC has been improved in several ways. First, a new electron energy analyzer (PHOIBOS 150) has been installed and all components have been adapted correspondingly. This lead to a reduction of the measurement time for a typical PAES spectrum of one order of magnitude. Simultaneously, the quality of the measured spectra, i.e. the SNR, increased by up to one order of magnitude.

In addition, the measurement of a fast overview PAES spectrum became possible. The measurement time for such a spectrum amounts now to only 420 s for a 80 eV range compared to more than 3 h before this thesis. In this case, the SNR rose from 4:3 to 11:1. The short measurement time, which is now comparable to EAES, allows also to control the cleanliness of a sample prior to a more detailed measurement with PAES in a much more reliable way than with EAES. In addition, the reduced measurement time enabled for the first time the observation of dynamic processes with PAES. At two Pd samples with a few ML of Cu a time-dependent, step-like behaviour of the Cu-Auger-intensity was observed, which is interpreted as a segregation process of Cu in Pd.

Furthermore, the higher surface sensitivity and elemental selectivity of PAES compared to EAES was demonstrated. A Pd and a Fe substrate were prepared, each coated with increasing Cu layer thicknesses within a range from 5% of a ML up to 16.83 ML. The surface sensitivity of PAES was clearly demonstrated, as in the case of Fe 0.96 ML of Cu sufficed to obtain more than 55% of the Auger electrons from Cu, whereas with EAES the same layer thickness yielded less than 6%. Moreover, with PAES there was a clearly visible difference between the two substrates, emerging from the different positron affinities of the used elements. With EAES, in contrast the evaluation of the respective Auger electron fractions from Cu and the substrate revealed no differences between the Pd and the Fe substrate.

Finally, the ability of the PHOIBOS 150 to analyze also positively charged particles was used to measure the energy distribution of moderated positrons and hence the positron work function of tungsten. With minor modifications of the sample manipulator this will be possible for any kind of material.

For the future, further installations are foreseen. New electronics for the CCD readout are to be introduced in order to determine the positron intensity at the sample site quantitatively. With a temperature controlled sample manipulator more research areas will become accessible, since the dynamics of several surface processes are temperature driven. In the near future, a STM for the exploration of the sample topography and a X-ray source for XPS, providing a complementary elemental selective surface analysis method, will be installed. Thus, together with PAES the chemical and the structural composition of a surface can be explored. With the improvements achieved within this thesis, PAES gets for the first time accessible for external scientists in order to perform proposed surface sensitive measurements.

Chapter 7

Appendix

7.1 Calculated core annihilation probabilities

element	level				
	1s	2s	2p	3s	3p
$_{3}$Li	5.42				
$_{4}$Be	4.37				
$_{11}$Na	0.049	2.11	6.86		
$_{12}$Mg	0.032	1.56	4.87		
$_{13}$Al	0.021	1.18	3.53		
$_{14}$Si (100)			2.01 [FFW04]		
$_{19}$K		0.028	0.069	1.27	5.25
$_{22}$Ti		0.045	0.11	2.31	8.70
$_{23}$V		0.053	0.12	2.76	10.21
$_{24}$Cr		0.059	0.14	3.07	11.28
$_{26}$Fe		0.034	0.076	1.98	7.20
$_{28}$Ni		0.034	0.075	2.07	7.41
$_{29}$Cu		0.027	0.058	1.66	5.93
$_{30}$Zn		0.018	0.038	1.18	4.23

Table 7.1: Calculated core annihilation probabilities in %, from [JW90].

elemet	level				
	3s	3p	3d	4s	4p
$_{37}$Rb	0.021	0.072	0.17	1.05	5.31
$_{40}$Zr	0.039	0.13	0.26	2.05	8.71
$_{41}$Nb	0.042	0.14	0.26	2.18	9.07
$_{42}$Mo	0.040	0.13	0.24	2.12	8.74
$_{46}$Pd	0.026	0.080	0.13	1.51	6.07
$_{47}$Ag	0.022	0.069	0.11	1.38	5.53
$_{48}$Cd	0.015	0.047	0.073	1.01	4.06

Table 7.2: Calculated core annihilation probabilities in %, from [JW90].

element	level					
	4s	4p	4d	4f	5s	5d
$_{55}$Cs	0.020	0.078	0.26		0.93	4.41
$_{58}$Ce	0.052	0.19	0.18		1.48	5.60
$_{64}$Gd	0.039	0.14	0.39		2.03	9.01
$_{73}$Ta	0.034	0.12	0.30	1.82	1.94	8.43
$_{74}$W	0.036	0.13	0.31	1.64	2.05	8.80
$_{78}$Pt	0.026	0.089	0.21	0.75	1.56	6.63
$_{79}$Au	0.021	0.071	0.16	0.56	1.32	5.58
$_{81}$Tl	0.009	0.031	0.071	0.22	0.68	2.89
$_{82}$Pb	0.005	0.018	0.039	0.12	0.40	1.72

Table 7.3: Calculated core annihilation probabilities in %, from [JW90].

7.2 Positron affinities

Z	element	$\mathbf{A}_{+,\mathrm{exp}} = -(\mathbf{\Phi}^+ + \mathbf{\Phi}^-)$	$\mathbf{A}_{+,\mathrm{theo}} = -(\mathbf{\Phi}^+ + \mathbf{\Phi}^-)$
3	Li	-2.9	-7.80
	Li (100)		-6.37
	Li (110)		-6.44
	Li (111)		-6.46
4	Be (0001)		-2.62
			-4.60
6	C (100)	-0.67	
	(diamond)		
11	Na		-7.69
	Na (100)		-8.55
	Na (110)		-8.58
	Na (111)		-8.58
12	Mg		-7.04
			-6.63
13	Al (100)	-4.25	-4.09
	Al (110)		-4.09
	Al (111)	-4.31	-4.09
14	Si (100)		-6.95
	Si (110)		-6.95
19	K		-7.62
	K (100)		-7.08
	K (110)		-7.12
	K (111)		-7.13
21	Sc		-5.90
22	Ti		-3.60
23	V	-3.7	-4.26
24	Cr (100)	-2.7	-2.56
26	Fe	-3.2	-3.20
27	Co	-4.2	-4.40
28	Ni		-5.05
	Ni (100)		-4.45
	Ni (110)		-4.45
	Ni (111)		-4.45

Table 7.4: Positron affinities of elements from Li to Ni, calculated from the values of Φ^+ and Φ^- from [Col00].

Z	**element**	$\mathbf{A}_{+,\mathrm{exp}} = -(\mathbf{\Phi}^+ + \mathbf{\Phi}^-)$	$\mathbf{A}_{+,\mathrm{theo}} = -(\mathbf{\Phi}^+ + \mathbf{\Phi}^-)$
29	Cu		-4.57
	Cu (100)	-4.29	-4.36
	Cu (110)	-4.28	-4.34
	Cu (111)	-4.45	-4.49
30	Zn		-5.14
31	Ga		-5.96
32	Ge (111)		-6.78
37	Rb (100)		-7.13
	Rb (110)		-7.08
	Rb (111)		-7.16
39	Y		-5.90
40	Zr		-5.00
41	Nb		-4.90
42	Mo	-2.4	-3.00
	Mo (100)	-2.83	-1.88
	Mo (110)		-1.92
	Mo (111)	-1.55	-1.88
46	Pd		-6.40
47	Ag (100)	-5.22	-5.34
	Ag (110)		-5.36
	Ag (111)		-5.36
48	Cd		-6.40
49	In		-7.00
50	Sn (100)		-7.10
55	Cs (100)		-7.03
	Cs (110)		-7.08
	Cs (111)		-7.07
74	W	-2.5	
	W (111)	-1.87	
79	Au	-6.1	-6.30
82	Pb (100)	-4.01	-5.56
	Pb (100)	-4.01	-5.56

Table 7.5: Positron affinities of elements from Cu to Pb, calculated from the values of Φ^+ and Φ^- from [Col00].

Bibliography

[And33] Carl D. Anderson. The negative positive electron. *Phys. Rev.*, 43(6):491–494, Mar 1933.

[Aug25] Pierre Auger. Sur l'effet photoélectrique composé. *Journal de Physique et Le Radium*, 6:205–208, 1925.

[BG03] D. Briggs and J. T. Grant, editors. *Surface Analysis by Auger and X-ray Photoelectron Spectroscopy*. IMPublications and SurfaceSpectra Limited, 2003.

[BGN+03] Guillermo Bozzolo, Jorge E. Garcés, Ronald D. Noebe, Phillip Abel, and Hugo O. Mosca. Atomistic modeling of surface and bulk properties of Cu, Pd and the Cu-Pd system. *Progress in Surface Science*, 73(4-8):79 – 116, 2003.

[BJHK96] R. A. Bartynski, E. Jensen, S. L. Hulbert, and C. C. Kao. Auger photoelectron coincidence spectroscopy using synchrontron radiation. *Progress in Surface Science*, 53(2-4):155 – 162, 1996.

[BPN87] O. V. Boev, M. J. Puska, and R. M. Nieminen. Electron and positron energy levels in solids. *Phys. Rev. B*, 36(15):7786–7794, Nov 1987.

[BS83] D. Briggs and M. P. Seah, editors. *Practical Surface Analysis*. John Wiley & Sons, 1983.

[Cha76] D. Chattarji. *The theory of Auger transissions,*. Academic Press, 1976.

[CJ70] M.F. Chung and L.H. Jenkins. Auger electron energies of the outer shell electrons. *Surface Science*, 22(2):479 – 485, 1970.

[CK35] D. Coster and R. De L. Kronig. New type of auger effect and its influence on the x-ray spectrum. *Physica*, 2(1-12):13 – 24, 1935.

[Col00] P. Coleman, editor. *Positron Beams and their applications*. World Scientific Publishing Co. Pte. Ltd., 2000.

[Dir30] P. A. M. Dirac. A theory of electrons and protons. *Proceedings of the Royal Society A*, 126:360–365, 1930.

[FFNW06] N.G. Fazleev, J.L. Fry, M.P. Nadesalingam, and A.H. Weiss. Positron trapping at quantum-dot-like particles on metal surfaces. *Applied Surface Science*, 252(9):3327 – 3332, 2006.

[FFP83] G. Fletcher, J. L. Fry, and P. C. Pattnaik. Work functions and effective masses of positrons in metals. *Phys. Rev. B*, 27(7):3987–3991, Apr 1983.

[FFW98] N. G. Fazleev, J. L. Fry, and A. H. Weiss. Positron states and annihilation characteristics at the (100), (110), and (111) surfaces of alkali metals. *Phys. Rev. B*, 57(19):12506–12519, May 1998.

[FFW04] N. G. Fazleev, J. L. Fry, and A. H. Weiss. Surface states and annihilation characteristics of positrons trapped at the (100) and (111) surfaces of silicon. *Phys. Rev. B*, 70(16):165309, Oct 2004.

[Fir05] R.B. Firestone. Website, 2005. `http://www.nndc.bnl.gov/nudat2/decaysearchdirect.jsp?nuc=22NA&unc=nds`.

[FKWF77] J. C. Fuggle, E. Källne, L. M. Watson, and D. J. Fabian. Electronic structure of aluminum and aluminum-noble-metal alloys studied by soft-x-ray and x-ray photoelectron spectroscopies. *Phys. Rev. B*, 16(2):750–761, Jul 1977.

[GDPO+09] R. Gotter, F. Da Pieve, F. Offi, A. Ruocco, A. Verdini, H. Yao, R. Bartynski, and G. Stefani. $M_3M_{45}M_{45}$ Auger lineshape measured from the Cu(111) surface: Multiplet term selectivity in angle-resolved Auger-photoelectron coincidence spectroscopy. *Phys. Rev. B*, 79(7):075108, Feb 2009.

[HKR+02a] C. Hugenschmidt, G. Kögel, R. Repper, K. Schreckenbach, P. Sperr, B. Straßer, and W. Triftshäuser. Monoenergetic positron beam at the reactor based positron source at FRM-II. *Nuclear Instruments and Methods in Physics Research B*, 192:97–101, May 2002.

[HKR+02b] C. Hugenschmidt, G. Kögel, R. Repper, K. Schreckenbach, P. Sperr, and W. Triftshäuser. First platinum moderated positron beam based on neutron capture. *Nuclear Instruments and Methods in Physics Research B*, 198:220–229, 2002.

[HLM+08] C. Hugenschmidt, B. Löwe, J. Mayer, C. Piochacz, P. Pikart, R. Repper, M. Stadlbauer, and K. Schreckenbach. Unprecedented intensity of a low-energy positron beam. *Nuclear Instruments and Methods in Physics Research A*, 593:616– 618, 2008.

[HMS07] C. Hugenschmidt, J. Mayer, and K. Schreckenbach. Surface investigation of Si(100), Cu, Cu on Si(100), and Au on Cu with positron annihilation induced Auger-electron spectroscopy. *Surf. Sci.*, 601:2459–2466, 2007.

[HMS09] C. Hugenschmidt, J. Mayer, and K. Schreckenbach. High-resolution Auger-electron spectroscopy induced by positron annihilation on Fe, Ni, Cu, Pd, and Au. *Journal of Physics: Conference Series*, in press, 2009.

[HPSS08] C. Hugenschmidt, P. Pikart, M. Stadlbauer, and K. Schreckenbach. High elemental selectivity to Sn submonolayers embedded in Al using positron annihilation spectroscopy. *Physical Review B (Condensed Matter and Materials Physics)*, 77(9):092105, 2008.

[HSSS06] C. Hugenschmidt, K. Schreckenbach, M. Stadlbauer, and B. Straßer. First positron experiments at NEPOMUC. *Applied Surface Science*, 252:3098–3105, 2006.

[JW90] K. O. Jensen and A. Weiss. Theoretical study of the application of positron-induced Auger-electron spectroscopy. *Phys. Rev. B*, 41(7):3928–3936, Mar 1990.

[Kit02] Ch. Kittel. *Einführung in die Festkörperphysik*. Oldenburg, 2002.

[KLM+92] A. R. Koymen, K. H. Lee, D. Mehl, Alex Weiss, and K. O. Jensen. Positron states on the Cs/Cu(100) surface. *Phys. Rev. Lett.*, 68(15):2378–2381, Apr 1992.

[KLY+92] A.R. Koymen, K.H. Lee, G. Yang, H. Zhou, and Alex H. Weiss. Temperature dependent top layer composition of Pd on Cu(100). *Materials Science Forum*, 105-110:1411–1414, 1992.

[Kra79] M. O. Krause. Atomic radiative and radiationless yields for K and L shells. *Journal of Physical and Chemical Reference Data*, 8(2):307–327, 1979.

[KRBJ+08] R. Krause-Rehberg, G. Brauer, M. Jungmann, A. Krille, A. Rogov, and K. Noack. Progress of the intense positron beam project EPOS. *Applied Surface Science*, 255(1):22 – 24, 2008.

[KRL99] R. Krause-Rehberg and H. S. Leipner. *Positron annihilation in semiconductors*. Springer, 1999.

[KS90] B. Krusche and K. Schreckenbach. Intense positron sources by pair creation with neutron capture γ-rays. *Nuclear Instruments and Methods in Physics Research Section A: Accelerators, Spectrometers, Detectors and Associated Equipment*, 295(1-2):155 – 171, 1990.

[LDD+07] J. Laverock, S. B. Dugdale, J. A. Duffy, J. Wooldridge, G. Balakrishnan, M. R. Lees, G. q. Zheng, D. Chen, C. T. Lin, A. Andrejczuk, M. Itou, and Y. Sakurai. Elliptical hole pockets in the fermi surfaces of unhydrated and hydrated sodium cobalt oxides. *Physical Review B (Condensed Matter and Materials Physics)*, 76(5):052509, 2007.

[Leg06] S. Legl. Aufbau eines Time-of-Flight-Spektrometers zur Analyse Positronenannihilation-induzierter Auger-Elektronen. Diploma thesis, 2006.

[LH07] S. Legl and C. Hugenschmidt. A novel time-of-flight spectrometer for PAES. *Physica Status Solidi C*, 4/10:3981–3984, 2007.

[Li06] Hsin-I Li. Wikipedia: http://en.wikipedia.org/wiki/File:Slide1.PNG, Nov. 2006.

[LMK+89] Chun Lei, David Mehl, A. R. Koymen, Fred Gotwald, M. Jibaly, and Alex Weiss. Apparatus for positron annihilation-induced Auger electron spectroscopy. *Review of Scientific Instruments*, 60(12):3656–3660, 1989.

[Løvvik05] O.M. Løvvik. Surface segregation in palladium based alloys from density-functional calculations. *Surface Science*, 583:100 – 106, 2005.

[Mäh09] S. Mähl. SPECS GmbH. Personal communication, 2009.

[Mak61] A. F. Makhov. *Sov. Phys. Solid State 2*, 1934, 1961.

[May06] J. Mayer. Durch Positronenannihilation induzierte Auger-Elektronenspektroskopie an Kupfer und Silizium. Diploma thesis, 2006.

[Meh07] Helmut Mehrer. *Diffusion in solids*. Springer, 2007.

[Mei22] Lise Meitner. Über die β-Strahl-Spektra und ihren Zusammenhang mit der γ-Strahlung. *Zeitschrift für Physik A Hadrons and Nuclei*, 11:35–54, 1922.

[MHS08] J. Mayer, C. Hugenschmidt, and K. Schreckenbach. Study of the surface contamination of copper with the improved positron annihilation-induced Auger electron spectrometer at NEPOMUC. *Applied Surface Science*, 255(1):220 – 222, 2008.

[MK04] T. Michely and J. Krug. *Islands, Mounds, and Atoms: Patterns and Processes in Crystal Growth Far from Equilibrium* . Springer, 2004.

[MKJ+90] David Mehl, A. R. Köymen, Kjeld O. Jensen, Fred Gotwald, and Alex Weiss. Sensitivity of positron-annihilation-induced Auger-electron spectroscopy to the top surface layer. *Phys. Rev. B*, 41(1):799–802, Jan 1990.

[MSH07] J. Mayer, K. Schreckenbach, and C. Hugenschmidt. Positron annihilation induced Auger electron spectroscopy of Cu and Si. *Physica Status Solidi C*, 10:3928–3931, 2007.

[MSH09] J. Mayer, K. Schreckenbach, and C. Hugenschmidt. Recent development of the PAES set up at NEPOMUC. *Phys. Status Solidi C*, 11:2468—-2470, 2009.

[MTN08] Peter J. Mohr, Barry N. Taylor, and David B. Newell. Codata recommended values of the fundamental physical constants: 2006. *Reviews of Modern Physics*, 80(2):633, 2008.

[OP49] A. Ore and J. L. Powell. Three-photon annihilation of an electron-positron pair. *Phys. Rev.*, 75(11):1696–1699, Jun 1949.

[OSMY97] Toshiyuki Ohdaira, Ryoichi Suzuki, Tomohisa Mikado, and T. Yamazaki. Auger line shape analysis by time-of-flight positron-annihilation induced Auger-electron spectroscopy. *Materials Science Forum*, 255 - 257:769–771, 1997.

[Pio09] C. Piochacz. *Generation of a high-brightness pulsed positron beam for the Munich scanning positron microscope.* PhD thesis, TU München, 2009.

[PLN89] M J Puska, P Lanki, and R M Nieminen. Positron affinities for elemental metals. *Journal of Physics: Condensed Matter*, 1(35):6081–6094, 1989.

[PR99] A. Polity and F. Rudolf. Defects in electron-irradiated Ge studied by positron lifetime spectroscopy. *Phys. Rev. B*, 59(15):10025–10030, Apr 1999.

[PRWM72] P. W. Palmberg, G. E. Riach, R. E. Weber, and N. C. MacDonald. *Handbook of Auger Electron Spectroscopy.* Physical Electronics Ind., Inc., Edina, Minnesota, 1972.

[Pur38] Edward M. Purcell. The focusing of charged particles by a spherical condenser. *Phys. Rev.*, 54(10):818–826, Nov 1938.

[RB07] W. Eckstein R. Behrisch, editor. *Sputtering by Particle Bombardment Experiments and Computer Calculations from Threshold to MeV Energies.* Springer, 2007.

[RLG+93] K. A. Ritley, K. G. Lynn, V. J. Ghosh, D. O. Welch, and M. McKeown. Low-energy contributions to positron implantation. *Journal of Applied Physics*, 74(5):3479–3496, 1993.

[RT90] D Roy and D Tremblay. Design of electron spectrometers. *Reports on Progress in Physics*, 53(12):1621–1674, 1990.

[SAKH99] W. Stoeffl, P. Asoka-Kumar, and R. Howell. The positron microprobe at LLNL. *Applied Surface Science*, 149:1, 1999.

[Se67] H. Z. Sar-el. Cylindrical capacitor as an analyzer I nonrelativistic part. *Review of Scientific Instruments*, 38(9):1210–1216, 1967.

[Sev72] Kenneth D. Sevier. *Low energy electron spectrometry.* Wiley-Interscience, 1972.

[SL88] P.J. Schultz and K.G. Lynn. Interaction of positron beams with surfaces, thin films, and interfaces. *Rev. Mod. Phys.*, 60(3):701–779, Jul 1988.

[SOM+96] Ryoichi Suzuki, Toshiyuki Ohdaira, Tomohisa Mikado, Hideaki Ohgaki, Mitsukuni Chiwaki, and Tetsuo Yamazaki. Apparatus for positron-annihilation-induced Auger electron spectroscopy with a pulsed positron beam. *Applied Surface Science*, 100-101:297 – 300, 1996.

[SOM+97] R. Suzuki, T. Ohdaira, T. Mikado, H. Ohgaki, M. Chiwaki, and T. Yamazaki. Control and measurement system for positron experiments at the ETL linac facility. *Applied Surface Science*, 116:187 – 191, 1997.

[SPE] SPECS Gesellschaft für Oberflächenphysik und Computertechnologie mbH. *Manual for Phoibos Hemispherical energy analyzer series 2.08*.

[Str02] B. Straßer. *Aufbau einer Anlage zur positroneninduzierten Auger-Elektronenspektroskopie*. PhD thesis, TU München, 2002.

[The96] Albert J. P. Theuwissen. *Solid-State Imaging with Charge-Coupled Devices*. Kluwer Academic Publishers, 1996.

[vVSdR+01] A. van Veen, H. Schut, J. de Roode, F. Labohm, C.V. Falub, S.W.H. Eijt, and P.E. Mijnarends. Intense positron sources and their applications. *Materials Science Forum*, 363-365:415–419, 2001.

[Wes73] R. N. West. Positron studies of condensed matter. *Advances in Physics*, 22:263 – 383, 1973.

[WMJ+88] A. Weiss, R. Mayer, M. Jibaly, C. Lei, D. Mehl, and K. G. Lynn. Auger-electron emission resulting from the annihilation of core electrons with low-energy positrons. *Phys. Rev. Lett.*, 61(19):2245–2248, Nov 1988.

[YZJ+97] S. Yang, H. Q. Zhou, E. Jung, A. H. Weiss, and P. H. Citrin. High-resolution positron-annihilation-induced Auger electron spectrometer. *Review of Scientific Instruments*, 68(10):3893–3897, 1997.

[YZJW95] S. Yang, H.Q. Zhou, E.S. Jung, and Alex H. Weiss. Auger line shape of $M_{2,3}VV$ Measured with Positron Annihilation Induced Auger Electron Spectroscopy. *Materials Science Forum*, 175-178:249–254, 1995.

[ZB02] T. J. M. Zouros and E. P. Benis. The hemispherical deflector analyser revisited. I. motion in the ideal 1/r potential, generalized entry conditions, Kepler orbits and spectrometer basic equation. *Journal of Electron Spectroscopy and Related Phenomena*, 125:221–248, 2002.

Acknowledgments

At the end, I would like to thank all the people who encouraged me during my thesis. Without their help this work would not have been possible.
First of all, I would like to thank Dr. Christoph Hugenschmidt. He always came up with new ideas and believed in me and in my work even at moments, when I doubted the success. I am happy to work in his group, where he guarantees an enjoyable and productive atmosphere.
Secondly, I would like to thank Prof. Dr. Klaus Schreckenbach for his knowledge which helped in many aspects. Though he retired during my thesis, he was still interested in my work and came even more often to my office in order to discuss the results and to provide new thoughts.
I would also like to thank Prof. Dr. Peter Böni, who supported me in the last few years financially. Fruitful discussions with him gave input from a more external point of view.
I am also deeply grateful for the financial support of the FRM-II, who funded the new electron energy analyzer and to a great part also my position.
I would like to thank the whole NEPOMUC group (and friends) for the enjoyable and funny time we had together, not only during office hours. I was happy to work with Thomas Brunner, Kathrin Buchner, Sebastian Busch, Hubert Ceeh, Thomas Gigl, Karin Hain, Benjamin Löwe, Philip Pikart, Christian Piochacz, Markus Reiner, Reinhard and Florin Repper, Benedikt Stoib, Martin Stadlbauer, Christian Steyer and Alexander Wolf. I would not have come so happily and motivated to my office every day without all those helpful and friendly guys. Especially, I would like to thank Philip, Hubert and Benjamin for all their help with my minor and major computer concerns. Thank you Pio for proofreading my thesis. Thank you Kathrin for several cakes and „Lebkuchenherzen“ in the autumn of every year.
Special thanks also to Reinhard and Florin, who helped me with all my technical problems. Without Reinhard, I might still be thinking about how to position the new analyzer without damaging it. He just did it, thanks!
I would also like to thank the workshops from the FRM-II and the physics department. Representatively, thanks to Christian Herzog and Manfred Pfaller. They manufactured everything, even when I thought it was not possible and also when time was short, which unfortunately was often the case.
I would also like to thank Prof. Dr. Peter Feulner and Matthias Marschall from the chair E20. Peter helped me in several discussions with his knowledge in surface physics and Matthias measured my Pd sample with his STM.

I am deeply grateful to my parents for their financial and moral support during my studies and my thesis. This work would not have been possible without their help.
Finally, I am deeply grateful to Monika, who supported me during the last years. Thank you for your love and help!

List of publications

- J. Mayer and C. Hugenschmidt and K. Schreckenbach. High resolution positron annihilation induced Auger electron spectroscopy of the Cu $M_{2,3}VV$ -transition and of Cu sub-monolayers on Pd and Fe. *submitted*

- J. Mayer, K. Schreckenbach, and C. Hugenschmidt. Recent development of the PAES set up at NEPOMUC. *Phys. Status Solidi C*, 11:2468–2470, 2009.

- K. Schreckenbach, C. Hugenschmidt, B. Löwe, J. Mayer, P. Pikart, C. Piochacz, and M. Stadlbauer. Performance of the (n,γ)-based positron beam facility NEPOMUC. *Proceedings of the 13th International Symposium on Capture Gamma-Ray Spectroscopy and Related Topics*, 1090(1):549-553, 2009.

- C. Hugenschmidt, J. Mayer, and K. Schreckenbach. High-resolution Auger-electron spectroscopy induced by positron annihilation on Fe, Ni, Cu, Pd, and Au. *Journal of Physics: Conference Series*, in press, 2009.

- J. Mayer, C. Hugenschmidt, and K. Schreckenbach. Study of the surface contamination of copper with the improved positron annihilation-induced Auger electron spectrometer at NEPOMUC. *Applied Surface Science*, 255(1):220-222, 2008.

- Philip Pikart, Christoph Hugenschmidt, Jakob Mayer, Martin Stadlbauer, and Klaus Schreckenbach. Depth resolved Doppler broadening measurement of layered Al-Sn samples. *Applied Surface Science*, 255(1):245-247, 2008.

- Christian Piochacz, Gottfried Kögel, Werner Egger, Christoph Hugenschmidt, Jakob Mayer, Klaus Schreckenbach, Peter Sperr, Martin Stadlbauer, and Günther Dollinger. A positron remoderator for the high intensity positron source NEPOMUC. *Applied Surface Science*, 255(1):98-100, 2008.

- C. Hugenschmidt, T. Brunner, J. Mayer, C. Piochacz, K. Schreckenbach, and M. Stadlbauer. Determination of positron beam parameters by various diagnostic techniques. *Applied Surface Science*, 255(1):50-53, 2008.

- C. Hugenschmidt, G. Dollinger, W. Egger, G. Kögel, B. Löwe, J. Mayer, P. Pikart, C. Piochacz, R. Repper, K. Schreckenbach, P. Sperr, and M. Stadlbauer. Surface and bulk investigations at the high intensity positron beam facility NEPOMUC. *Applied Surface Science*, 255:29-32, 2008.

- J. Mayer, K. Schreckenbach, and C. Hugenschmidt. Positron annihilation induced Auger electron spectroscopy of Cu and Si. *Physica Status Solidi C*, 10:3928-3931, 2007.

- C. Hugenschmidt, B. Löwe, J. Mayer, C. Piochacz, P. Pikart, R. Repper, M. Stadlbauer, and K. Schreckenbach. Unprecedented intensity of a low-energy positron beam. *Nuclear Instruments and Methods in Physics Research A*, 593:616–618, 2008.

- C. Hugenschmidt, J. Mayer, and K. Schreckenbach. Surface investigation of Si(100), Cu, Cu on Si(100), and Au on Cu with positron annihilation induced Auger-electron spectroscopy. *Surf. Sci.*, 601:2459–2466, 2007.

- C. Hugenschmidt, T. Brunner, S. Legl, J. Mayer, C. Piochacz, M. Stadlbauer, and K. Schreckenbach. Positron experiments at the new positron beam facility NEPOMUC at FRM II. *Physica status solidi (c)*, 4:3947-3952, 2007.

- C. Hugenschmidt, J. Mayer, and M. Stadlbauer. Investigation of the near surface region of chemically treated and Al-coated PMMA by Doppler-broadening spectroscopy. *Radiation Physics and Chemistry*, 76(2):217-219, 2007.